

CHAPTER 1

1.0 INTRODUCTION

As the world's demand for energy continues to grow, unconventional gas will continue to grow in importance as a complement to conventional fossil fuel. Coal is the most abundant energy source in the world and plays host to a lot of natural gas resources. Between 3,500 and 9,500 trillion cubic feet (Tcf) of coalbed methane gas is contained in subsurface coal seams around the world, with anywhere from 1,000 to 3,000 Tcf in North America alone. Coalbed methane today accounts for about 9 percent of U.S. natural gas production. . Recent U.S. estimates (Rice, 1997) indicate more than 700 trillion cubic feet (Tcf) of coalbed methane gas in place, but less than 100 Tcf may be economically recoverable. The initial capital investments are huge; success is not guaranteed because the amount of gas that can be produced depends on the correct depth, the thickness, lateral continuity of the coal, permeability which is controlled by the amount of fracturing or cleats, and other barriers such as impermeable layers and faults or folds that keep the gas trapped within the coal seam.

Coalbed methane reservoirs differ from conventional gas reservoirs in the way the gas is stored. In coalbed methane reservoirs, gas is mostly stored as an adsorbed phase on the coal surface; whereas, in conventional gas reservoirs the gas is stored within the pore space. The behavior of the coalbed methane reservoir, therefore, is complex and understanding gas production and well design poses significant challenges.

1.1 Research Objective

There are two primary objectives in this study. The first is to use the amplitude variation with offset (AVO) technique to delineate areas of high fracture density within the Cameo coal interval at Rulison Field in Piceance Basin, Colorado. The second is to investigate the influence on the AVO response of the orientation of seismic lines relative to the orientation of fractures.

AVO has been used in the oil and gas industry as a Direct Hydrocarbon Indicator (DHI) and lithology indicator since 1980 (Rutherford et al, 1980). This concept has been extensively applied to gas-sand reservoirs and this is due to the Poisson's ratio contrast that exists between a gas-sand reservoir and the surrounding rocks. In contrast, AVO technology has not been widely applied to coalbed methane (CBM) exploration.

Factors that facilitate the use of AVO for CBM exploration include (Suping Peng et al, 2006:

- High reflection amplitudes: P- wave velocity, S-wave velocity and density of coal seams are usually lower than their surrounding rocks, thus creating a large impedance contrast between the coal and surrounding rocks.
- AVO anomalies: the AVO gradient anomaly for the top interface of a coalbed methane reservoir is usually positive because of the negative-reflection coefficient and the positive Poisson's ratio contrast at the interface.

- Stable geological properties of coal: coal is both the source rock and the reservoir rock of coalbed methane. A coal seam can cover tens of kilometers without much change in its inclination and strike.
- The presence of faults: the presence of faults in coal increases its permeability and storage capacity. It also increases the Poisson's ratio contrast between coal and its surrounding lithologies. The presence of fracture will decrease the shear modulus, thus decreasing the S-wave velocity more than the P-wave velocity.

Given these factors, I analyzed a prestack P-wave AVO dataset to delineate areas of high fracture density within the Cameo coal interval.

1.2 Study Area

In this section, I will review the geology of the study area, reservoir properties, and previous work. The study area is Rulison field, located in the Piceance Basin, Colorado.

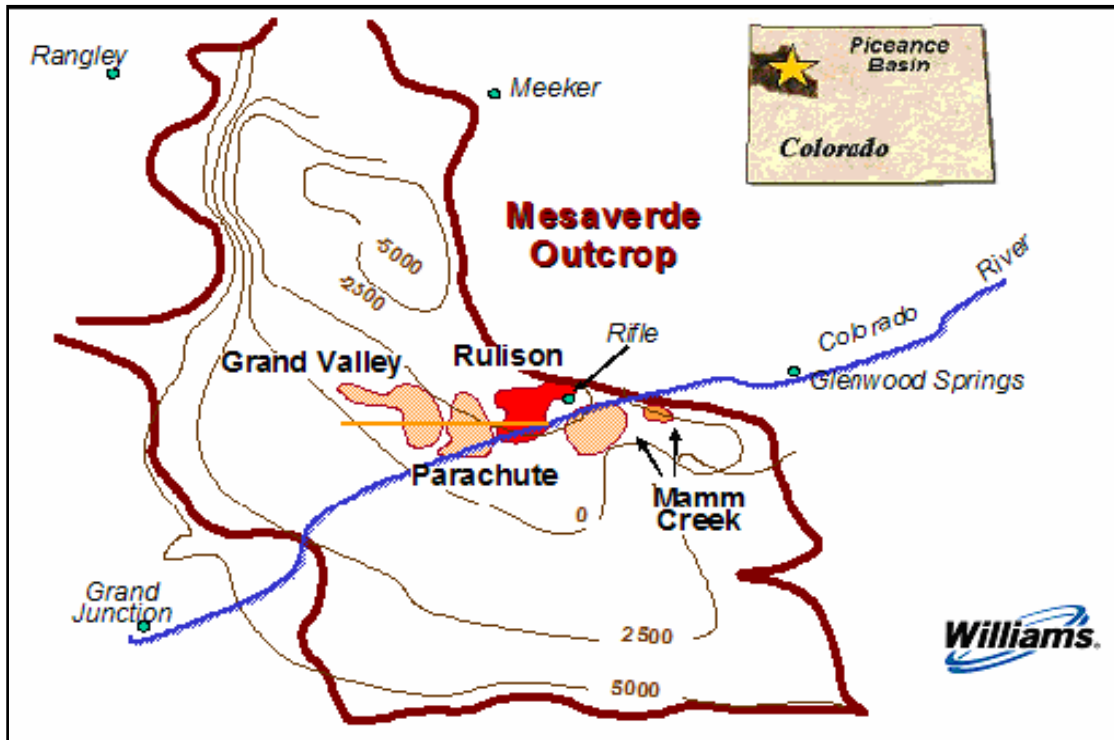


Figure 1.1: Map of Piceance Basin showing location of gas fields producing from the Williams Fork formation. (Courtesy Williams Oil Company)

Rulison Field is a basin-centered gas accumulation with no water leg. Gas production occurs in 1700 to 2400 feet of stacked discontinuous sandstones (Cumella and Ostby, 2003) within the non-marine Late Cretaceous Williams Fork Formation. (Figure 1.2)

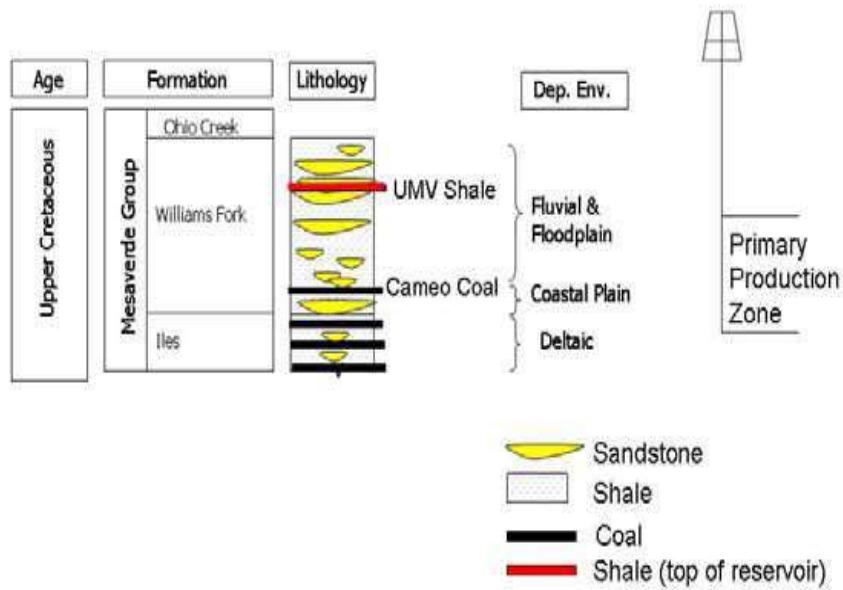


Figure 1.2: Simplified stratigraphic column of primary production interval for Rulison Field modified from Hinze (1998). The area of interest is the coal interval in the Williams Fork Formation.

The shallower productive sandstone layers average 20 to 60 feet in thickness and are interbedded in layers of siltstones, shales and coals (Jansen, 2005). The sandstones are discontinuous with limited lateral extent. The top seal for the sandstone reservoir is thought to be the UMV shale, but it could be some other type of capillary seal (Cumella, 2006). The bottom of the reservoir is bounded by Cameo coal. Typical reservoir porosity is between 3-12 percent and in-situ permeabilities are in order of 10-50 microdarcies (mD). Production relies on the presence of natural fractures. The coals and shales of the Williams Fork formation are the major sources of gas for this reservoir. Rulison Field is considered a fractured reservoir because its productivity and performance are strongly affected by the presence or absence of faults and fractures.

The coalbed methane reservoirs are found in the Upper Cretaceous Mesaverde Group which covers about 7,225 square miles and ranges in thickness from about 2,000 feet on the west to about 6,500 feet on the east side of the basin (Johnson, 1989). It is estimated that 80 trillion to 136 trillion cubic feet (Tcf) of gas are contained within the coalbed in the Piceance basin (Tyler et al., 1998). Total coalbed methane production was 1.2 billion cubic feet in 2000 (GTI, 2002). Two-thirds of the coalbed methane occurs in coals deeper than 5,000 feet, making the Piceance Basin one of the deepest coalbed methane areas in the United States (Quarterly Review, August 1993). The major coalbed methane target, below the Cameo coal zone is contained within the Williams Fork Formation of the Mesaverde Group and holds approximately 80 to 136 Tcf of coalbed methane (Tyler et al., 1998). This coal zone ranges in thickness from 300 to 600 feet and lies more than 6,000 feet below the ground surface (around 1200 ms two-way travel time) over a large portion of the basin (Tyler et al., 1998). Individual coal seams of up to 20 to 35-feet thick can be found within the group, with net coal thickness of the Williams Fork Formation averaging 80 to 150 feet thick. The Cameo Coal acts both as the reservoir as well as source rock. The coals contain natural fractures, but the cleat permeability at the depth of production in Rulison Field, is in the microDarcy range. Well productivity depends substantially on enhanced permeability through tectonic fractures. This is the reasons why my research is focus on the delineation of this fracture using prestack P-wave data.

1.3 Previous Work on Rulison Field

Extensive research has been conducted at Rulison Field by RCP; the major objectives of these studies are to better characterize the reservoirs in order to enhance the production. These research studies include; geological modeling, engineering modeling, rock physics, geomechanics, time-lapses, and multi-component analyses. I will summarize the relevant work below:

Gerardo Franco (2007) studied the P-wave seismic anisotropy at Rulison Field. He demonstrated anisotropy of tight-gas sandstones at Rulison varies (laterally and vertically) and generally correlates with lithology and fractures. He saw a correlation between high shear-wave splitting and lithology. There was also a correlation between high shear-wave splitting zones and gas concentration. He concluded that gas migration is enhanced by the natural fracture system at Rulison Field. Gerardo also concluded that P-wave NMO azimuthal anisotropy indicated a high eccentricity area on the western side of the Reservoir Characterization Project (RCP) study.

Matesic (2007) analyzed well logs to identify fractures and faults. He interpreted that the current in-situ stress orientation (S_{hmax}) is $N70^{\circ}W$. He also detected three sets of resistive (closed or partially open) fractures in the field with orientations of $N30^{\circ}W$, $N60^{\circ}E$, and $N70^{\circ}W$.

Higgins (2006) related stress, rock strength and pressure to create a one-dimensional geomechanical model. She stated that most of the natural fractures

and the drilling induced fractures are aligned in the same direction as the direction of present day maximum horizontal stress. From her interpretation of image logs and the dipole sonic log, Higgins has interpreted the average maximum horizontal stress direction is N72° W. Her work showed that stress magnitudes were lithology dependent.

Vasconcelos & Grechka (2006) characterize the multiple fracture sets in Rulison Field from the surface seismic dataset assuming an orthorhombic model. Their studies showed a set of cracks oriented WNW-ESE in the western part of the study and multiple fractures sets in its eastern part.

Xu (2006) analyzed azimuthal AVO and NMO ellipses using P-wave surface seismic data. Her azimuthal AVO analysis workflow included inverting the P-wave amplitudes for the azimuthally-varying AVO gradients and intercepts to obtain AVO ellipses. She found that the AVO-gradient anomalies at the bottom of the sandstone reservoir in Rulison coincided with intersections of wrench fault systems. She also concluded that the average fracture azimuth at the bottom of the sandstone reservoir (top of Cameo coal) should be close to N70W. The study showed a poor correlation between the azimuthal AVO and NMO ellipses.

Most of the research conducted so far at Rulison Field considered the William Forks Formation that is, the interval between the UMV shale and the Cameo. My work considers the interval between the top of Cameo and the Rollins. Previous researchers have determined the fracture orientation; they all agreed that the

dominant stress orientation is averagely N70°W. I will incorporate their findings into my work especially for modeling purposes.

1.4 Methodology

The major objective of this research delineates areas of higher fracture density within the Cameo coal interval in Rulison field, Piceance Basin Colorado. The data set will be carefully reprocessed and analyzed by me in order to delineate the areas of high fracture density from prestack P-wave data and the influence of AVO on the orientation of the seismic lines with respect to the fractures; this is the reason why the data will be analyzed both parallel and orthogonal to the fractures.

The approach for AVO analysis with prestack P-wave seismic data in Rulison involves four main steps. The first step consists of preparing the data in order to make it suitable for azimuthal AVO analysis. The goal of this step is to produce, as accurately as possible, an estimate of the reflection coefficients as a function of either offset or, equivalently, angle of incidence.

After reprocessing the data, the next step is modeling of synthetic CMP gathers; this is used to gain a qualitative insight into the sign and magnitude of the AVO gradient at the objective reflections.

The next stage is data analysis. This involves creating various AVO attributes; near-offset, mid-offset, far-offset stacks, AVO intercept, AVO gradient and AVO curvature. It also involves detail analysis of the prestack P-wave data.

The last stage is data reconciliation that encompasses matching the synthetic models with the actual data.

Figure 1.3 is a diagram representation of the AVO workflow described above.

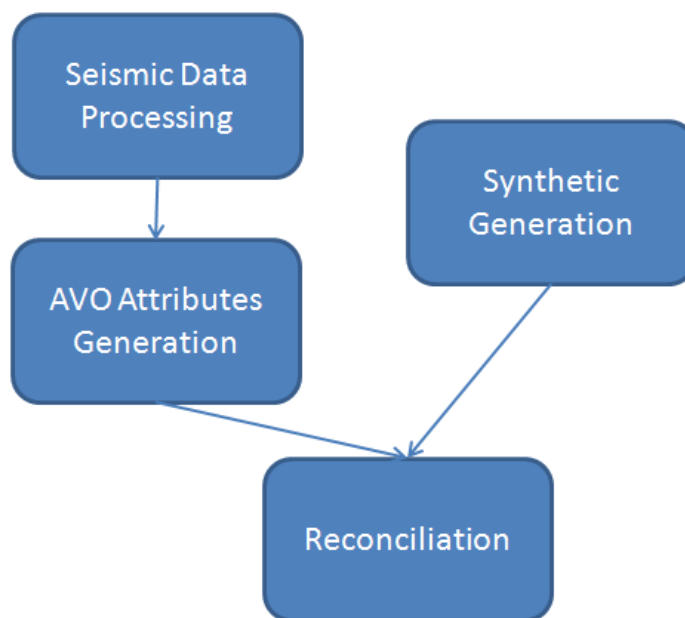


Figure1.3 Research Workflow

CHAPTER 2

DATA ACQUISITION AND PROCESSING

2.0 Introduction

In this section, I will describe the acquisition parameters and also the processing parameters applied to the 3-D multi-azimuth prestack P-wave data.

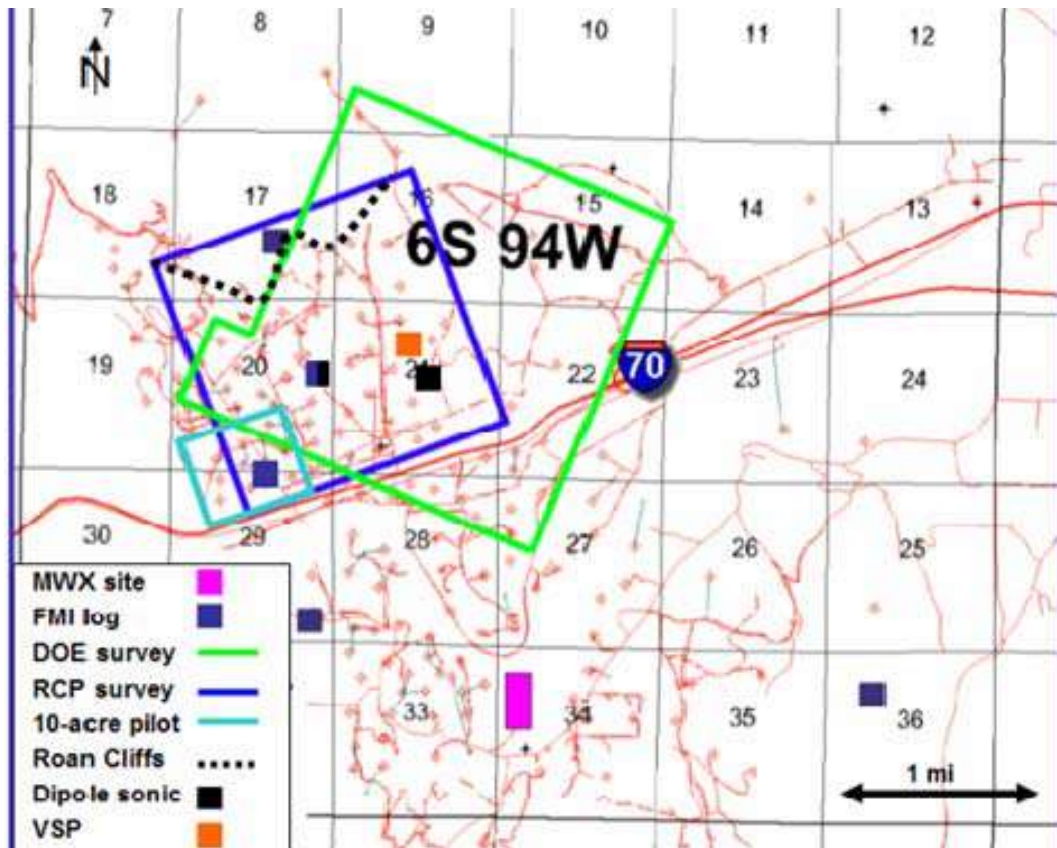


Figure 2.1 Rulison Field Survey Area

The Colorado School of Mines, Reservoir Characterization Project, acquired a 4-D multi-component seismic data in 2003 and the data were processed by Veritas DGC. The survey area is bounded to the south by Interstate 70 and to the north by the topographic feature of the Roan Cliffs. The survey highlighted in green in Figure 2.1 shows the extent of the 1996 U.S. Department of Energy 3D P-wave seismic survey while the survey highlighted in blue defines the extent of the time-lapse RCP surveys. There is a 3D vertical seismic profile (VSP) in the southeast corner of the survey area; it was collected in the RMV 30-21 well during the 2003 survey. Log information was also acquired in the RCP survey area along with the seismic information.

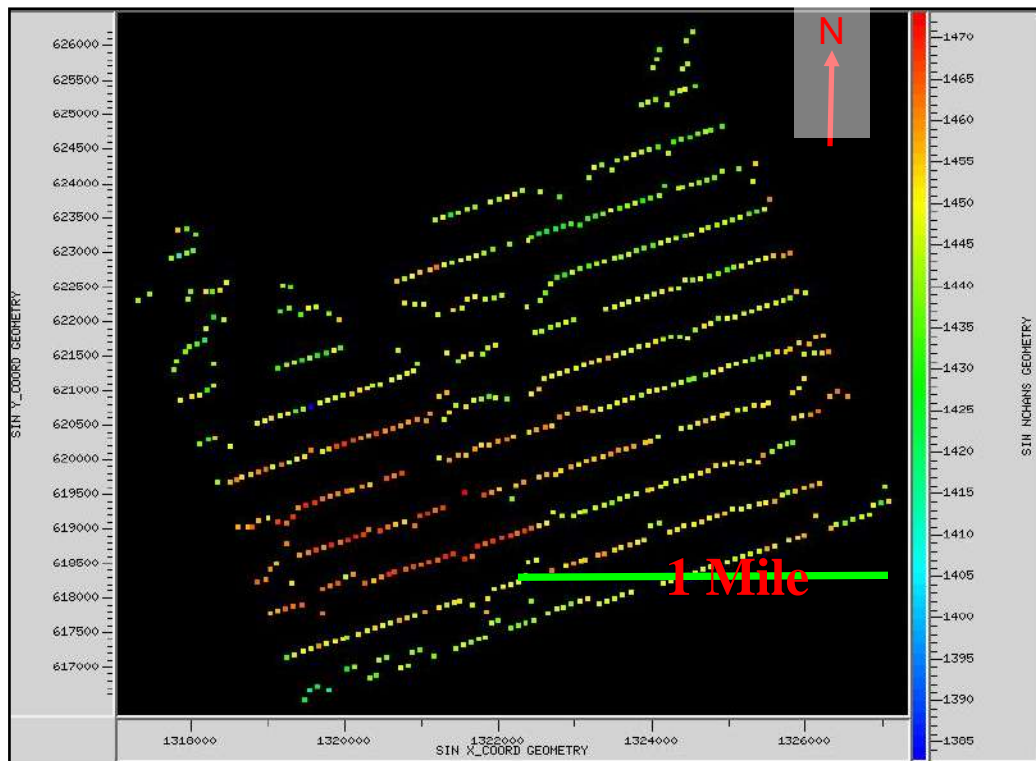


Figure 2.2 Sources locations in Rulison, the vertical axis is the y-coordinate while the horizontal axis is the x-coordinate.

The log information includes: Full-bore Formation Microimager (FMI) and cross-dipole sonic logs. The RCP surveys covered an area of 7260 ft by 8250 ft or 2.15 mi² (5.57 km²). The survey included approximately 1500 receivers and 700 source locations. The receivers consisted of 26 approximately north-south inlines, each containing 66 receiver groups spaced 110 ft apart. The inlines were spaced 330 ft apart in an approximate east-west direction (Figure 2.2). All receivers were active for each source point, with the signals being recorded using radio telemetry. 12 source lines were run perpendicular to the receiver lines in the approximately east-west direction.

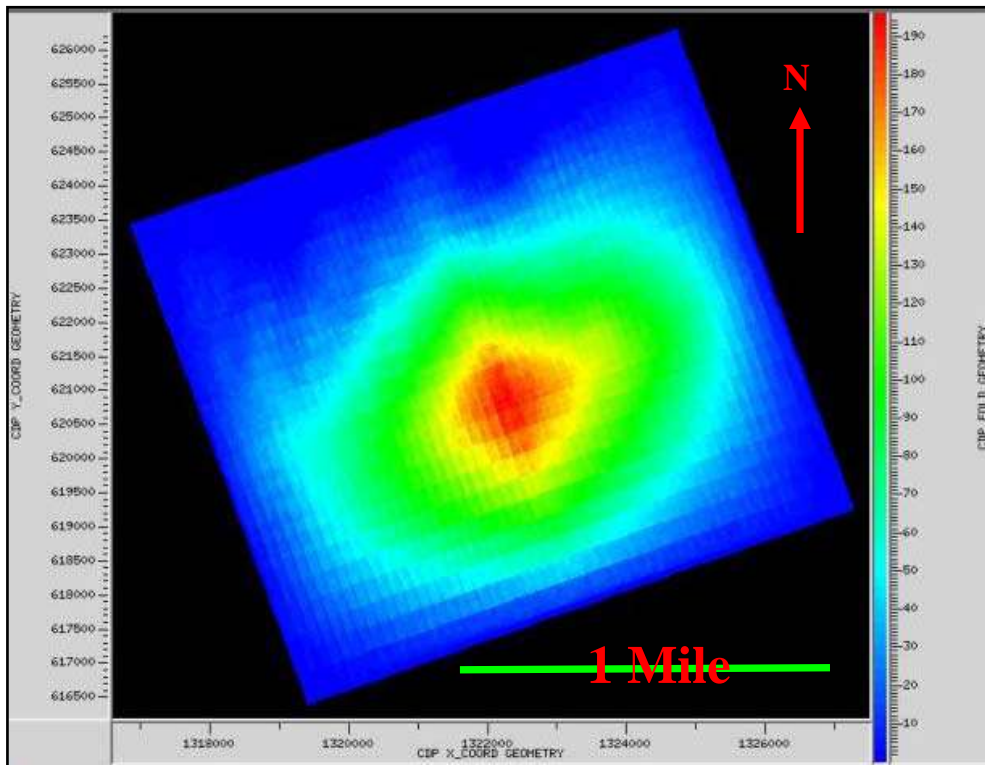


Figure 2.3 Fold Map. The color represents the fold, with the hotter colors representing the larger values of the fold. See the color bar on the right-hand side.

Each inline contained 75 source locations spaced every 110 ft. Source lines were spaced at 660 ft intervals in an approximate north-south direction (Figure 2.2). Due to the limited size of the survey, a maximum fold of 225 was achieved in the central part of the survey area (50'x 50' bin size) and it decreased toward the edges of the survey area. (Figure 2.3). There is also an area of low fold data in the northern edge of the survey. This area coincides with the rise in topography associated with the Roan Cliffs that prevented full source and receiver coverage (Figure 2.2 and figure 2.4). Solid State Geophysical acquired the seismic dataset using a Mertz 18 vibrator as the P-wave source and an IVI Tri-Ax as the S-wave sources. Individual P-wave shots consisted of six 5-120 Hz sweeps over 10 seconds. The vibrators were controlled by Pelton VibPro 3X electronics I/O VectorSeis System. Four single sensor digital multi-component receivers were surveyed into location using ground based techniques and Global Positioning System (GPS). Receivers were the Vectorseis Mertz sensors. Each receiver was inserted into a hole drilled into the ground and it was oriented with a compass. Figure 2.4 shows the receiver lines

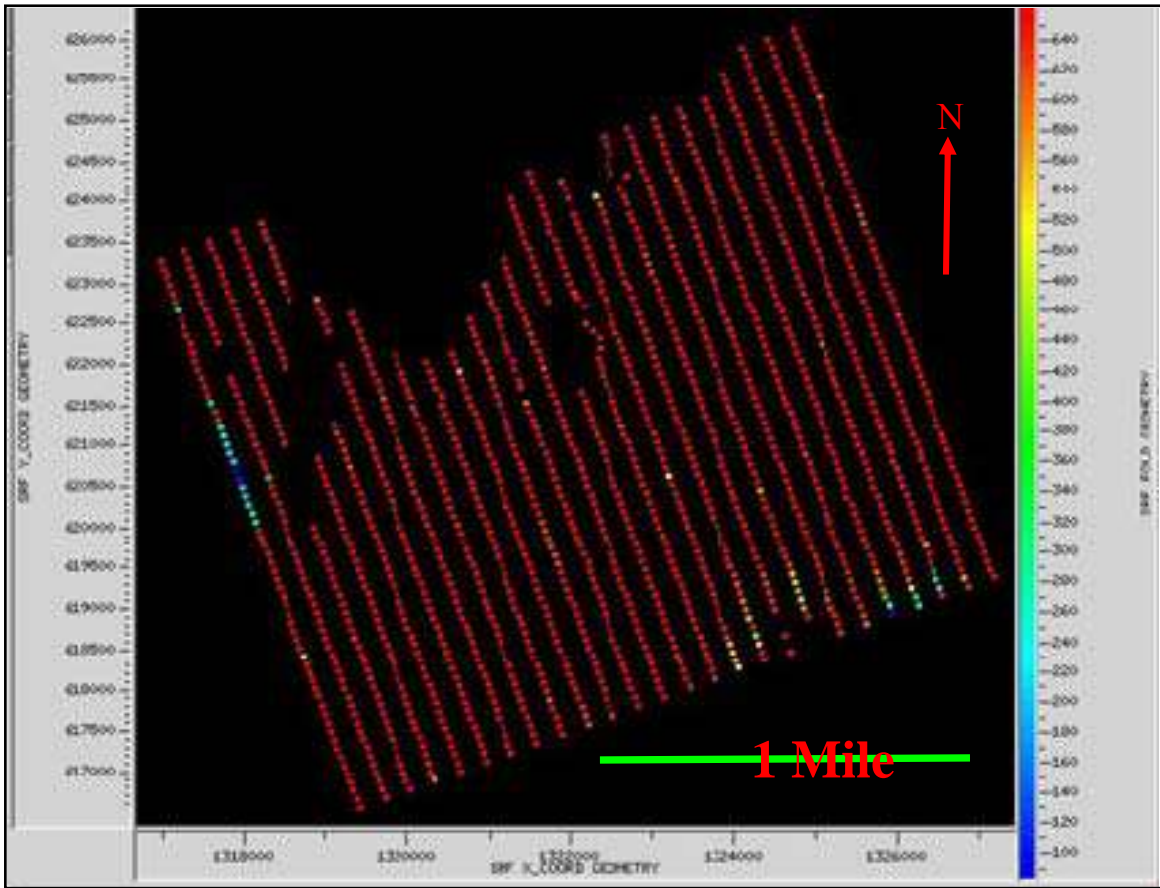


Figure 2.4: Receivers locations in Rulison. The vertical axis is the y-coordinate while the horizontal axis is the x-coordinate

The specifications for these receivers are shown in Table 2.1

Table 2.1 Receiver Specification

Sampling Rate	2- ms
Instantaneous Dynamic Range	118 dB
Bits	24 bits
Time Break Accuracy	+/- 8 μ s
Inclination Resolution	+/- 0.5 $^{\circ}$

2.1 Processing

In this section, I describe the processing sequence applied to the 3D seismic survey. Processing steps applied to the data by Veritas DGS are:

- Tilt Correction was applied in the field
- Demultiplexing
- A Spreading Gain Recovery- A time-square function was applied $1/t^2$
- Surface Consistency scaling- Shot and station compensation was applied
- Deconvolution
- Weathering Static: Tomostatics was used with a processing datum of 5850 ft along with a replacement velocity of 12874 ft/s
- Velocity Analysis
- NMO correction
- Statics

This flow was implemented by Veritas strictly for data preconditioning. Figure 2.5 shows the Veritas processed data after the application of this above processing sequence.

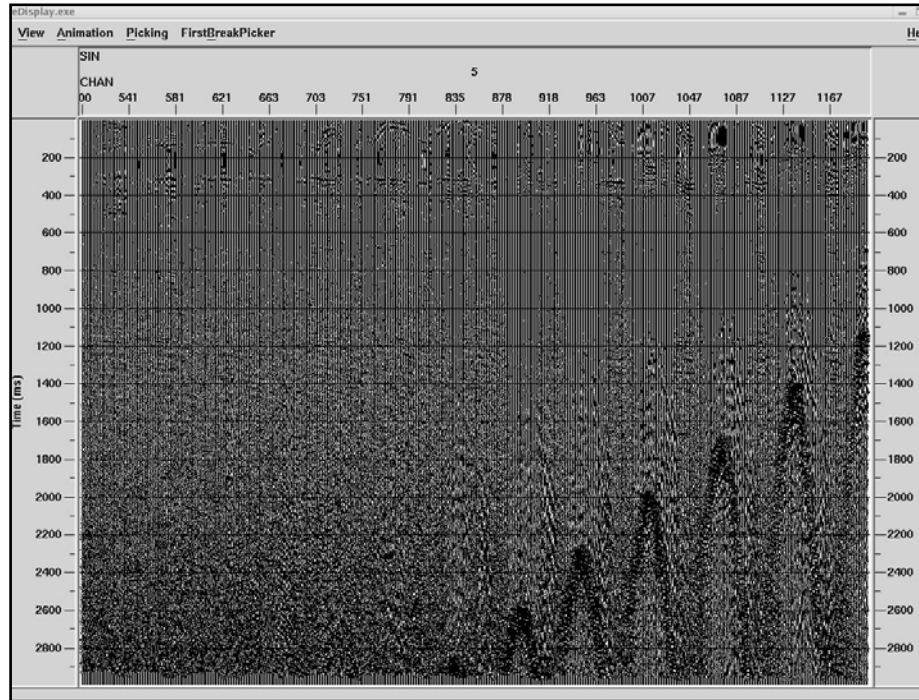


Figure 2.5 Veritas processed data (shot profiles) after the application of this above-listed processing sequence.

Below is the processing workflow that I applied to this data set:

- Extract database file & run the 3D Land Geometry: The Geometry is already installed in the trace headers, so for reprocessing, the Extract Database algorithm in Promax reads this information from the input trace headers and builds a database from trace headers.
- Database header transfer-Load to trace header from database
- Inline geometry header load
- Sort the data by source index number and recording channel number
- Air blast attenuation: this will be described below
- Data sorting by azimuth: this step also be will be described later
- Data sorting by CDP bin number and absolute value of offset

- CDP Diversity Stack: the data were stacked with different offset ranges in order to create the near-offset stack, mid-offset stack and the far-offset stack volumes. The details will be explained later.
- Trace equalization : The processing step will be described later
- F-K migration
- Seisworks volume: I created six volumes, three for each of the two azimuth separated data. I output all of them as Seisworks volumes because that is the only format that the Landmarks' AVO modeling software recognizes.

2.2 Air Blast Attenuation

The high-energy event in Figure 2.5 is air blast. This air blast must be suppressed without causing any damage to the relative amplitudes of the data. In order to suppress the airwaves I used the air blast attenuation algorithm in ProMax, Landmark's seismic processing software. The data were sorted by source and channel number. Then, Air Blast Attenuation was applied in order to remove the unwanted noise. The Air Blast Attenuation algorithm tries to address the problems of strong energy from sources, such as shot-generated air blasts which contaminate seismic data with very high amplitude, broad-band noise. It will automatically seek out anomalous energy on a trace-by-trace basis, given a pilot velocity, a relative noise amplitude threshold, and an approximate energy envelope width. This strong energy, if found, can be either surgically muted with appropriate edge tapering, or attenuated down to an amplitude level similar to the surrounding data. If the trace does not appear to be contaminated by noise, the

process will leave the trace untouched. I chose the attenuation option in order not to eliminate any data. Since Air Blast Attenuation is a single trace process, the trace-to-trace amplitude variations are approximately preserved. This is important for subsequent processing attempts to measure and preserve true amplitude relationships. Figure 2.5 shows the data before the application of the Air Blast Attenuation algorithm; Figure 2.6 shows the data after the application of the airwave attenuation; most of the air waves were attenuated along with part of the underlying amplitudes.

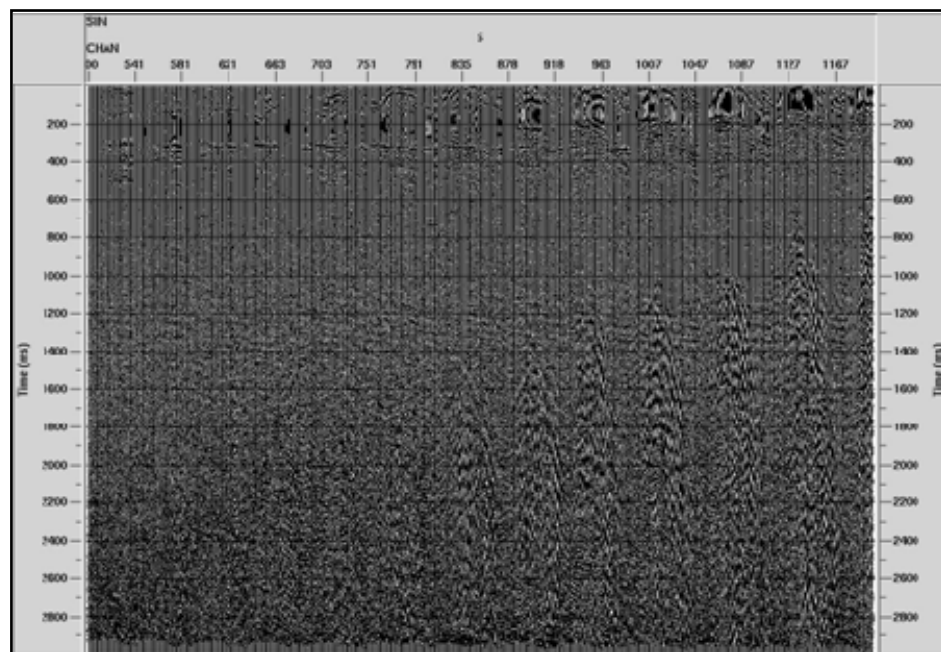


Figure 2.6: prestack P-wave data after the application of Landmark's air blast attenuation algorithm

In order to be able to see the noise removed. The data in Figure 2.6 were subtracted from the data in Figure 2.5. Figure 2.7 is the difference between the

original data and the attenuated data; this shows the air waves which were attenuated.

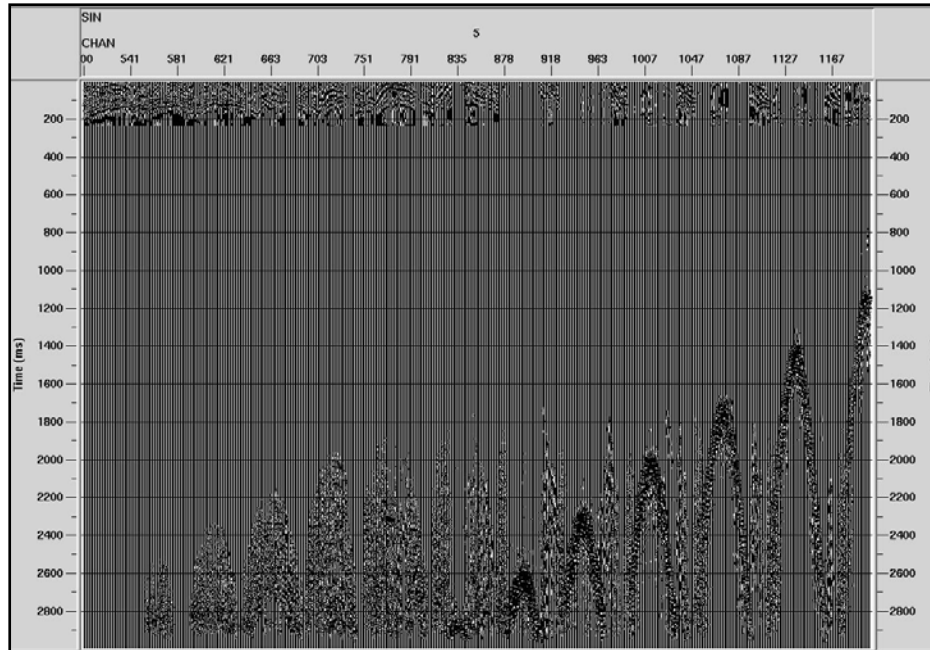


Figure 2.7: Attenuated air blast energy

2.3 Data Sorting by Azimuth

After the air blast was suppressed, the data were sorted by azimuth. The sorting was based on the dominant fracture orientation in the study area. Higgins (2006) determined that most of the natural fractures and drilling fractures in the study area are aligned in the same direction as the present day maximum horizontal stress. From her interpretation of image logs and the dipole sonic log, the average maximum horizontal stress direction is N72° W

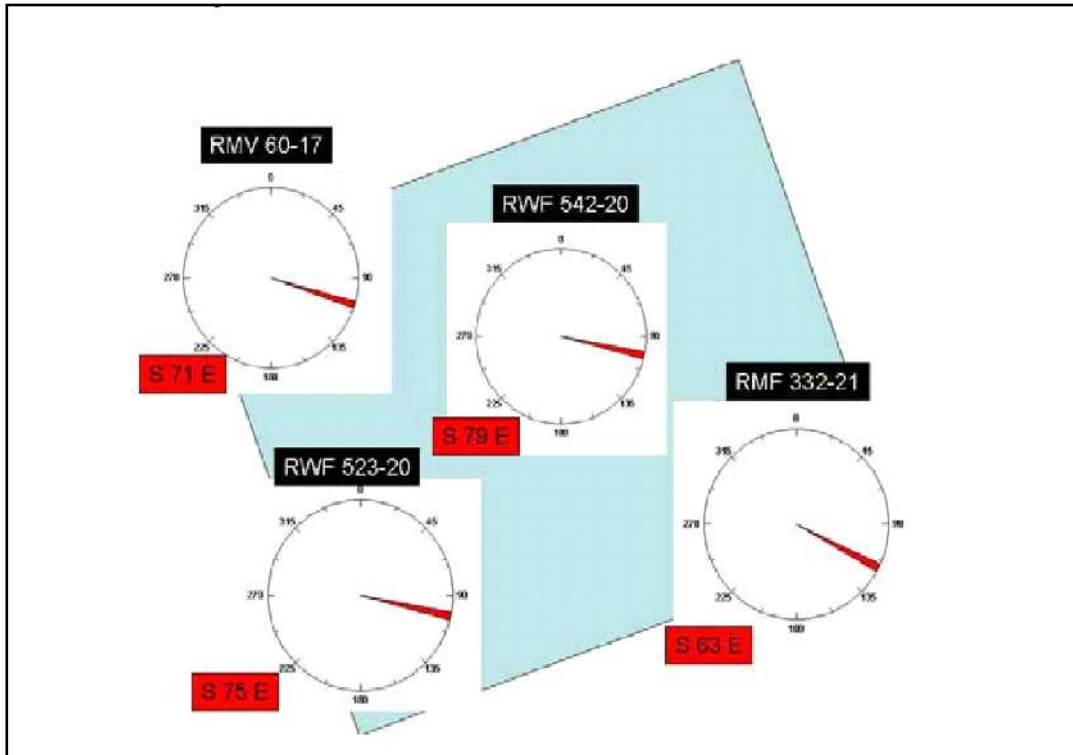


Figure 2.8: Average maximum horizontal stress direction from image logs and dipole sonic. (Picture courtesy Higgins 2006)

Matesic (2007) also interpreted borehole- image logs in the lower Williams Fork Formation at Rulison field. He concluded that the present day stress orientation determined from borehole breakouts and drilling induced fractures is N 70°W. He also found that the drilling induced fractures have the same orientation as the natural open fractures with the average dip of the open fractures around N70°W.

Praj Mazumdar (2007) estimated the fracture orientation at the reservoir zone from VSP data. The vertical receiver coverage for the VSP is mostly in the Williams Fork formation and he found that the fracture orientation in the reservoir zone is 65 degrees east of geographic North.

Figure 2.8 shows the dominant fracture orientation in Rulison field. The prestack P-wave data were divided into two volumes according to azimuth. The first one was from azimuths N60°E-N150°E & N240°E-N330°E., while the second volume was sorted orthogonal to the first volume. The sorting is based on the premise that any fractures opened at depth will be orientated normal to the direction of the minimum horizontal in situ stress Sayers (1990). Thus, after the sorting, I came up with two different data sets; one is approximately parallel to the fracture direction and the other is approximately perpendicular to the fracture direction. This sorting was necessary in order to be able to see the AVO response in the two-ideally perpendicular directions.

2.4 Data sorting and summing

Each of the azimuth-sorted volumes was resorted by CDP bin number and absolute value of offset. This created the near, mid and the far offset stack volumes for each of the two azimuth ranges. After sorting by offset, the data were summed using Diversity power stack. Diversity power stack is an effective stacking technique for attenuation of incoherent noise. This method utilizes the amplification of each trace as a function of the inverse ratio of the total power in each trace as compared to another trace. The amplified traces are then combined into a group of modified traces. Diversity power stacking is accomplished by prescaling the data by the inverse of its local power value prior to summation. The scalars are summed and averaged, and the stacked amplitude is divided by

the average of the values of the scalars. Figure 2.9 shows the offset limited data after stacking with the diversity stack algorithm.

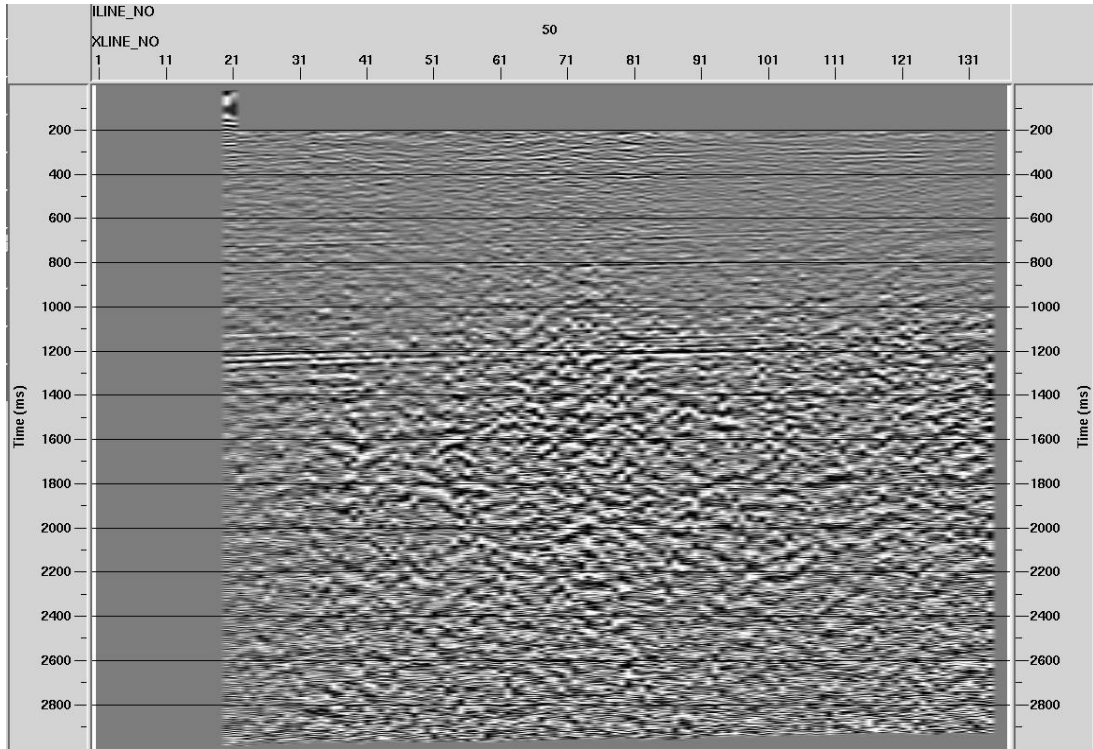


Figure 2.9: near-offset and azimuth limited stack, line 50

Stacking has greatly improved the signal to noise ratio of these data, strong reflections could be observed around 1200 ms. After these processes, I ended up with up with 6 different datasets: near-offset stack, mid-offset stack and the far-offset stack volumes for each of the two azimuths-separated data.

2.5 Migration

One of the ways to increase the signal-to-noise ratio of the data is to migrate the data. An f-k migration algorithm was used because f-k is an exact solution of the two-way wave equation. It assumes a constant velocity world, it handles dips up to 90 degrees, and it is a fast migration algorithm because it implements the migration through frequency-shift in the f-k domain. Figure 2.10 shows the data after migration. Some severe migration arching is present in the data. These artifacts are due to the fact that there are severe trace-to-trace amplitude variations in the data. The data given to migration had high amplitudes at the edge, leading to the arcs. Figure 2.9 shows the data given to migration; the trace-to-trace variation is not so distinct simply because the ProMax plotting had a built-in trace equalization program. In order to get a better migrated data I found it necessary to balance the amplitudes of this data before migration in order to reduce the trace-to-trace variations. Two ways to do this are to either apply an amplitude gain (AGC) before migration or to apply trace equalization to the data before migration.

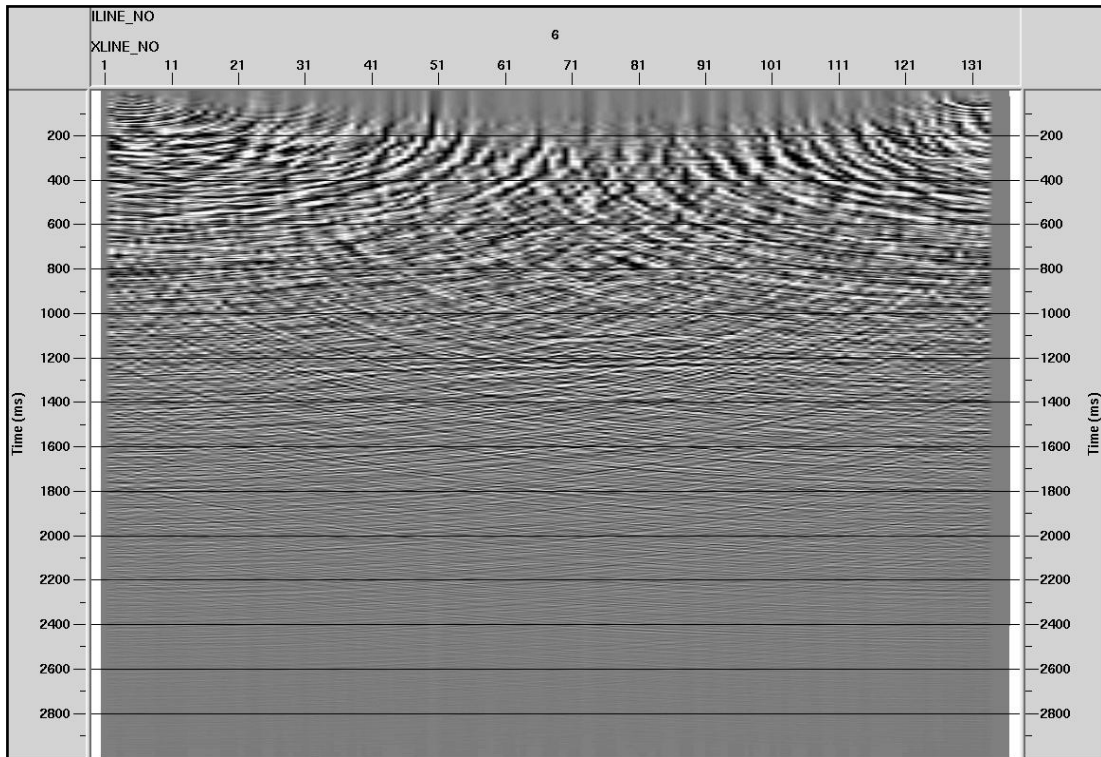


Figure: 2.10 migrated data

2.6 AGC before stack

AGC is a simple and effective means of improving the appearance of the data, but it can change the relative amplitudes within a CMP gather (Yu, 1985; Gassaway et al., 1986). A 500-ms median-based AGC was applied before stack and migration. This is done in order to reduce the effect of the anomalous high amplitudes in the data. AGC automatically varies the gain applied to trace samples as a function of sample amplitude within an AGC time window. The AGC operator length defines the length of the AGC window used for gain

computations. The AGC program moves the window down the trace sample-by-sample and calculates a scale factor at each location. For this AGC application, the scale factor is equal to the inverse of the median amplitude in the window. The scalar is applied to the sample at the beginning, center, or end of the AGC window. At the start and end of the trace, where there is less data in the window than the operator length requested, the window will be made as long as possible. Therefore, the window will grow at the start of the trace until it reaches the full operator length, and will remain constant until it reaches the end of the data, where it will shrink to progressively smaller value. Figure 2.11 shows the data after the application of AGC while Figure 2.12 shows the migrated data with AGC.

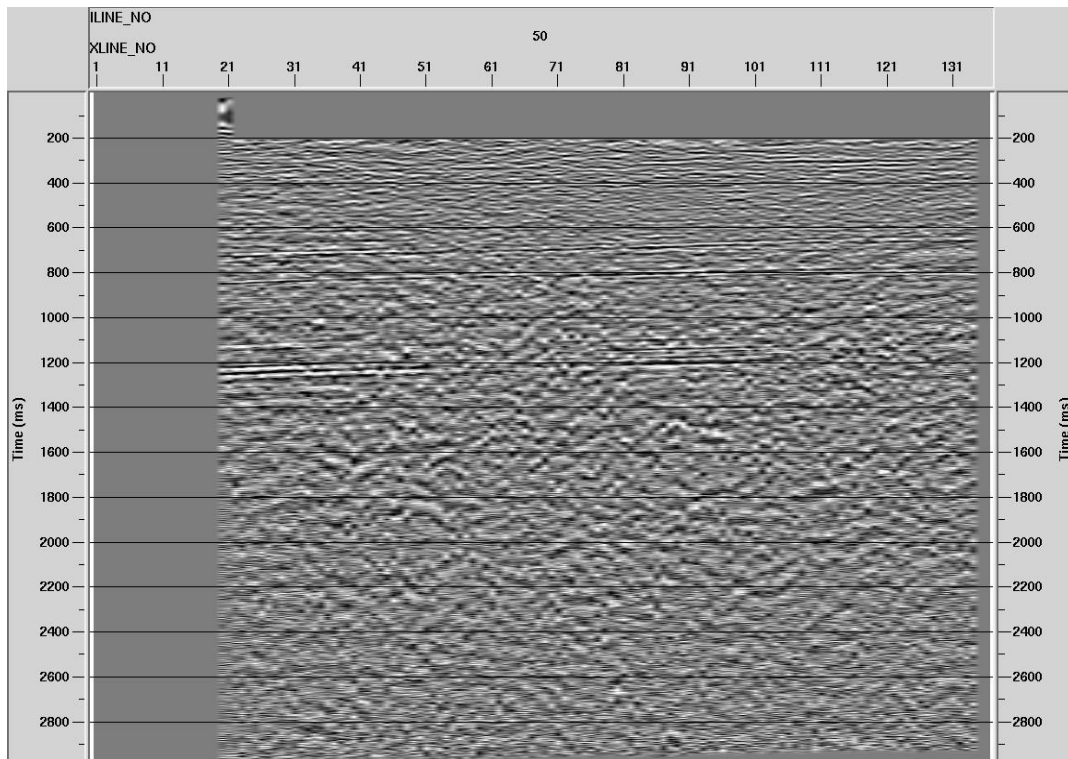
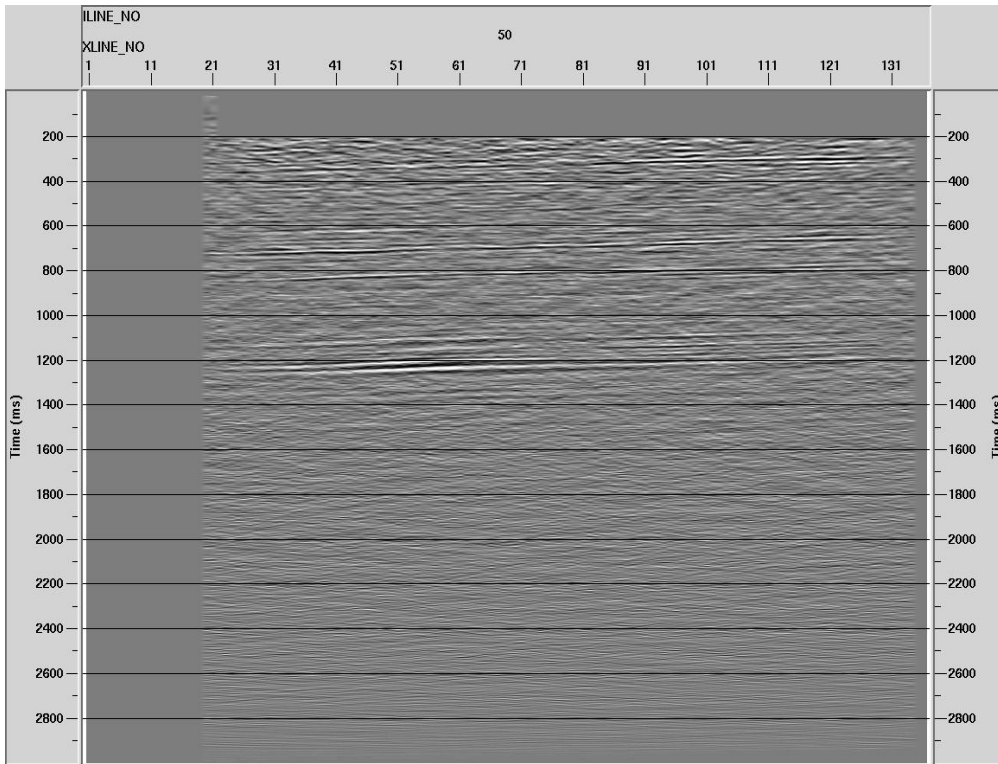


Figure 2.11: stack data with AGC applied



2.12 Migrated data with AGC Applied

2.7 Trace Equalization before stack

AGC applied a time dependent gain function to the data, Figure 2.11 shows that the amplitude in the shallow time were boosted and thus there is less trace-to-trace variation after the application of the AGC. In order to preserve the true amplitude of the data it is imperative to apply a time-invariant gain function to the data. So, I tried Trace Equalization, and I applied it to the data in Figure 2.9.

Trace Equalization computes and applies a trace-to-trace amplitude balancing

function. This algorithm was applied to the data before migration. The Trace Equalization algorithm in ProMax uses a single time window gate for each trace. The scalar in the window is computed on a Mean, RMS, or Maximum basis. I used the RMS option for this project. The scalar is defined as the ratio of desired RMS to the RMS that is computed from a specific time window. A separate scalar is computed for and applied to each trace. In this way, variations in amplitude between traces are reduced. Figure 2.13 shows the data with trace equalization applied before migration while Figure 2.14 shows the same data after migration. I will be using the data with trace equalization applied before migration for the AVO analysis.

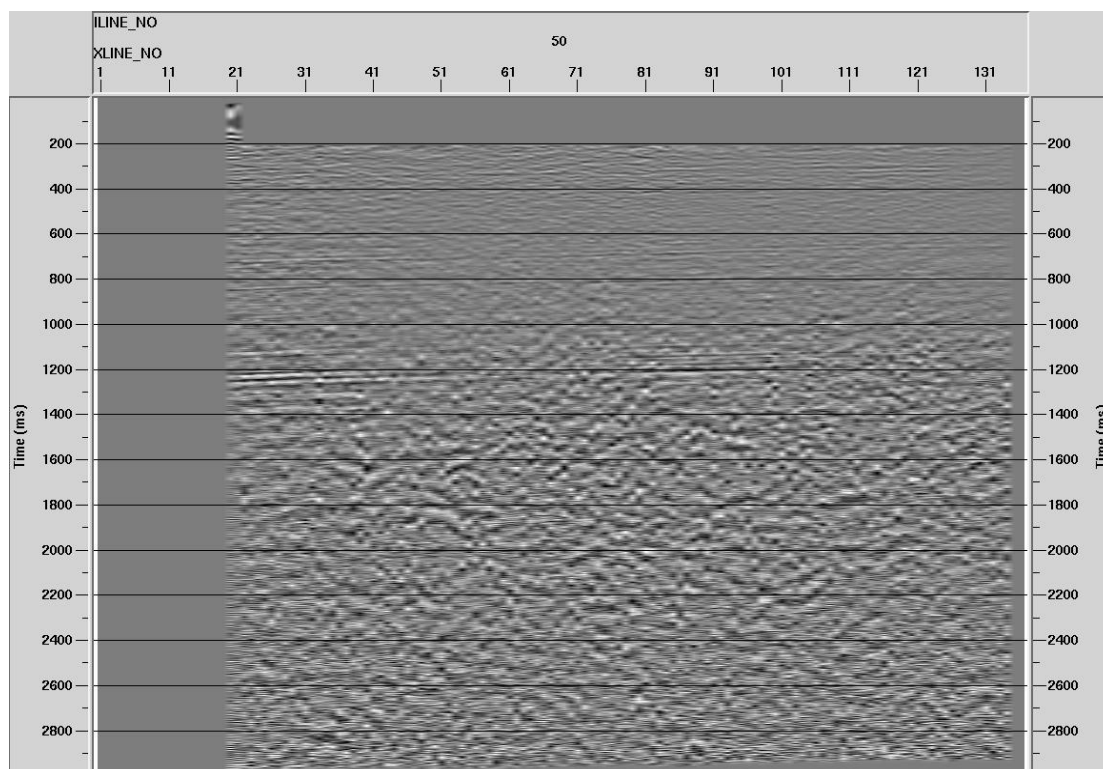


Figure 2.13 Stack data with Trace Equalization applied

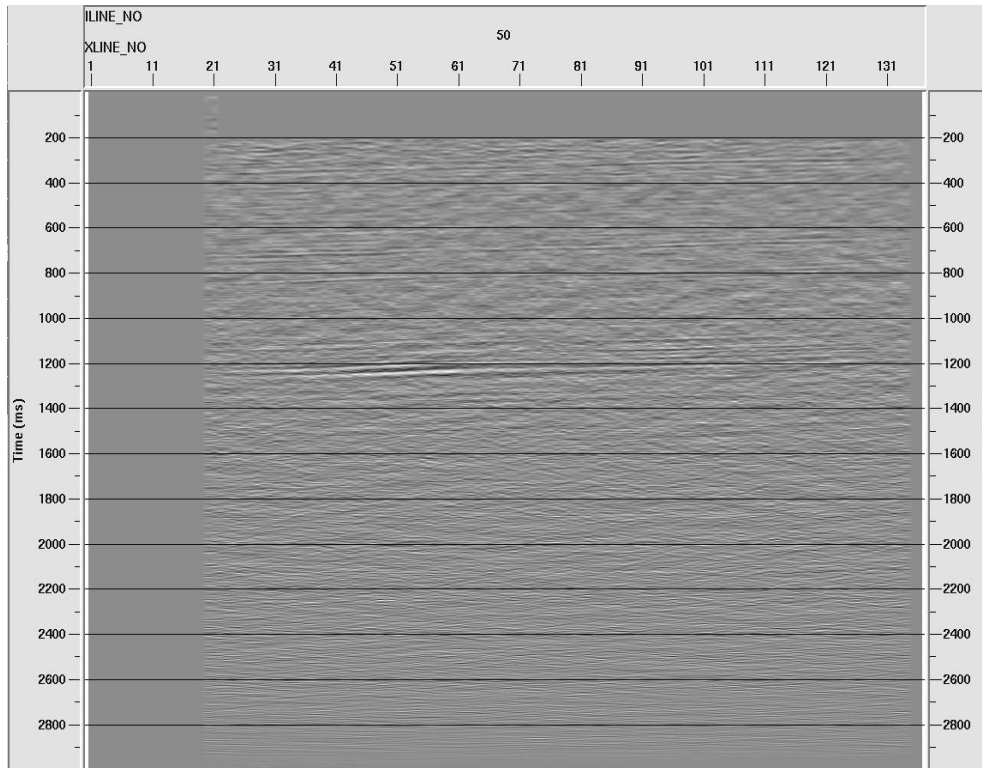


Figure 2.14 Migrated data with Trace Equalization applied.

Finally, each of the six offset and azimuth-limited volumes were converted to Seiswork volumes and they were input into the Landmark's AVO modeling software, Well Seismic Fusion, for the AVO analysis.

2.8 Summary

The prestack P-wave dataset for this project was contaminated with air blast. The air blast was suppressed using the air blast attenuation algorithm in ProMax. The dataset was divided according to azimuths; one was approximately parallel to the fracture direction and the other was approximately perpendicular to the fracture

direction. Each of the two azimuth-limited volumes was resorted by offset; trace equalization was applied to the data before stacking. The stack process created the near, the mid and the far offset stack volumes for each of the two azimuth ranges. The six stacked datasets were later migrated. The final outputs after migration will be used for the AVO analysis.

CHAPTER 3

AVO MODELING

3.0 Introduction

This chapter discusses some models that I created in order to determine the azimuthal AVO response for the reflections from the top of coal in Rulison field, Colorado from prestack P-wave data. The modeling is in 3-parts:

- The first part is analytically solving the reflection coefficients from the equations derived by Rueger for anisotropic media
- The second part is plotting the reflection coefficients for the top of coal as a function of the incidence angle,
- The last part of the modeling is generation of different synthetic seismograms.

This chapter also reviews the basics of AVO, the influence of seismic anisotropy on AVO, and the various symmetries used for characterizing fractured reservoirs.

3.1 AVO Modeling

AVO is defined as the variation in seismic reflection amplitude with change in distance between shotpoint and receiver that indicates differences in lithology and fluid content in rocks above and below the reflector. Amplitude variation with offset (AVO) is one of the techniques used by geophysicists to estimate thickness, porosity, density, velocity, lithology and fluid content of rocks. Figure

3.1 illustrates the input data to AVO analysis, the common midpoint gather.

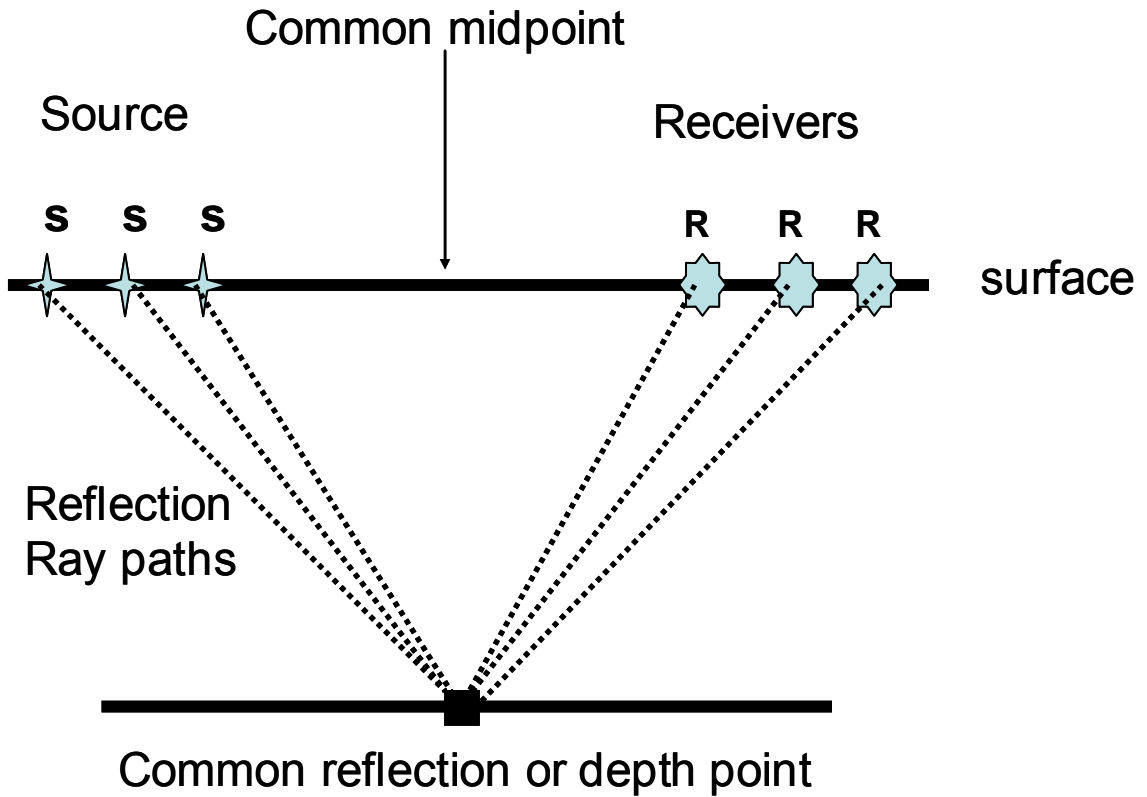


Figure 3.1 CMP gather

The theory behind AVO in clastic (sandstone) rocks is straightforward. Gas within the pore space of a clastic rock may substantially lower the compressional P-wave velocity of the rock, but leaves the shear-wave (S) velocity relatively unaffected. The change in the ratio of P-wave velocity to S-wave velocity causes the partitioning of an incident wave in the case of a gas- sand/shale or gas -sand/ wet sand reflector to differ from most other reflectors.

3.2 AVO Theory and History

When seismic waves travel down in the earth and encounter layer boundaries with density and velocity contrasts, the energy of the incident wave is partitioned at each boundary. Part of the incident energy associated with a P-wave source might be mode converted to reflected and transmitted S-wave energy provided that the lower medium is not fluid. For the solid-solid case, both the P-wave and the S-wave energy are partly reflected and partly transmitted through each of these boundaries. The fraction of the incident energy that is reflected also depends upon the angle of incidence. The analysis of amplitudes as a function of incidence angle is what is referred to as an AVO analysis. (Figure 3.2)

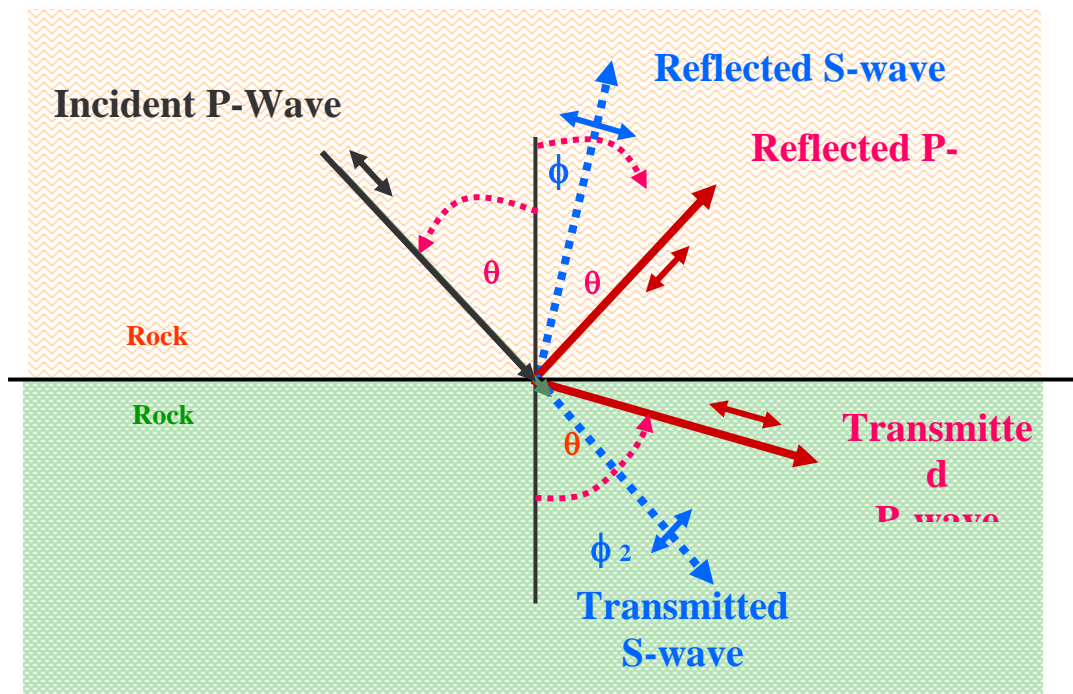


Figure 3.2: Reflected and transmitted rays caused by a P-wave incident at a boundary between two isotropic media. (Picture modified from Mike Graul's AVO short course).

Zoeppritz (1919) derived a set of equations relating the reflected and the transmitted displacement amplitudes at an interface for an incident plane waves. These equations were derived from basic physical principles, using Snell's law, the continuity of displacement, and the continuity of stress across each layer. These equations give the reflection and transmission coefficients for plane waves as a function of angle of incidence and three independent elastic parameters (compressional velocity, shear-wave velocity and density), on each side of the reflecting interface.

Using these relations, Koefoed (1955) computed amplitudes as functions of changes in the Poisson's ratios. Koefoed work showed that it is the contrasts in Poisson's ratio across an interface that controls the variations in amplitude with offset. Poisson's ratio is a function of V_p/V_s ratio given by:

$$\sigma = \frac{0.5\left(\frac{V_p}{V_s}\right)^2 - 1}{\left(\frac{V_p}{V_s}\right)^2 - 1} \quad (3.1)$$

Ostrander (1982) demonstrated that Poisson's ratio had a strong influence on changes in reflection coefficient versus angle of incidence, and that AVO analysis can often distinguish between gas-related amplitude anomalies and other types of amplitude anomalies.

Shuey (1985) derived a linear simplification of the Zoeppritz equations. Shuey rewrote the Zoeppritz equations presented in Aki and Richards (1980) as

$$R_p(i) = A + B \sin^2 i + C \sin^2 i \tan^2 i \quad (3.2)$$

where i is the angle of incidence of the incoming waves. The coefficient A is the normal incidence reflection coefficient (or intercept), B is the initial slope of the reflection coefficient curve (or AVO gradient), and C is referred to as the curvature term. Shuey's (1985) linear simplification of the Zoeppritz equations allowed the processing of large data sets quickly, and it also increases the computation speed of AVO attributes.

In practical problems, AVO analysis is performed on measurements of seismic amplitudes, as opposed to direct reflection coefficient measurement. There are multitudes of phenomena that alter these seismic recorded amplitudes and these include: geometric dilution, instrumentation, field gain, spherical divergence, source strength, transmission losses, multiples, absorption, bed thickness, array directivity, salt velocity lenses and scattering. For a seismic trace to be equal to a reflection coefficient series, a lot of factors must be met. These factors include:

- Complete elimination of noise and multiples
- Removal of spherical divergence, transmission losses and other scaling factors

In the real world, it is obvious that that these requirements can never be achieved even after processing the data. Some of these effects will be removed while some will still remain in the data. Another important factor that might affect AVO

analysis is seismic anisotropy. It is quite imperative to discuss the effects of seismic anisotropy on AVO and to determine how these effects can actually change the elastic parameters we try to recover.

3.3 Anisotropy and AVO

Conventional AVO analysis needs to be modified if anisotropy is present on either side of the reflection boundary. Research studies show that the presence of seismic anisotropy can significantly distort AVO analysis (Wright, 1986; Banik, 1987; Kim et al., 1993). Samec, et. al (1990) studied the effect of anisotropy on wave propagation in fully anisotropic media and they showed that it can be inappropriate to neglect the effect of seismic anisotropy in modeling of prestack data. They showed that the expected trend in reflection coefficient amplitude versus angle of incidence may be reversed (phase reversal) from the elastic isotropic case if no special care is taken to compensate for source radiation pattern, anelastic or anisotropic energy focusing and phase distortions which are due to wave propagation in anelastic anisotropic media.

Anisotropy in sedimentary rocks can be caused by the following factors:

1. The presence of crystals of particular symmetry within an isotropic matrix
2. The presence of thin laminations on a small scale compared to the seismic wavelength

3. The presence of microfracturing in rocks along the principal axes of present and past regional stresses.

4. Non-hydrostatic stress (Tsvankin 2001)

For this research purpose, I will focus on fracture-induced anisotropy because fracture-induced anisotropy is the most important anisotropy for hydrocarbon exploration.

3.4 Anisotropy Symmetry

There are two major models that are used in the oil industry for describing fractured-induced anisotropy, these are:

1. Transverse Isotropy and
2. Orthorhombic Symmetry

Transverse isotropy is one of the models for describing fractures in reservoir rocks. All seismic signatures in this model depend on the angle between the propagation direction and the symmetry axis. Any plane that contains the symmetry axis represents a plane of mirror symmetry; the other symmetry plane called the isotropy plane is perpendicular to the first symmetry plane (Tsvankin 2001).

3.4.1 Transversely isotropic media with vertical axis of symmetry (VTI)

Laminated rocks or horizontal layers of rocks, e.g. shale formations, are considered VTI media. The AVO response in this medium is azimuthally independent i.e., for a given angle of incidence, the reflection amplitude does not vary with azimuth. Figure 3.3 shows the VTI model, where x_3 is the vertical direction.

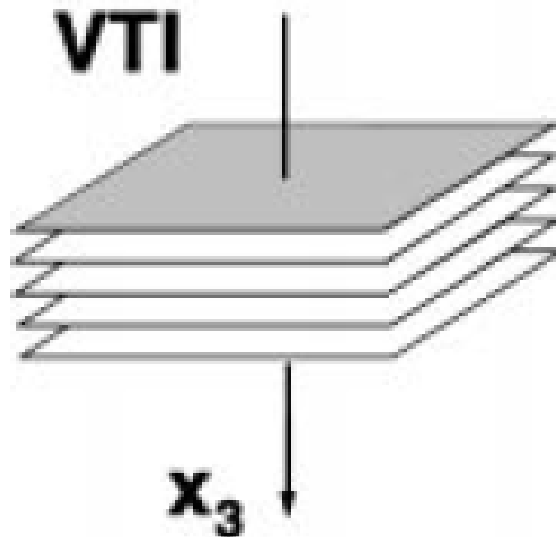


Figure 3.3 VTI model has a vertical axis of rotational symmetry. (From Rueger, 1997)

The elastic coefficients below describe how much stress must be applied to obtain a standard deformation in a given direction. The stiffness matrix for VTI media (Mugrave, 1970) can be represented as

$$C_{IJ} = \begin{matrix} & C_{11} & C_{12} & C_{13} & 0 & 0 & 0 \\ & C_{12} & C_{11} & C_{13} & 0 & 0 & 0 \\ & C_{13} & C_{13} & C_{13} & 0 & 0 & 0 \\ & 0 & 0 & 0 & C_{44} & 0 & 0 \\ & 0 & 0 & 0 & 0 & C_{44} & 0 \\ & 0 & 0 & 0 & 0 & 0 & C_{66} \end{matrix}$$

$$\text{Where } C_{12}=C_{11}-2C_{66} \quad C_{23}=C_{13} \quad ,C_{22}=C_{11} \quad C_{55}=C_{44} \quad (3.3)$$

The degree of anisotropy in the VTI medium is a function of how much the constant C_{11} , C_{33} , the constant C_{44} , C_{66} and the constant C_{12} , C_{13} differ from each other. The VTI medium phase velocity ($v(\theta)$) for compressional and shear-waves vary from the symmetry axis ($\theta = 0^\circ$) towards the horizontal ($\theta = 90^\circ$) direction, according to the following equations:

For P-waves

$$V_p(0) = \sqrt{\frac{C_{33}}{\rho}} \quad ,$$

$$V_p(90) = \sqrt{\frac{C_{11}}{\rho}} \quad ,$$

For S-waves

$$V_{sh}(0) = V_{sv}(0) = \sqrt{\frac{C_{44}}{\rho}} \quad ,$$

$$V_{sh}(90) = \sqrt{\frac{C_{66}}{\rho}},$$

$$V_{sv}(90) = \sqrt{\frac{C_{44}}{\rho}},$$

3.4.2 Transversely isotropic medium with horizontal axis of symmetry (HTI)

Physical reasons for a media with an HTI symmetry includes systems of parallel vertical penny-shaped cracks embedded in an isotropic background. The HTI model has two mutually orthogonal vertical planes of symmetry: the symmetry-axis plane and the isotropy plane (Figure 3.4). This produces different P-wave reflection amplitudes in the two vertical planes and thus leads to azimuthally dependent AVO responses.

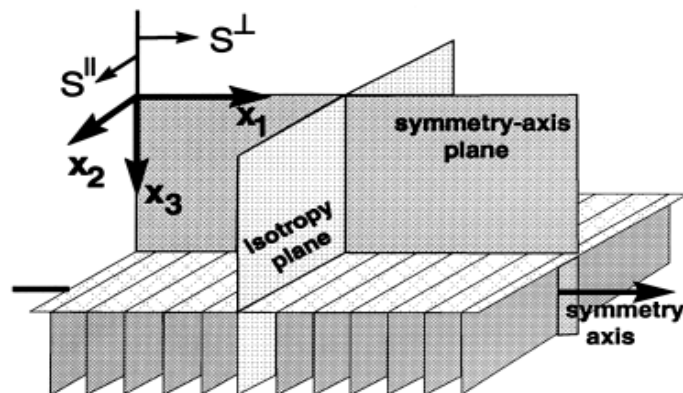


Figure 3.4 Sketch of an HTI model (From Tsvankin 2001)

The stiffness matrix (Mugrave 1970) for an HTI has the form:

$$C_{ij} = \begin{matrix} & C_{33} & C_{13} & C_{13} & 0 & 0 & 0 \\ & C_{13} & C_{11} & C_{12} & 0 & 0 & 0 \\ & C_{13} & C_{23} & C_{11} & 0 & 0 & 0 \\ C_{ij} = & 0 & 0 & 0 & C_{66} & 0 & 0 \\ & 0 & 0 & 0 & 0 & C_{44} & 0 \\ & 0 & 0 & 0 & 0 & 0 & C_{44} \end{matrix}$$

3.4.3 Orthorhombic Symmetry

Media with orthorhombic symmetry have three mutually orthogonal planes of mirror symmetry. This symmetry describes several models typical for fractured reservoirs, including those containing a system of parallel vertical cracks in a VTI background (Figure 3.5), as well as two to three orthogonal crack systems.

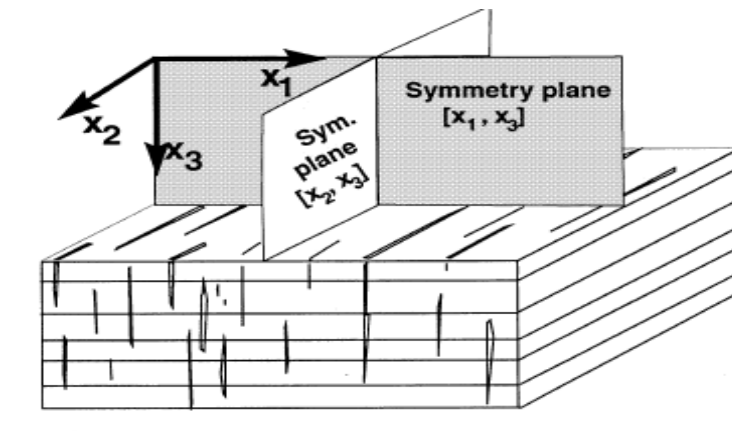


Figure 3.5 Orthorhombic model (From Tsvankin 2001)

The stiffness matrix (Mugrave 1970) for orthorhombic media can be represented as:

$$C_{ij} = \begin{matrix} C_{11} & C_{12} & C_{13} & 0 & 0 & 0 \\ C_{12} & C_{22} & C_{23} & 0 & 0 & 0 \\ C_{13} & C_{23} & C_{33} & 0 & 0 & 0 \\ 0 & 0 & 0 & C_{44} & 0 & 0 \\ 0 & 0 & 0 & 0 & C_{55} & 0 \\ 0 & 0 & 0 & 0 & 0 & C_{66} \end{matrix}$$

3.5 Reflection Coefficient in Anisotropic Medium

Conventional AVO analysis is based on analytical expressions for P-wave reflection coefficients in isotropic media. This reflection coefficient has to be modified if anisotropy is present in either side of the reflection boundary just as we have between the overburden and the top of coal in Rulison Field. In this section, I will review some of the recent work that was done on anisotropic reflection coefficients equations because I will be making use of these equations for synthetic modeling. An incident plane wave at the boundary between two anisotropic media can generate reflected quasi-P-wave and quasi-S-waves as well as transmitted quasi-P-wave and quasi-S-waves (Auld, 1990). (“Quasi-P-wave” refers to the fact that, in anisotropic media, the P- wave is not polarized in either the slowness or ray directions.

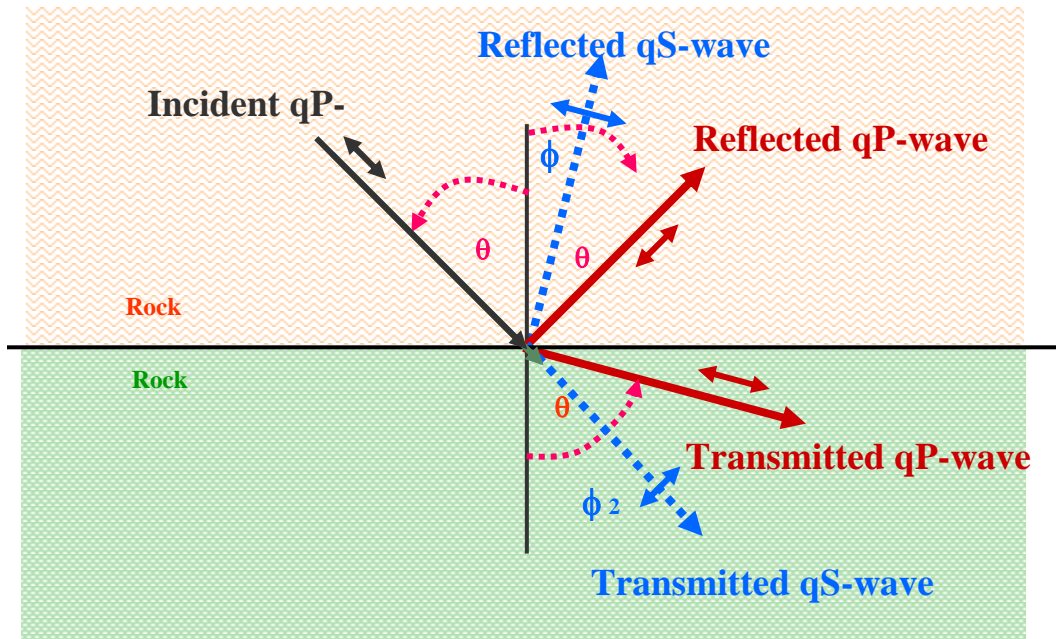


Figure 3.6 Reflected and transmitted rays caused by a P-wave incident at a boundary between two anisotropic media (Picture modified from Mike Graul's).

Also, the SV-wave in anisotropic media is not polarized normal to the slowness and ray directions). Generally, the reflection coefficient might vary with both offset and azimuth. The amplitude variation with offset and azimuth (AVOZ) can be detected by 3D wide-azimuth seismic data. Normally, for a wave traveling in anisotropic media, there will be out-of-plane motion unless the wave is in a symmetry plane. These symmetry planes include all vertical planes in VTI, HTI and orthorhombic media. In this case, quasi-P-waves and quasi-S-waves in the symmetry are uncoupled from the quasi-S-wave polarized transversely to the symmetry plane. For weakly anisotropic media, analytical formulas by (Banik, 1987; Thomsen 1993; Rueger, 1995, 1996; Chen, 1995) can be used to compute AVOZ responses at the interface of anisotropic media that can be HTI, VTI or orthorhombic. I used the equations derived by (Rueger 1995 and Rueger

1997). These formulas give more insights on the dependence AVOZ on anisotropy.

Thomsen (1986) introduced a set of notation for weakly transversely isotropic media with density. He replaced the five independent stiffness coefficients with two vertical velocities and three dimensionless anisotropic parameters:

$$\alpha = \sqrt{\frac{C_{33}}{\rho}} \quad (3.4)$$

$$\beta = \sqrt{\frac{C_{44}}{\rho}} \quad (3.5)$$

$$\varepsilon = \frac{C_{11} - C_{33}}{2C_{33}} \quad (3.6)$$

$$\gamma = \frac{C_{66} - C_{44}}{2C_{44}} \quad (3.7)$$

$$\delta = \frac{(C_{13} - C_{44})^2 - (C_{33} - C_{44})^2}{2C_{33}(C_{33} - C_{44})^2} \quad (3.8)$$

α and β are the vertical (symmetry-axis) velocities of P-waves and shear waves respectively. γ denotes the fractional difference between horizontal and vertical SH-wave velocity, ε denotes the fractional difference between horizontal and vertical P-wave velocity, and δ describes the variations of P-wave velocity with phase angle for near vertical propagation. One of the advantages of Thomsen's

notations is that the anisotropic parameters γ , ε and δ go to zero for an isotropic medium, therefore characterizing the strength of the anisotropy.

3.5.1 P-P Reflections in VTI Media

Thomsen (1986) wrote the linearized version of the phase velocities of waves propagating in VTI medium in terms of the anisotropic coefficients as

$$V_p(\theta) = \alpha \left[1 + \delta \sin^2 \theta \cos^2 \theta + \sin^4 \theta \right]; \quad (3.9)$$

$$V_{sv}(\theta) = \beta \left[1 + \frac{\delta^2}{\beta^2} (\varepsilon - \delta) \sin^2 \theta \cos^2 \theta \right]; \quad (3.10)$$

$$V_{sh}(\theta) = \beta \left[1 + \gamma \sin^2 \theta \right]; \quad (3.11)$$

V_p , V_{sv} , and V_{sh} are the vertical P-wave velocity, vertical S-wave velocity and the horizontal S-wave velocity respectively. These equations explain the influence of anisotropy on seismic wave fields. (Thomsen, 1993) also gave the P-wave reflection coefficient for weak transversely anisotropic media (VTI) in the limit of small impedance contrast as

$$R_{pp}(\theta) = R_{pp-iso} + R_{pp-aniso} \quad (3.12)$$

$$(3.12) \quad R_{pp-iso}(\theta) = \frac{1}{2} \left(\frac{\Delta Z}{Z} \right) + \frac{1}{2} \left\{ \frac{\Delta \alpha}{\alpha} - \left(\frac{2\beta}{\alpha} \right)^2 \frac{\Delta G}{G} + \sin^2 \theta + \frac{1}{2} \left\{ \frac{\Delta \alpha}{\alpha} \right\} \sin^2 \theta \tan^2 \theta \right\} \quad (3.13)$$

$$R_{pp_aniso}(\theta) \approx \frac{\Delta\delta}{2} \sin^2 \theta + \frac{\Delta\varepsilon}{2} \sin^2 \theta \tan^2 \theta \quad (3.14)$$

$$\theta = \left(\frac{\theta_1 + \theta_2}{2} \right) \quad \bar{Z} = \left(\frac{Z_1 + Z_2}{2} \right) \quad \bar{\rho} = \left(\frac{\rho_1 + \rho_2}{2} \right) \quad \bar{\alpha} = \left(\frac{\alpha_1 + \alpha_2}{2} \right)$$

$$\bar{\beta} = \left(\frac{\beta_1 + \beta_2}{2} \right) \quad \bar{G} = \left(\frac{G_1 + G_2}{2} \right) \quad \Delta\varepsilon = \varepsilon_2 - \varepsilon_1 \quad \Delta\rho = \rho_2 - \rho_1$$

$$\Delta\alpha = \alpha_2 - \alpha_1 \quad \Delta\beta = \beta_2 - \beta_1 \quad \Delta G = G_2 - G_1 \quad \Delta Z = Z_2 - Z_1$$

$$\Delta\gamma = \gamma_2 - \gamma_1 \quad \Delta\delta = \delta_2 - \delta_1 \quad G = \rho\beta^2 \quad Z = \rho\alpha$$

(Rueger, 1995) derived a similar P-wave reflection coefficients equation for weak transversely anisotropic media (VTI) from Aki and Richards 1980's expression for isotropic media assuming a small impedance contrast across the interface.

Rueger's expression is given as:

$$R_p(\theta) = \frac{1}{2} \frac{\Delta Z}{\bar{Z}} + \left\{ \frac{\Delta V_{po}}{\bar{V}_{po}} - \left(\frac{2\bar{V}_{so}}{\bar{V}_{po}} \right)^2 \frac{\Delta G}{\bar{G}} + \Delta\delta \right\} \sin^2 \theta + \frac{1}{2} \left\{ \frac{\Delta V_{po}}{\bar{V}_{po}} + \Delta\varepsilon \right\} \sin^2 \theta \tan^2 \theta \quad (3.15)$$

Where θ denotes the incident phase angle, $Z = \rho V_{P0}$ is the vertical P-wave impedance, and $G = \rho V_{so}^2$ denotes the vertical shear modulus. The differences in anisotropy across the boundary are given as:

$$\Delta\delta = \delta_2 - \delta_1, \quad \Delta\varepsilon = (\varepsilon_2 - \varepsilon_1)$$

Equation 3.15 derived by (Rueger, 1995) differs from Thomsen's result in that the difference in anisotropy parameter $\Delta\delta$ does not appear in the $\sin^2\theta\tan^2\theta$ term. In equation 3.15, $\Delta\delta$ enters the $\sin^2\theta$ term and Rueger explained that the $\Delta\delta$ describes the influence of anisotropy on the small-angle reflection coefficient and the AVO slope. He also concluded that $\Delta\varepsilon$ is responsible for the $\sin^2\theta\tan^2\theta$ term and hence it is more dominant at larger incidence angles. His work corroborated the fact that δ controls the influence of anisotropy on near-vertically traveling P-waves, while ε dominates near-horizontal wave propagation. Equation 3.15 was previously discussed by Thomsen (1993) and Blangy (1994), but with the wrong $\sin^2\theta\tan^2\theta$ term. Rueger pointed out that the presence of $\Delta\delta$ in Thomsen's result may cause inaccuracies at large angles, specifically for nonzero values of $\Delta\delta$. He also pointed out that Thomsen's approximation does not work well for angles larger than 20 degrees and will break down for angles greater than 45 degrees.

3.5.2 Reflections in HTI Media

In HTI media, reflectivity will vary with azimuth (θ), offset, and incident angle. Rueger (1995, 1996) and Chen (1995) derived the P-wave reflection coefficient in the symmetry planes for reflections at the boundary of two HTI media sharing the same symmetry axis. The reflection coefficient was derived from Aki Rueger derived the P-wave reflection coefficient for the symmetry-axis plane of an HTI medium as

$$R_p^{sym}(\theta) = \frac{1}{2} \frac{\Delta Z}{Z} + \left\{ \frac{\Delta\alpha}{\alpha} - \left(\frac{2\beta}{\alpha} \right)^2 \left(\frac{\Delta G}{G} - 2\Delta\gamma \right) + \Delta\delta^{(v)} \right\} * \sin^2 \theta + \frac{1}{2} \left\{ \frac{\Delta\alpha}{\alpha} + \Delta\varepsilon^{(v)} \right\} \sin^2 \theta \tan^2 \theta \quad (3.16)$$

where θ again denotes the incident phase angle. This equation is valid for general HTI media. Thomsen (1995) has shown that the anisotropy coefficients: $\delta^{(v)}$, $\varepsilon^{(v)}$ and γ are not independent in the case of fracture-induced anisotropy. The $^{(v)}$ exponent means that the Thomsen's parameters were defined with respect to vertical.

3.5.3 P-Reflections in Orthorhombic Media

Rueger (1996) estimated the reflection coefficient in the $[x_1; x_3]$ -plane of media with orthorhombic symmetry from the VTI equations because the reflection coefficients in the symmetry planes of orthorhombic media are the same as in VTI media when the upper and lower media have the same orientations of the symmetry- planes. The P-wave reflection coefficient in the $[x_1; x_3]$ -symmetry-plane of orthorhombic media is given by Rueger as:

$$R_p^{[x_1, x_3]}(i) = \frac{1}{2} \frac{\Delta Z}{Z} + \frac{1}{2} \left[\frac{\Delta \alpha}{\alpha} - \left(\frac{2\beta^\perp}{\alpha} \right)^2 \frac{\Delta G^\perp}{G^\perp} + \Delta \delta^{(2)} \right] \sin^2 i + \frac{1}{2} \left(\frac{\Delta \alpha}{\alpha} + \Delta \varepsilon^{(2)} \right) \sin^2 i \tan^2 i, \quad (3.18)$$

$$\text{with } \beta^\perp = \sqrt{C_{55} / \rho}, \quad G^\perp = \rho \beta^{\perp 2} \quad (3.19)$$

He also derived the P wave reflection coefficient for the $[x_2; x_3]$ - symmetry plane in orthorhombic media as

$$Rp^{[s2,s3]}(i) = \frac{1}{2} \frac{\Delta Z}{Z} + \frac{1}{2} \left[\frac{\Delta \alpha}{\bar{\alpha}} - \left(\frac{2\bar{\beta}}{\bar{\alpha}} \right)^2 \frac{\Delta G}{\bar{G}} + \Delta \delta^{(1)} \right] \sin^2 i + \frac{1}{2} \left(\frac{\Delta \alpha}{\bar{\alpha}} + \Delta \varepsilon^{(1)} \right) \sin^2 i \tan^2 i, \quad (3.20)$$

This result can be applied to the interfaces between isotropic, VTI, HTI, and orthorhombic media.

Similarly, the anisotropic parameters in orthorhombic media are given by Chen (1995) and Tsvankin (1997) as follows:

$$\varepsilon^{(1)} = \frac{C_{22} - C_{33}}{2C_{33}} \quad (3.21)$$

$$\varepsilon^{(2)} = \frac{C_{11} - C_{33}}{2C_{33}} \quad (3.22)$$

$$\delta^{(1)} = \frac{(C_{23} - C_{44})^2 - (C_{33} - C_{44})^2}{2C_{33}(C_{33} - C_{44})^2} \quad (3.23)$$

$$\delta^{(2)} = \frac{(C_{13} - C_{55})^2 - (C_{33} - C_{44})^2}{2C_{33}(C_{33} - C_{55})^2} \quad (3.24)$$

$$\gamma^{(2)} = \frac{C_{44} - C_{55}}{2C_{55}} \quad (3.25)$$

The parameters $\varepsilon^{(1)}$ and $\delta^{(1)}$ are Thomsen's parameters for VTI media in the

2-3 plane, while $\varepsilon^{(2)}$ and $\delta^{(2)}$ are Thomsen's parameters for VTI media in the

1-3 plane. $\gamma^{(2)}$ is the VTI parameter γ in the 1-3 plane.

This preceding section discusses: the various symmetries used for characterizing fractured reservoirs and the various reflection coefficient equations in anisotropic media. This background information was necessary because most of these reflection coefficient equations will be used for the AVO modeling.

3.6 Reflectivity Modeling Code

Synthetic seismograms will be computed using the reflectivity method in order to see the azimuthal dependence of the AVO from the prestack P-wave data. The reflectivity code, Anisynpa, is a full-waveform modeling algorithm which is designed to simulate exact 3D wavefields for horizontally layered anisotropic media. The reflectivity code was originally developed by Dennis Corrigan at ARCO and was later modified by Andreas Rueger while working on his PhD Thesis at the Center for Wave Phenomena, Colorado School of Mines. The inputs to this code are: the layer type, the layer elastic parameters i.e V_{ij} s, offset distance, and the wavelet, where the V_{ij} is defined as

$$V_{ij} = \sqrt{\frac{C_{ij}}{\rho}} \text{ Where } \rho \text{ is density}$$

3.7 Input data for Synthetic Modeling and Petrophysical Analysis

I chose well RMF 441-20 for modeling because the dipole sonic logs were acquired at this well. The well has a density log, a gamma ray log and a P-wave sonic log. Figure 3.7 shows a P-wave sonic log and density log from 7300 ft to 7900 ft. This is the coal interval from the top of the Cameo formation to the top of the Rollins formation. The coal is characterized by low density, low P and S-wave velocities. Typical coal density is around 1.4 g/cc. This low density and velocities are responsible for the high impedance contrast that exists between the coal and the surrounding lithology. The presence of fractures in the rock increases the V_p/V_s ratio (or Poisson's ratio) because fractures reduce the shear modulus of the rock more than its density. If gases fill the fractures, then the Poisson's ratio further increases; this is because the presence of gas will decrease the bulk modulus of the rock and thus decrease the P-wave velocity (Ramos, 1993). The coals in Rulison field are filled with dry gas with almost zero water saturation. This is the major reason why I will not spend any time to determine the effect of saturation changes on the cracks in Rulison.

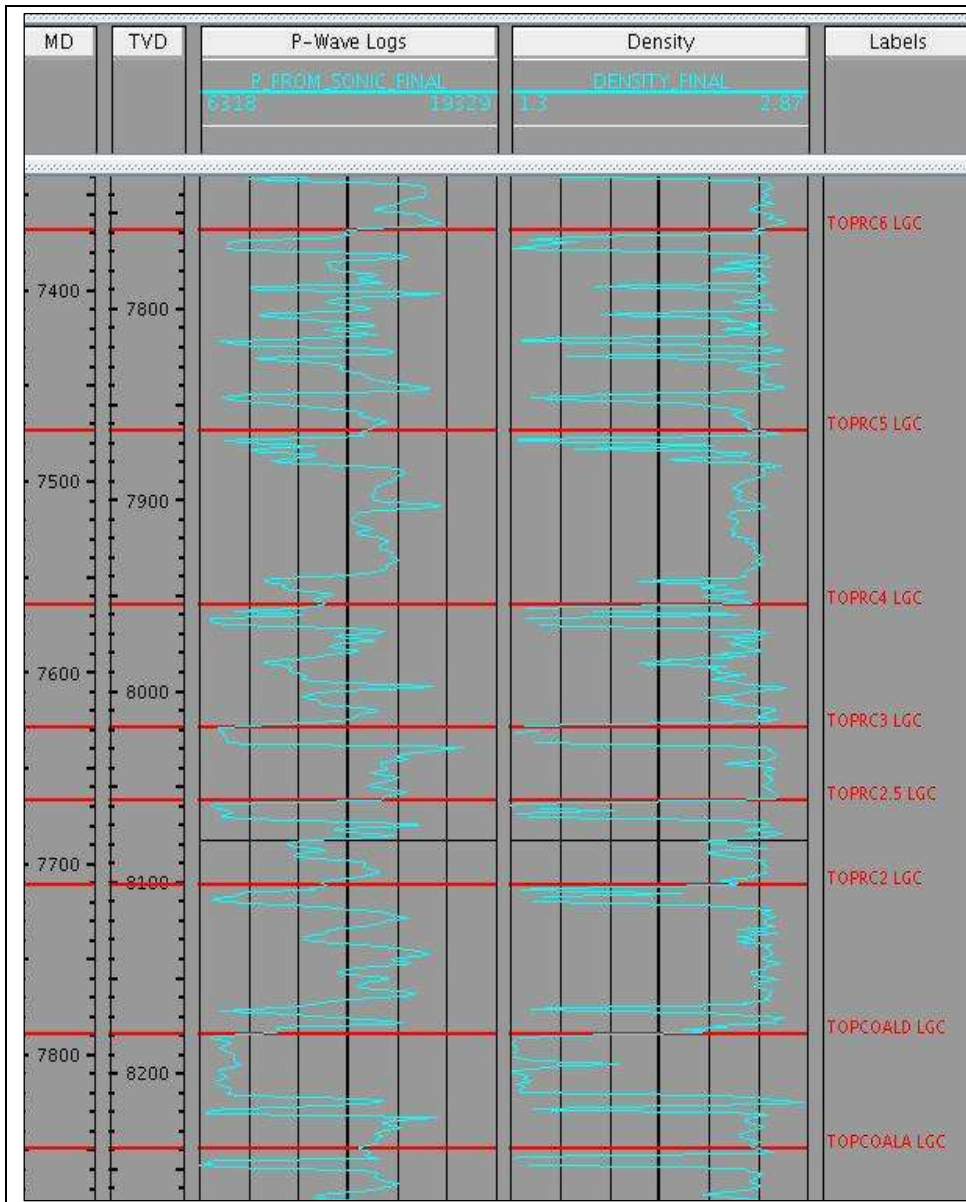


Figure 3.7 P-wave log and density log for the coal interval. The red horizontal lines show the tops of the various coal intervals.

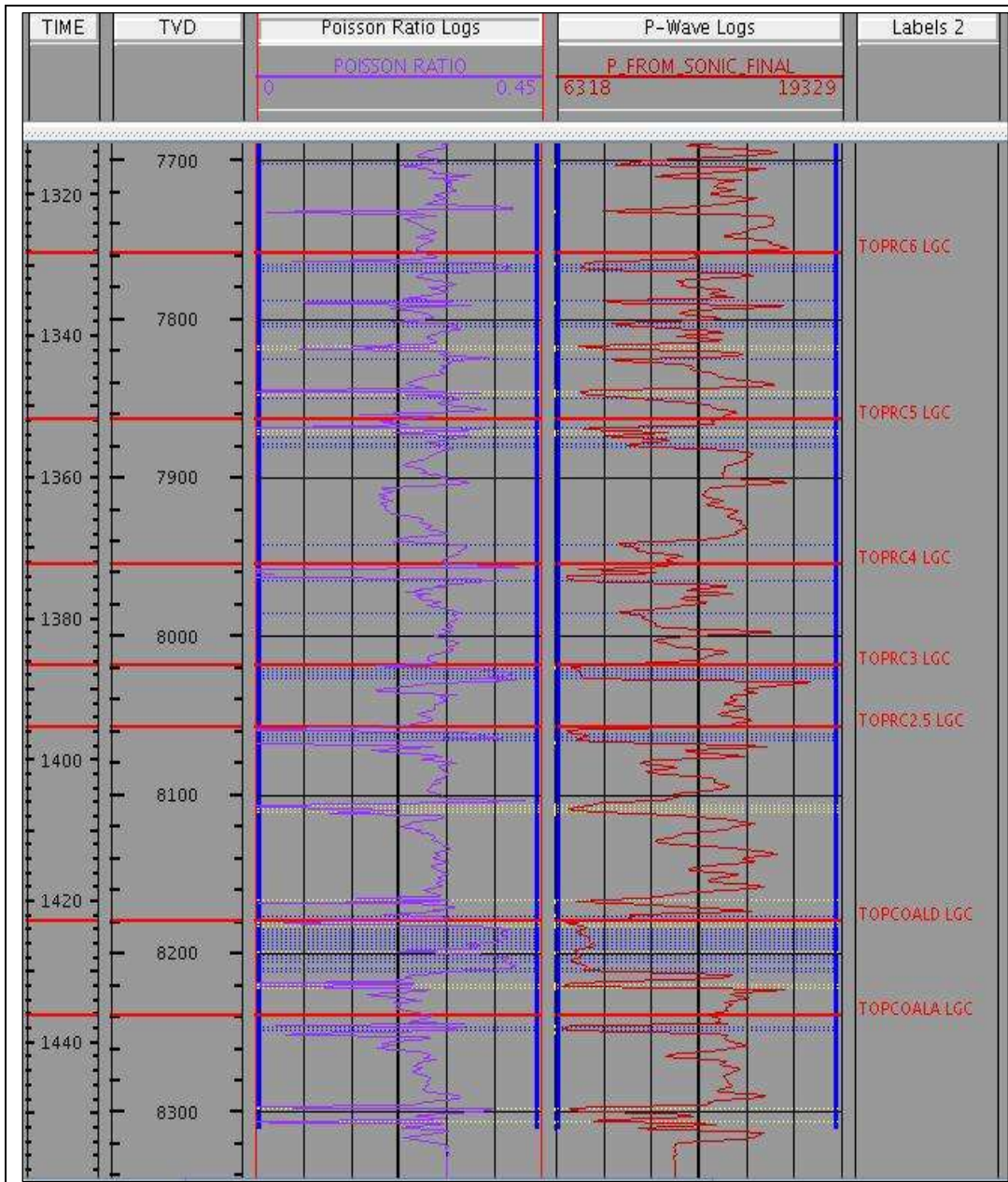


Figure 3.8 Poisson ratio log and P-wave log for the coal interval. The blue stipple highlights the various coal intervals while the red horizontal line shows the tops of the various coal intervals.

3.8 Intercept and Gradient Computation from well log

Richard Verm and Fred Hilterman (1995) reduced Shuey's AVO equation to two terms; normal incidence reflectivity (NI) and the far-offset reflectivity (PR).

Their simplification of the linear approximation of the isotropic reflection coefficient is given as:

$$RC(i) \cong NI \cos^2 i + PR \sin^2 i \quad 3.26$$

where i is the angle of incidence, NI and PR are defined as

$$NI = \frac{\alpha_2 \rho_2 - \alpha_1 \rho_1}{\alpha_2 \rho_2 + \alpha_1 \rho_1} \quad \text{and} \quad PR = \frac{\sigma_2 - \sigma_1}{(1 - \sigma_{avg})^2}$$

α , ρ , and σ denote P-wave velocity, density, and Poisson's ratio, respectively.

The NI term can be referred to as the intercept term, while the PR term is the Poisson's Reflectivity. I used this relationship to extract these terms from the well logs in order to estimate the AVO response for the top of coal so that I can know what to look for on the seismic data. Figure 3.9 shows the intercept and gradient attribute computed from the well log. The top of coal indicated by the red horizontal lines in (figure 3.9) is seen to have positive gradient and negative

intercept. This kind of AVO response is described as a class IV AVO response for a gas sand reservoir (Castagna et al., 1998).

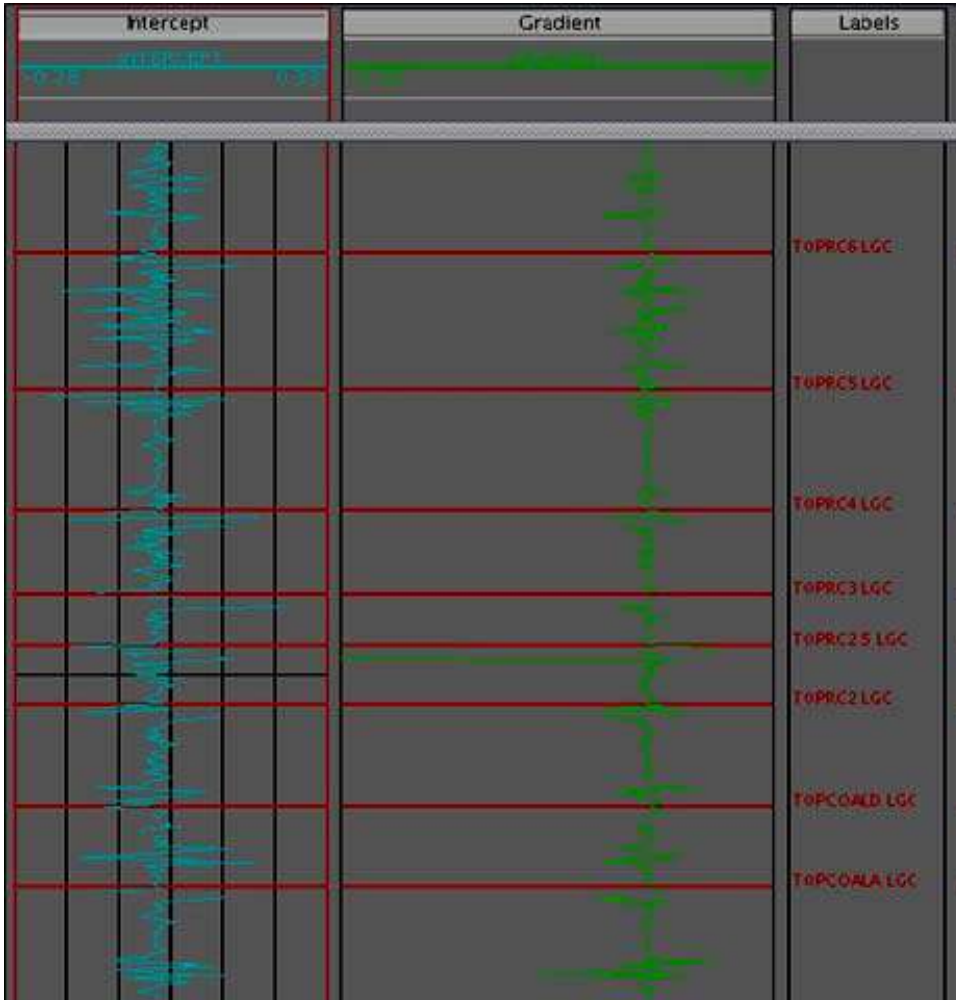


Figure 3.9 Intercept and gradient log computed from well log

3.9 Synthetic Models

Different models were generated in order to have a clear idea of the AVO response. The first modeling involves analytically solving the P-wave reflection

coefficient derived for an HTI medium by Rueger (1997). These equations were derived from the P-P reflection coefficient equations given by Aki-Richards (1980) with the assumption of small discontinuities in elastic parameters, i.e. low impedance contrast between the interfaces. Rueger assumed that the symmetry plane of the HTI model is parallel to the x1-axis, thus the symmetry plane is the x1-x3-plane.

The equation is given by:

$$R_p^{HTI}(i, \phi) = \frac{1}{2} \frac{\Delta Z}{\bar{Z}} + \frac{1}{2} \left\{ \frac{\Delta \alpha}{\bar{\alpha}} - \left(\frac{2\bar{\beta}}{\bar{\alpha}} \right)^2 \frac{\Delta G}{\bar{G}} + \left[\Delta \delta^{(v)} + 2 \left(\frac{2\bar{\beta}}{\bar{\alpha}} \right)^2 + \Delta \gamma \right] \cos^2 \phi \right\} \sin^2 i + \frac{1}{2} \left\{ \frac{\Delta \alpha}{\bar{\alpha}} + \Delta \varepsilon^{(v)} \cos^4 \phi + \Delta \delta^{(v)} \sin^2 \phi \cos^2 \phi \right\} \sin^2 i \tan^2 i \quad (3.27)$$

where i is the angle of incidence, Z is the P-impedance, α is the vertical P-wave velocity, β is the shear-wave velocity, G is the shear impedance and ($\varepsilon^v, \delta^v, \text{ and } \gamma^v$) are Thomsen's anisotropic parameters measured from the vertical. The other variables in equations 3.27 & 3.28 are defined below:

$$\bar{Z} = \left(\frac{Z_1 + Z_2}{2} \right), \quad \bar{\alpha} = \left(\frac{\alpha_1 + \alpha_2}{2} \right), \quad \bar{\beta} = \left(\frac{\beta_1 + \beta_2}{2} \right), \quad \bar{G} = \left(\frac{G_1 + G_2}{2} \right)$$

$$\Delta \varepsilon = \varepsilon_2 - \varepsilon_1 \quad \Delta \rho = \rho_2 - \rho_1 \quad \Delta \alpha = \alpha_2 - \alpha_1 \quad \Delta \beta = \beta_2 - \beta_1$$

$$\Delta G = G_2 - G_1 \quad \Delta Z = Z_2 - Z_1 \quad \Delta \gamma = \gamma_2 - \gamma_1 \quad \Delta \delta = \delta_2 - \delta_1$$

$$G = \rho \beta^2 \quad Z = \rho \alpha$$

Waves confined to the plane orthogonal to the symmetry plane, i.e. the isotropy plane, exhibit no velocity variations with propagation angle. Thus at azimuth (ϕ) 90 degrees from the symmetry axis, the equation 3.27 above reduces to:

$$R_p^{HTI}(i, \phi) = \frac{1}{2} \frac{\Delta z}{\bar{z}} + \frac{1}{2} \left\{ \frac{\Delta \alpha}{\bar{\alpha}} - \left(\frac{2\bar{\beta}}{\bar{\alpha}} \right)^2 \frac{\Delta G}{\bar{G}} \right\} \sin^2 i + \frac{1}{2} \left\{ \frac{\Delta \alpha}{\bar{\alpha}} \right\} \sin^2 i \tan^2 i \quad (3.28)$$

This is because $\text{Cos } 90^\circ = 0$

I computed the reflection coefficients of the waves both at azimuth $\phi = 0^\circ$ and at $\phi = 90^\circ$ (i.e. the isotropy plane). I varied the incidence angle for each of the azimuths from 0-40°. For the computation, I assumed an isotropic overburden over an HTI coal layer. The elastic parameters for the modeling (table 3.1) were taken from well logs, Xiaoxia's PhD thesis and Gerardo Franco's MS thesis.

Table 3.1 Elastic parameter for modeling

Layer	Lithology	Type	V_p (m/s)	V_s (m/s)	Density (g/cm ³)	Anisotropic parameters (γ, δ, ϵ)
1	shale	Isotropic	3300	1700	2.75	0,0,0
2	coal	HTI	2262	1057	1.40	0.1,0.19,- 0.02

These anisotropic parameters that were used for modeling are approximate numbers. They are approximations from Xiaoxia's PhD thesis and Gerardo Franco's MS thesis. In Rulison, we cannot estimate the precise values of the Thomsen's parameters because we do not have enough information from the vertical seismic profiling (VSP). The 2003 VSP data that Franco analyzed only covered the overburden (4600- 5050 ft). The 2006 VSP data covered the reservoir interval and the coal interval but, unfortunately, the data lacked adequate vertical P-wave vibrator coverage (Praj, 2008 through personal communication).

While the modeling is in terms of the reflection angle as an independent variable, it is appropriate to convert that reflection angle to the acquisition offset distance; thus, I estimated the source-receiver offset distance using the equation given by Walden (1991)

$$\sin^2 \theta = \frac{x^2 V_p^2}{V_{rms}^2 [V_{rms}^2 t(0) + x^2]} \quad (3.29)$$

where θ is the angles of incidence, x is the source-receiver offset, V_{rms} is the root-mean-square (rms) velocity, V_p is the interval velocity of the medium above the interface and $t(0)$ is the time at zero offset. I used $t=1.2s$, $V_{rms}=11532$ ft/s (3514 m/s), $V_p=10425$ ft/s (3177.54m/s). These numbers were estimated from the well log. Table 3.2 shows the values of the different reflection coefficients computed parallel to the symmetry plane and orthogonal to the symmetry plane (equations 3.27 & 3.28).

Table 3.2 Analytical solution of the reflection coefficients

Incidence Angle(°)	Offset (ft)	RC ($\phi=0^\circ$)	RC ($\phi=90^\circ$)	Percentage difference
0	0	-0.4902	-0.4902	0
10	2700	-0.46	-0.47	2
20	6000	-0.42	-0.45	7
30	9000	-0.37	-0.42	12
40	14000	-0.31	-0.41	24

From table 3.2 we can see that the reflection coefficients have identical magnitudes at the zero-offset as they should be, because it is difficult to define a unique azimuth for incidence angle = 0. Also, because at 0 degrees incidence angle, the other terms in the equations 3.27 and 3.28 I showed earlier will cancel out because of the combined presence of sine and cosine terms in the equation. This will reduce the equations to only the first term i.e. the impedance term. We can also see that the magnitudes of the reflection coefficient at azimuth equal to 90 degrees are larger for incidence angle greater than zero. This is because at azimuth equal to 90 degrees, the reflection coefficient equation for the symmetry plane of an HTI medium reduces to the reflection coefficient in the isotropy plane of an HTI. Thus, there won't be any influence of seismic anisotropy in this plane

and the waves will travel faster in this plane. Another striking observation is that the magnitudes of the reflection coefficients for the two orthogonal planes are similar until beyond 20 degrees. Beyond 20 degrees incidence angle, we observe the difference in the reflection coefficients for the two orthogonal planes. This implies that in real data we must have a large source-receiver offset coverage in order to be able to see the azimuthal variations in seismic amplitudes. The uniform azimuthal coverage of the prestack P-wave data only extended to offsets of about 6000 feet while modeling shows a 7% azimuthal dependence of the reflection coefficients at 6000 feet. Also, there that there are two factors that will reduce this observable maximum azimuthal dependence. Firstly, I have binned the seismic data over a wide azimuth range, not just the two extremes in azimuth. Second, I will be looking at the full-offset stack whose average offset distance is not the same as the maximum far-offset distance. The combination of these two effects probably reduces the anticipated azimuthal difference in amplitude by a factor of two smaller than indicated. Thus at 6000ft, I might not be able to see more than a 3% azimuthal variation in amplitudes.

In order to better quantify the differences in the reflection coefficients for the two orthogonal planes, I solved for the difference in the reflection coefficient for the two orthogonal planes. The difference in the reflection coefficient (RC_{diff}) for the two orthogonal symmetry planes derived is:

$$RC_{diff} = \frac{\sin^2 i}{2} \left[\Delta\delta^v + \left(\frac{2\bar{\beta}}{\bar{\alpha}} \right)^2 * 2\Delta\gamma^v + \{ \tan^2 i * \Delta\varepsilon^v \} \right]$$

The meaning of the equation is that the difference in the reflection coefficient for the two orthogonal planes is a function of the ratio of the average of S-wave velocities across the interface to average of the P-wave velocities across the interface, as well as the differences in the anisotropic parameters across the interface. I also computed the percentage differences of the reflection coefficients; even at 30 degrees, the percentage difference is only about 12%. In order to have a better quantitative idea of the amount of the contrast in anisotropic parameters required to cause the azimuthal-variation in reflection coefficients: I explored the influence of each of the Thomsen's parameters. I created a series of models, differing by each other in the Thomsen parameter that is allowed to be nonzero. For the first computation, I set $\gamma=0.0$, $\delta=0.0$, $\epsilon=0.2$ and I used the same elastic parameters in table 3.1. Table 3.3 shows the result for this model.

Table 3.3 Reflection coefficients solution when $\gamma=0.0$, $\delta=0.0$, $\epsilon=0.2$

Incidence Angle(°)	Offset (ft)	RC ($\phi=0^\circ$)	RC ($\phi=90^\circ$)	Percentage difference
0	0	-0.49	-0.49	0
10	2700	-0.479	-0.48	0
20	6000	-0.43	-0.435	1
30	9000	-0.36	-0.375	4

40	14000	-0.285	-0.31	8
----	-------	--------	-------	---

For the second calculation, I set $\gamma=0.0$, $\delta=0.2$, $\epsilon=0.0$. Table 3.4 shows the result obtained from these calculations.

Table 3.4 Reflection coefficients solution when $\gamma=0.0$, $\delta=0.2$, $\epsilon=0.0$

Incidence Angle($^{\circ}$)	Offset (ft)	RC ($\phi=0^{\circ}$)	RC ($\phi=90^{\circ}$)	Percentage difference
0	0	-0.49	-0.49	0
10	2700	-0.47	-0.48	2
20	5700	-0.428	-0.435	3
30	9000	-0.34	-0.375	9
40	14000	-0.27	-0.31	13

For the 3rd calculation, I set $\gamma=0.1$, $\delta=0.0$, $\epsilon=0.0$. Table 3.5 shows the result obtained from these calculations.

Table 3.5 Reflection coefficients solution when $\gamma=0.1$, $\delta=0$, $\varepsilon=0$

Incidence Angle($^{\circ}$)	Offset (ft)	RC ($\phi=0^{\circ}$)	RC ($\phi=90^{\circ}$)	Percentage difference
0	0	-0.49	-0.49	0
10	2700	-0.475	-0.48	1
20	5700	-0.42	-0.43	2
30	9000	-0.345	-0.37	7
40	14000	-0.27	-0.31	13

From the analytical calculations, we can see that for the AVO to be azimuthally-variant, a contrast in Thomsen's anisotropic parameters must exist. Since these calculations were done with the Andreas Rueger equations with the assumption of small material contrast across the interface, I find it necessary to test the validity of my computations under this assumption. I recomputed the exact reflection

coefficients at azimuth=0° and 90 ° using the Colorado School of Mines Center for Wave Phenomenon’s code RefRealAziHTI. Unlike my previously-employed method, this algorithm does not assume small change across the interface in acoustic parameters. I used the same parameters as in table 3.1 for this more exact computation. Table 3.6 shows the result.

Table 3.6 Reflection coefficients solution computed with the exact equation

Incidence Angle(°)	offset	RC ($\phi=0^\circ$)	RC ($\phi=90^\circ$)	Percentage difference
0	0	-0.49	-0.49	0
10	2700	-0.472	-0.475	0.6
20	5700	-0.42	-0.434	3
30	9000	-0.343	-0.37	8
40	14000	-0.26	-0.30	15

While the percent differences in Table 3.6 are slightly smaller than in Table 3.2, the overall conclusions are unchanged. Table 3.6 still shows that it is the contrasts in Thomsen's parameters that are responsible for the azimuthal-variation in reflection coefficients; this effect is more pronounced after 20-degrees incidence angle, which is beyond a 6000 ft of offset distance. In Rulison, the full azimuthal coverage is achieved around 6000 ft of offset; thus this might be a challenge for the azimuthal AVO analysis.

As independent confirmation of my above modeling results, I moved into the second stage of my modeling, which is the computation of the P-wave reflection coefficients using a java applet that was developed at the Consortium for Research in Elastic Wave Exploration Seismology (CREWES), at the University of Calgary. The applet is AniZoeppritz Explorer and it can be used freely on the internet. The Explorer can calculate exact reflection coefficients for VTI media, and linearized coefficients for both VTI and HTI media. It can also calculate exact (Zoeppritz) and linearized (Aki-Richards) coefficients for corresponding isotropic media. I modeled the behavior of the P-wave reflection coefficient in the presence of anisotropy, both at 0 degrees and at 90 degrees. I used the same parameters in Table 3.1. Figure 3.10 shows the reflection coefficient as a function of incidence angle with the anisotropic parameters at 0 degrees, while Figure 3.11 shows the reflection coefficient as a function of incidence angle with the anisotropic parameters at 90 degrees azimuth.

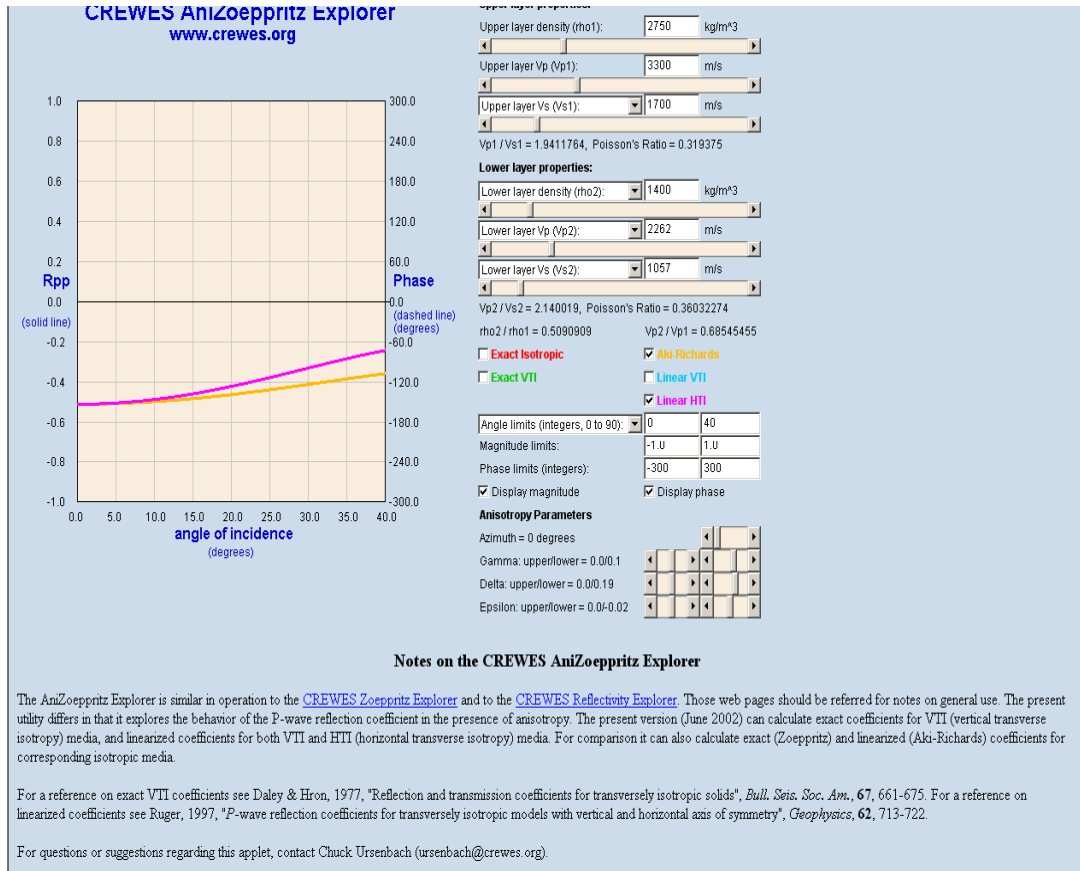


Figure 3.10 P-wave reflection coefficients as a function of angle of incidence for the top of Coal- Azimuth 0° computed using CREWES Anizoeppritz Explorer.

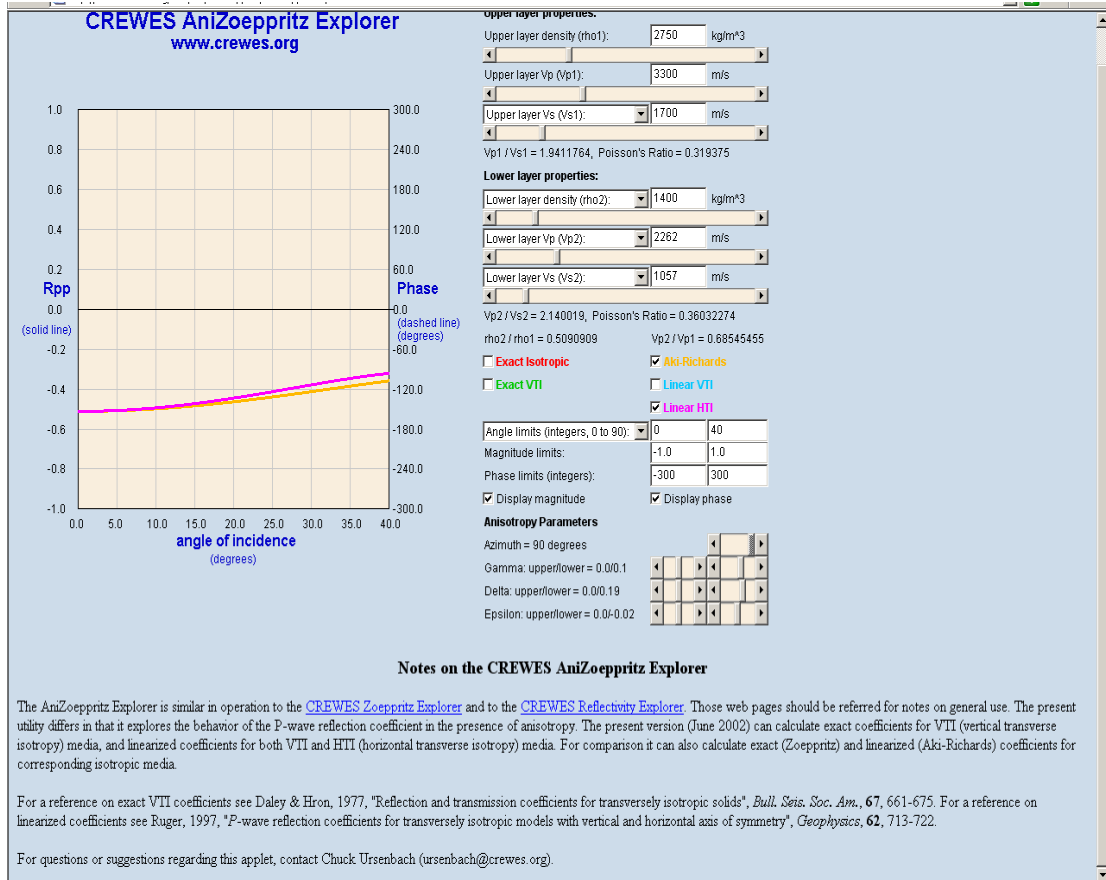


Figure 3.11 P-wave reflection coefficients as a function of angle of incidence for the top of Coal- Azimuth 90° computed using CREWES Anizoeppritz Explorer.

The yellow line in Figures 3.10 and 3.11 is the solution for the Aki-Richards's coefficient for the isotropic media while the pink line is the solution for the linearized coefficients for the HTI media. The solutions for the Aki-Richards's coefficient (yellow line) for the isotropic media for the two models, as shown in Figure 3.10 and 3.11, are identical as expected. There is a variation in the solution for the linearized coefficients for the HTI at 0 and 90-degrees azimuth. The variation is due to the contrast in the anisotropic parameters (γ , δ , and ϵ)

between the isotropic layer and the coal layer. This modeling also shows a small azimuthal dependence, especially around 20-degree incidence angles.

I will now present the last part of my modeling; that is the computation of various synthetic seismograms in order to have a clearer idea of the AVO response. A half-space model was specified for the computation of the synthetic seismograms using the reflectivity code, Anisynpa. The synthetic seismograms included direct arrivals, converted waves and multiples. I used a 25-Hertz Ricker wavelet for the computation because it is the dominant frequency around the coal interval in the P-wave data. The synthetic models were created using 55 receiver positions on the surface, spaced by 80 meters. The first receiver was at 0 meters and the last receiver was at 4400 meters (14400 ft). 14400 ft is almost twice the maximum far offset distance that existed in the real seismic data. Both the source and the receiver components were specified as vertical. Tables 3.6 to 3.8 show the different layer types, their velocities, densities, and other elastic parameters used in the model. The velocities and densities were estimated from well logs in Rulison field while anisotropic parameters were taken from Xiaoxia's (2006) PhD thesis and Gerardo Franco's (2007) MS thesis. For modeling, I assumed that the symmetry of the HTI model is parallel to the x_1 axis where x_3 is chosen to be vertical. The (x_1-x_3) plane is called the symmetry plane; the elastic constants for propagation in the symmetry plane are represented by V_{11} , V_{33} , V_{13} , V_{55} . Waves confined to the plane perpendicular (x_2-x_3) plane to the symmetry-axis plane are represented by the following elastic constants: V_{22} , V_{33} , V_{23} , V_{44} . The elastic parameters for the coal layer are: $V_{11}=2655$ m/s, $V_{22}=2262$ m/s, $V_{33}=2262$ m/s

$V_{44}=1057$ m/s $V_{55}=1358$ m/s $V_{66}=1358$ m/s, $V_{12}=1198$ m/s, $V_{13}=1198$ m/s, $V_{23}=1439$ m/s. These parameters are different from the parameters that I used for the first two part of the modeling. This is because the inputs to the code are the C_{ij} s and unfortunately we don't have these information for Rulison Field.

The first model is called Isotropic-isotropic-isotropic.

Table 3.7 Parameters for isotropic-Isotropic-Isotropic model.

Layer	Lithology	Thickness (Meters)	Type	V_p (m/s)	V_s (m/s)	Density (g/cm ³)
1	sand	100	Isotropic	1830	900	2.35
2	shale	1900	Isotropic	3400	2600	2.75
3	coal	∞	Isotropic	2262	1057	1.40

The second model is the Isotropic-VTI-Isotropic. The second layer (isotropic) in model 1 was replaced with a VTI layer.

Table 3.8 Parameters for isotropic-VTI-Isotropic model.

Layer	Lithology	Thickness (m)	Type	V_p (m/s)	V_s (m/s)	Density (g/cm ³)
1	sand	100	Isotropic	1830	900	2.35
2	shale	1900	VTI	3400	2600	2.75
3	coal	∞	Isotropic	2262	1057	1.40

The elastic parameters for the VTI are: $V_{11}=3075$ m/s $V_{33}=3400$ m/s $V_{44}=2600$ m/s
 $V_{66}=1862$ m/s $V_{13}=1476$ m/s.

For the third model, the third layer in the second model was replaced with an HTI symmetry. The third model created is called the ISO-VTI-HTI model.

Table 3.9 Parameters for isotropic-VTI-HTI model.

Layer	Lithology	Thickness (Meters)	Type	V_p (m/s)	V_s (m/s)	Density (g/cm ³)
1	sand	100	Isotropic	1830	900	2.35
2	shale	1900	VTI	3400	2600	2.75
3	coal	∞	HTI	2262	1057	1.40

The elastic parameters for the VTI are: $V_{11}=3075$ m/s $V_{33}=3400$ m/s $V_{44}=2600$ m/s
 $V_{66}=1862$ m/s $V_{13}=1476$ m/s. The parameters for the HTI are: $V_{11}=2655$ m/s,
 $V_{22}=2262$ m/s, $V_{33}=2262$ m/s $V_{44}=1057$ m/s $V_{55}=1357$ m/s $V_{66}=1357$ m/s,
 $V_{12}=1198$ m/s, $V_{13}=1198$ m/s, $V_{23}= 1439$ m/s.

Figure 3.12 to figure 3.14 show the synthetic gathers generated.

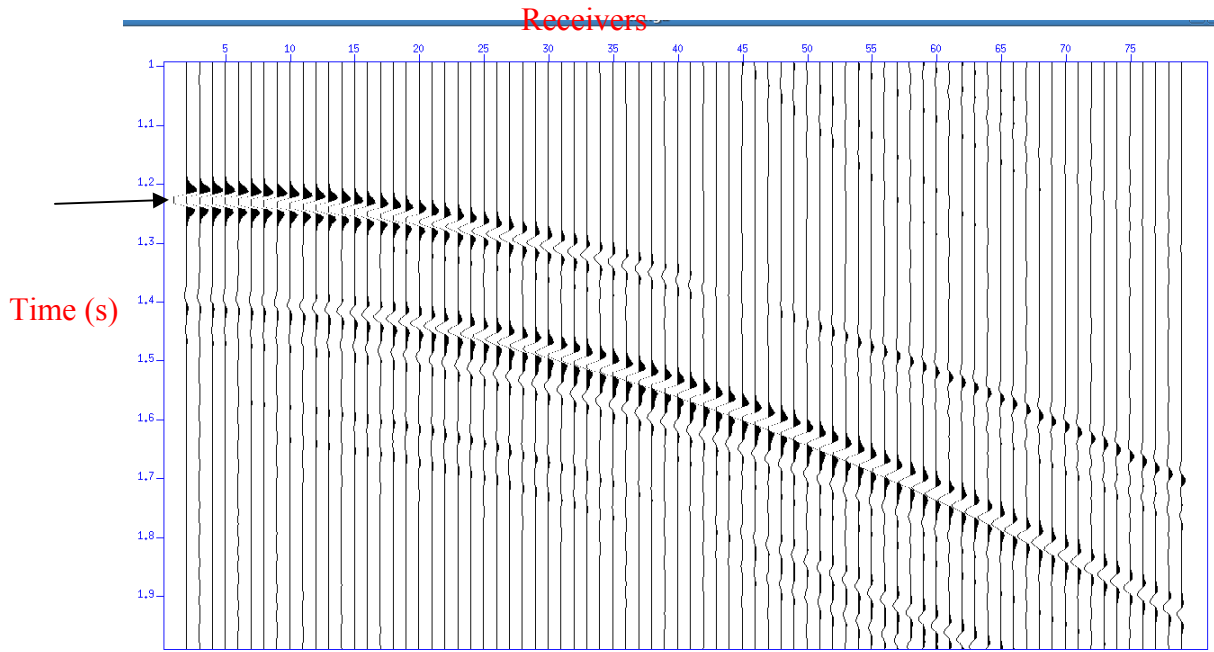


Figure 3.12 Synthetic gather for the ISO-ISO-ISO model (model 1). The traces were generated with the reflectivity code (Anisynpa). The reflection from the top of coal corresponds to troughs shown by the arrow i.e the event at 1.22 seconds

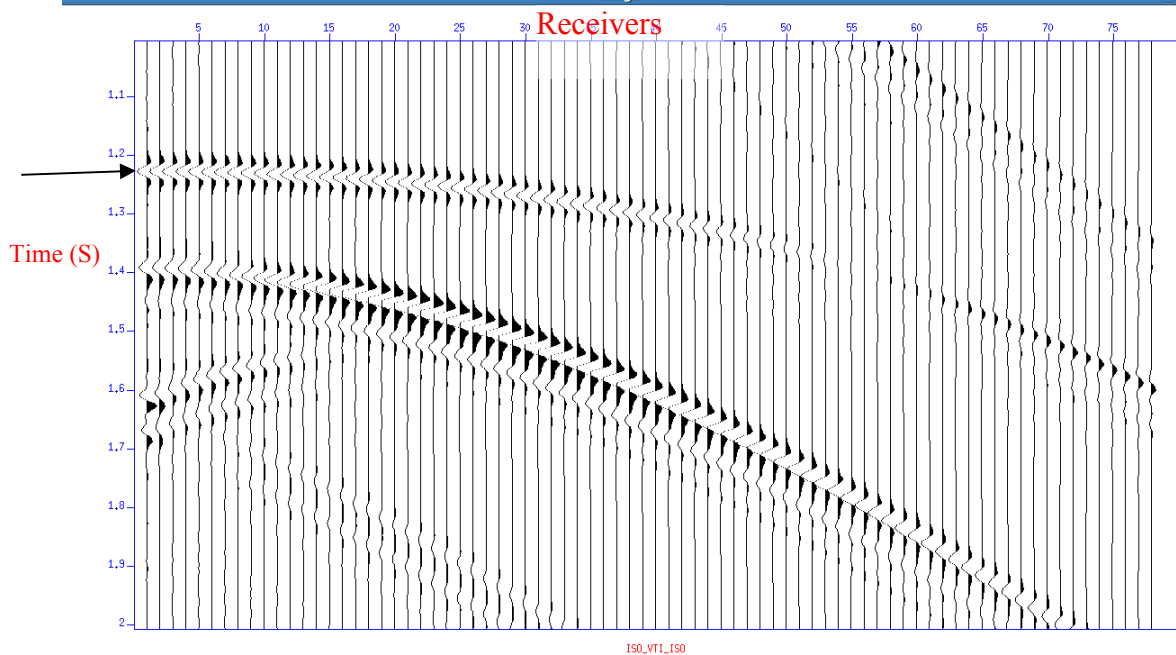


Figure 3.13 Synthetic gather for the ISO-VTI-ISO model (model 2), parallel to the fractures. The reflection from the top of coal corresponds to troughs shown by the arrow i.e the event at 1.22 seconds

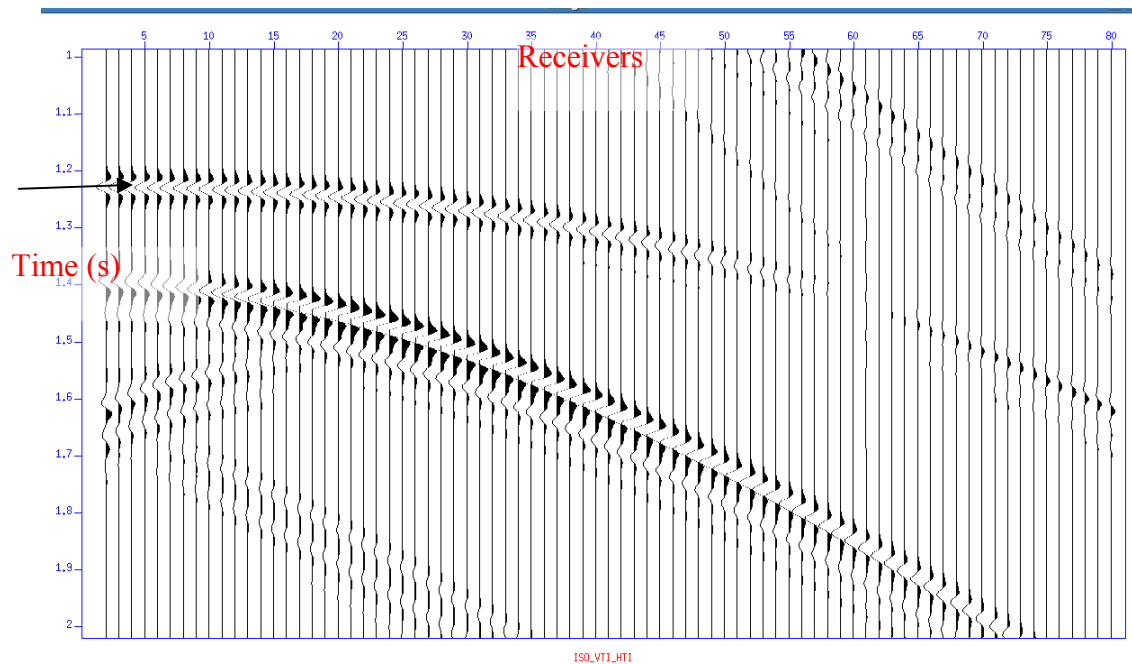


Figure 3.14 Synthetic gather for the ISO-VTI-HTI model (model3), perpendicular to the fracture. The reflection from the top of coal is shown by the arrow.i.e the reflection at 1.226s.

3.10 Observations from the synthetic models

The synthetic models show that the reflection from the top of coal corresponds to troughs and the amplitude decreases as a function of offset. This is typical of a class IV AVO anomaly. Model 1, Figure 3.12 is an Isotropic-Isotropic-Isotropic model. The negative reflection from the top of coal becomes increasingly positive and there is a change in polarity in the far offset (around the 45th receiver or 12000 ft). Figure 3.13 is Isotropic -VTI- Isotropic model; the second isotropic layer in model 1 was replaced with a VTI layer. The magnitude of the amplitudes for model 2 is similar to model 1. This difference is really subtle and the phase reversal is also noticeable on the synthetic seismogram from model 2, (Figure 3.13) but here the phase reversal is seen around the 52nd receiver. This is due to

the fact that rays and wavefronts for isotropic media are completely different for a VTI medium. The wavefronts in isotropic media are spherical while the wavefronts in anisotropic media are not. Also the vertical P-wavefronts in a VTI medium are more advanced in the horizontal direction than in the vertical direction (Rueger, 1997). The third model is Isotropic-VTI-HTI model. The third Isotropic layer in model 2 was replaced with an HTI layer. The magnitudes of the amplitudes of model 3 are subtly smaller than that of model 2. Model 2 is parallel to the fractures while model 3 is orthogonal to the fractures. The subtle difference in the amplitude is due to the fact that the anisotropic parameters: (γ , δ , ϵ) across the interface between the coal and the VTI layer is negligible. It is also due to the large impedance contrast between the coal and the overburden.

3.11 Effect of tuning on thin coal layer

The relationship between layer thicknesses, the signal wavelength, and the resolution of the top and bottom of a thin layer have been studied by various authors, Widess (1973), Kallweit and Wood (1982), Knapp (1990) and Gochioco (1991). Tuning thickness can be defined as the thickness of the maximum observed amplitude. The average thickness of the coals in Rulison Field is 10m. In order to determine the tuning thickness of the coal layer, I ran some tests by varying the coal thickness from 0 to 100 meters. I used a 6-layer model for this test (ISO-VTI-HTI-ISO-HTI-ISO). The third and the fifth layer are the two coal layers. I varied the thickness of the coal in the third layer. I varied it from 0 to 100 meters and I kept the thickness of the other five layers constant.

Table 3.10 is the parameter used for the ISO-VTI-HTI-ISO-HTI-ISO.

Layer	Lithology	Thickness (Meters)	Type	V_p (m/s)	V_s (m/s)	Density (g/cm^3)
1	sand	300	Isotropic	2900	2600	2.30
2	shale	1500	VTI	3300	1700	2.75
3	coal	0-100	HTI	2262	1057	1.4
4	sand	10	Isotropic	2900	2600	2.4
5	coal	1000	HTI	2262	1057	1.4
6	shale	∞	ISO	2900	2600	1.7

Figure 3.15 to figure 3.22 shows the synthetics

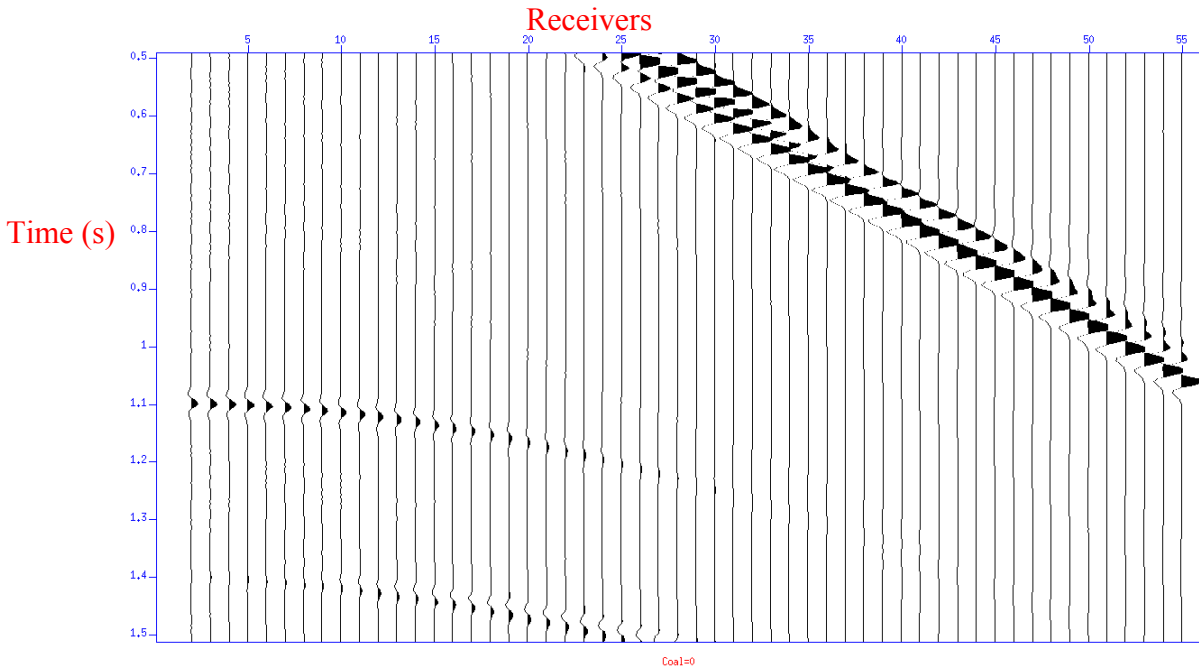


Figure 3.15 Synthetic gather for the ISO-VTI-HTI-ISO-HTI-ISO model, with thickness of the 2nd and 3rd layer equal 0

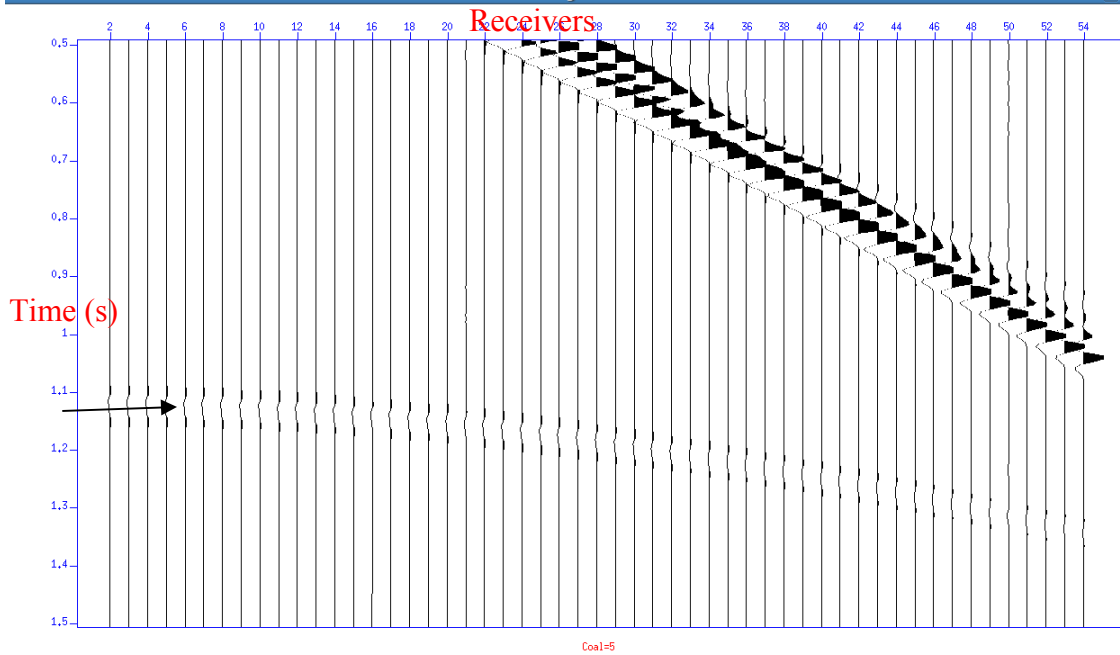


Figure 3.16 Synthetic gather for the ISO-VTI-HTI-ISO-HTI-ISO model, with coal thickness for the 3rd layer=5 meters. The top of coal of the 5m coal layer is the troughs shown by the arrow

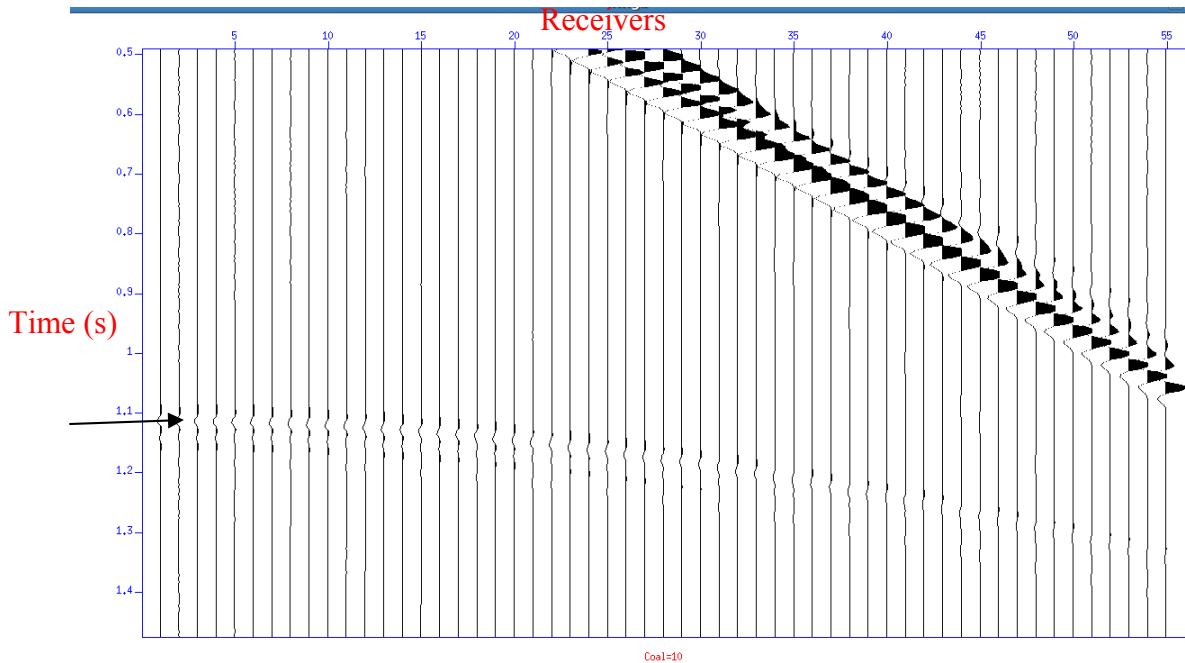


Figure 3.17 Synthetic gather for the ISO-VTI-HTI-ISO-HTI-ISO model, with coal thickness for the 3rd layer=10 meters, the top of coal of the 10m coal layer is the troughs shown by the arrow

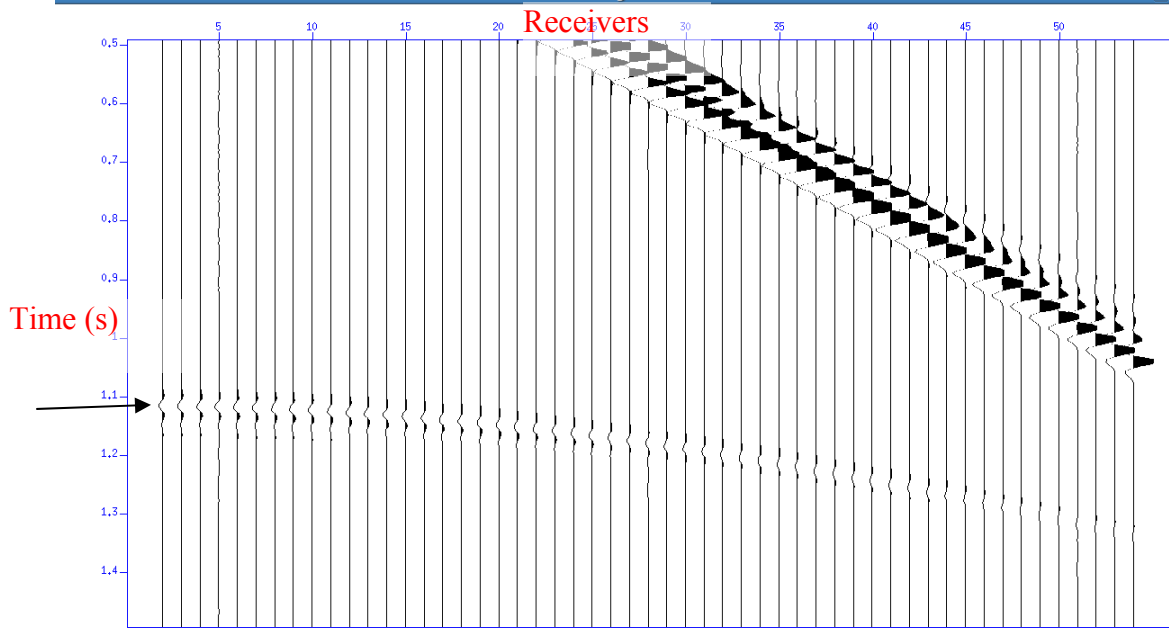


Figure 3.18 Synthetic gather for the ISO-VTI-HTI-ISO-HTI-ISO model, with coal thickness for the 3rd layer=15 meters, the top of coal of the 15m coal layer is the troughs shown by the arrow

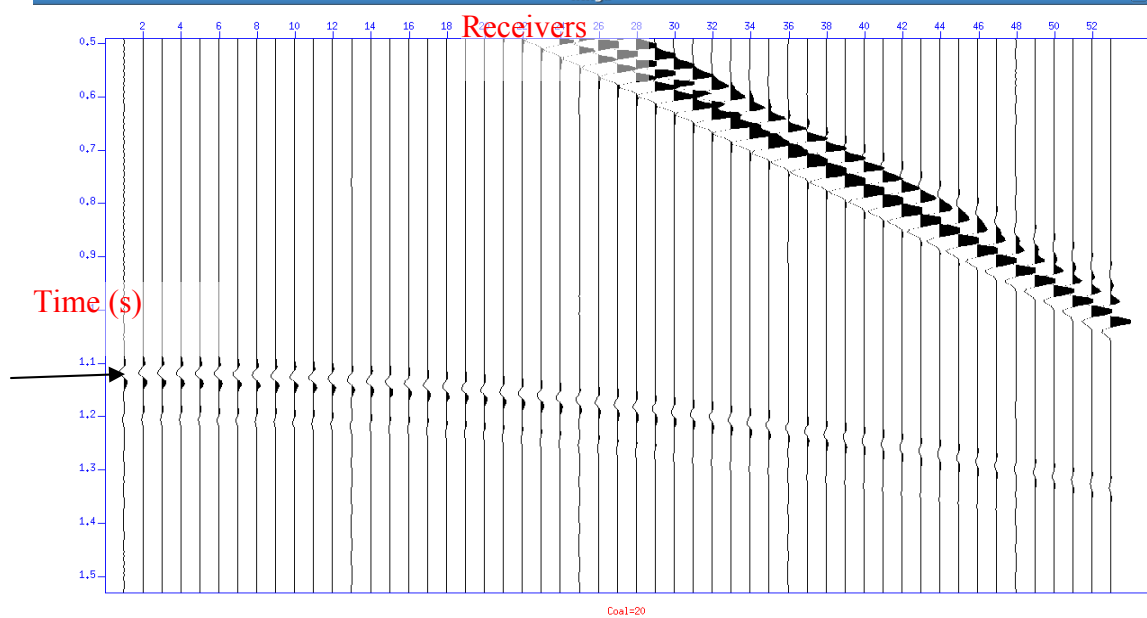


Figure 3.19 Synthetic gather for the ISO-VTI-HTI-ISO-HTI-ISO model, with coal thickness for the 3rd layer=20 meters, the top of coal of the 20m coal layer is the troughs shown by the arrow

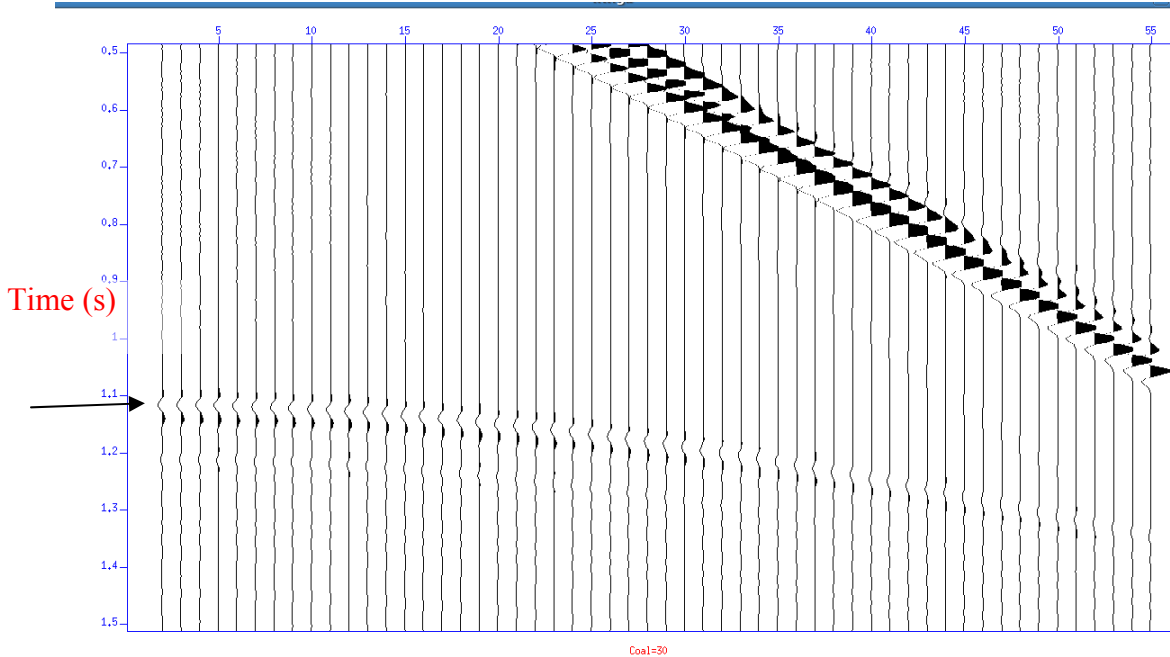


Figure 3.20 Synthetic gather for the ISO-VTI-HTI-ISO-HTI-ISO model, with coal thickness for the 3rd layer=30 meters, the top of coal of the 30m coal layer is the troughs shown by the arrow

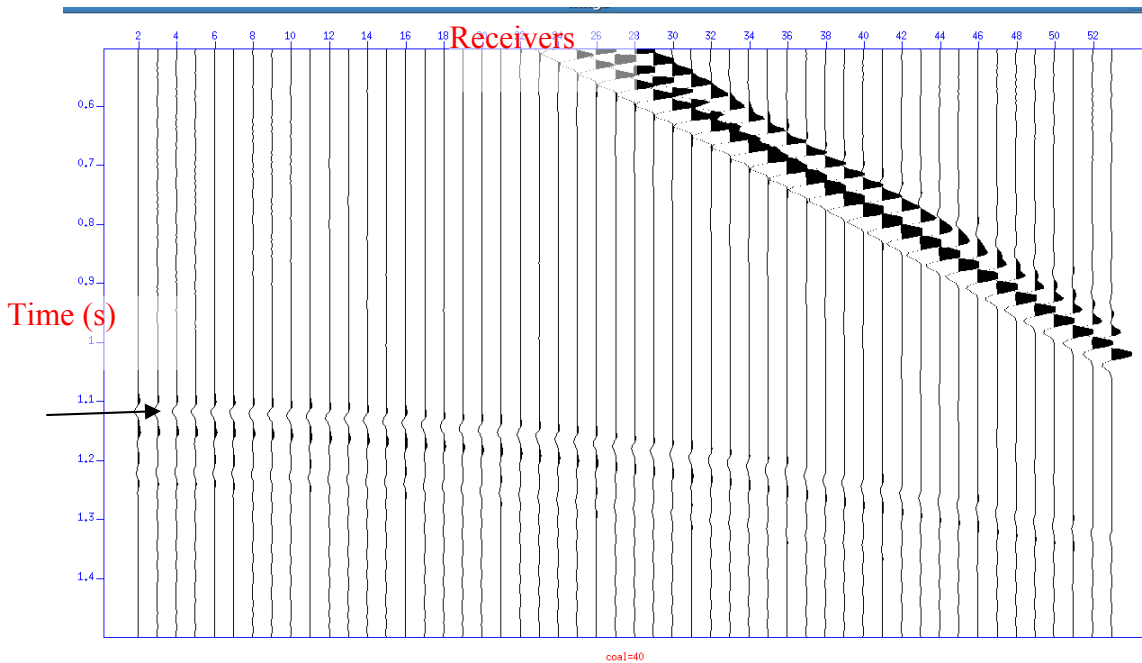


Figure 3.21 Synthetic gather for the ISO-VTI-HTI-ISO-HTI-ISO model, with coal thickness for the 3rd layer=40 meters, the top of coal of the 40m coal layer is the troughs shown by the arrow

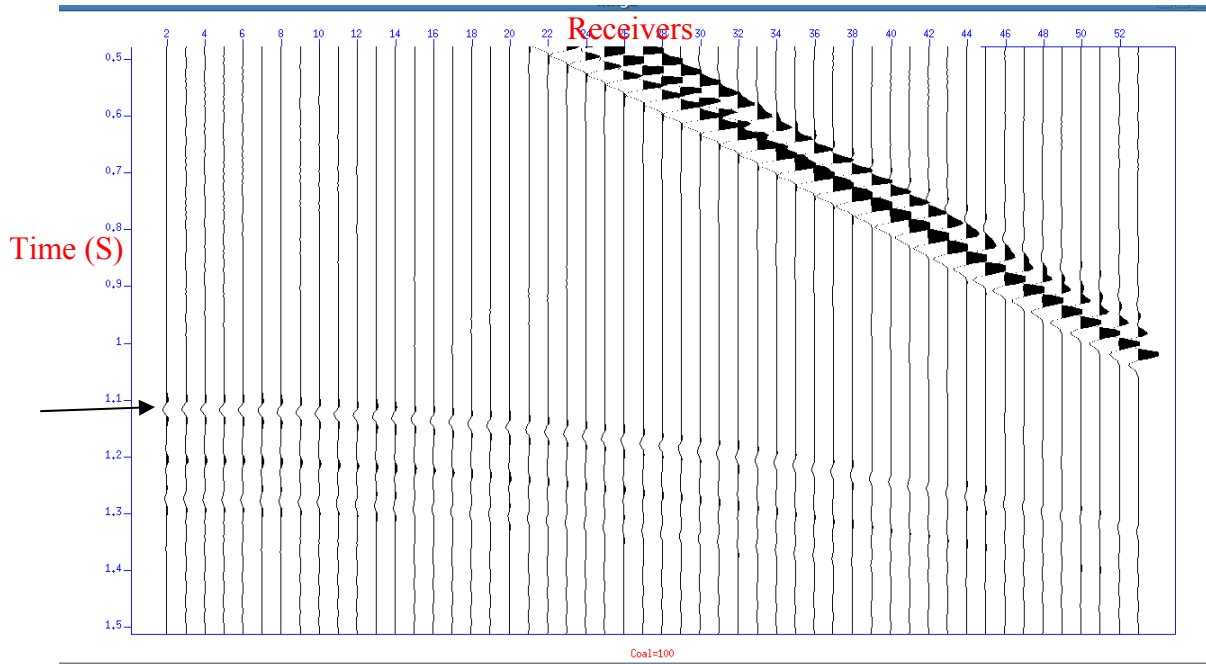


Figure 3.22 Synthetic gather for the ISO-VTI-HTI-ISO-HTI-ISO model, with coal thickness for the 3rd layer=100 meters, the top of coal of the 100m coal layer is the troughs shown by the arrow

Figures 3.16 – 3.22 show that at 5 meters, the top of the coal can be seen but as the thickness of the coal is increased through the sequence 5-10-15-20-30-40-100 meters the peak amplitude increases with respect to the increment in the thickness of the coal. The maximum amplitude is observed at about 20 meters thickness. In order to corroborate the modeling result, I computed the tuning thickness using the equation that was given by Widess (1973):

$$\text{tuning thickness} = \text{wavelength} / 4$$

the velocity of the coal is 2262 m/s while the frequency is 25 Hertz,

thus, the wavelength is velocity/frequency = 2262/25 meters
 =90.48 meters

Therefore, the tuning thickness is $90.48/4 \approx 20$ meters. This means that coal layers with thickness less than 20 meters will have their amplitudes diminished in proportion to their thickness.

3.12 Rulison Field Isotropic Synthetic Seismogram

I generated a 1-D isotropic synthetic seismogram using the well log information from well 441-20 in order to compare it with the real data. Figure 3.26 shows the zero-offset synthetic computed with Landmarks' SynTool software. The top of Cameo is indicated by the white horizontal line.

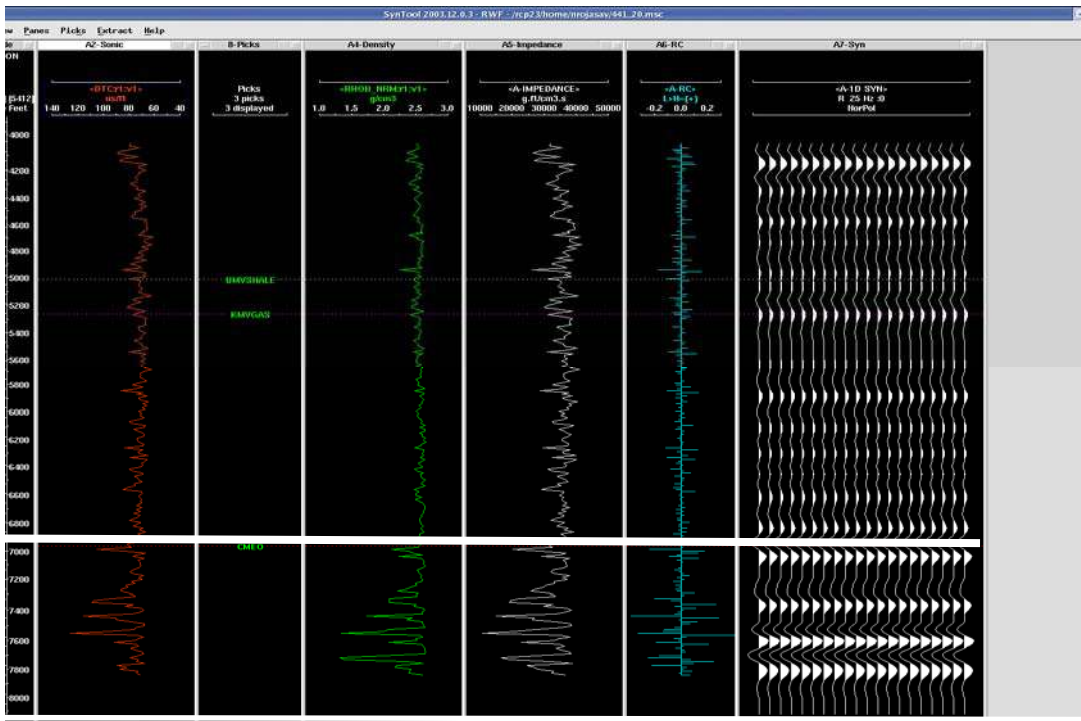


Figure 3.23 zero-offset synthetic computed with Landmarks' SynTool software.

The top of Cameo is shown with the white horizontal line. The 1st column in the plot is the sonic log, the 2nd column contains the picks label, the density log is in the 3rd column, the impedance, reflection coefficient curve and the synthetic seismograms are in column 4, 5, and 6 respectively. The different coal layers have low density and low velocity. The synthetic on the far right of figure 3.23 confirms that each of the individual coal layers cannot be resolved seismically.

3.13 Summary

Modeling has shown that the AVO response will be azimuthally dependent when there is a contrast in Thomsen's anisotropic parameters between the overburden and top of coal. I have modeled the azimuthal AVO dependence given the best-guess values for the Thomsen parameters. From that, I have an estimate of the percentage variation for the isolated, thick coal. It was small. It will be even smaller because I will be looking at a range of azimuths and not just that far-offset distance. I have also demonstrated that the coals are below tuning and they are not individually distinguishable.

CHAPTER 4

AMPLITUDE ANALYSIS

4.0 Introduction

In this chapter, I will discuss the AVO analysis of the prestack P-wave data. In chapter 2, I discussed the processing of this data and I mentioned that the predominant stress orientation for this study area is N70°W. The data were divided into two volumes according to azimuth: the first was parallel to this stress orientation while the second was orthogonal to the stress orientation. The division was done based on the premise that open fractures are aligned parallel to maximum horizontal stress. AVO analysis was carried out on each of the two azimuth-selected seismic volumes.

4.1 Prestack data Analysis

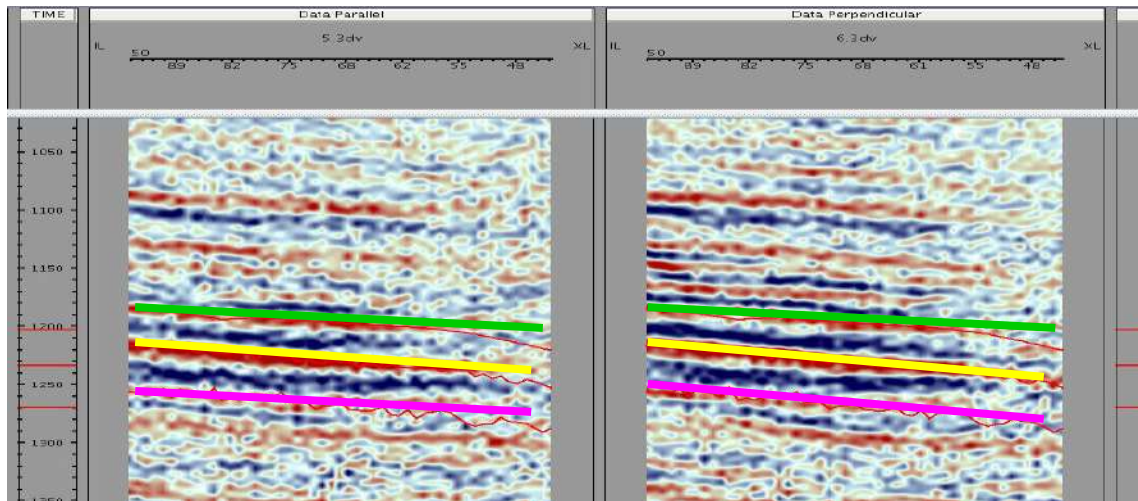


Figure 4.1 shows the full-stack volume for each of the two azimuth separated volumes.

Three different horizons were picked within the coal interval (i.e. the intervals between the Cameo coal and Rollins Formation) on the two azimuth-separated datasets. Figure 4.1 shows the full stack volume for each of the two azimuth-separated volumes. The first horizon is denoted by the green color, the second horizon is shown by the yellow color, and the third horizon is shown by the pink horizontal line. RMS amplitude maps were extracted for each of the three horizons on the two full-stack (all offsets) volumes. The horizon is centered over a 20-ms window. RMS amplitudes were preferred because they provided a measurement of the reflected energy over a given window (Aki and Richards, 1980). Figure 4.2 and figure 4.3 are the RMS amplitude maps for horizon 1 for the data parallel and data orthogonal to the fracture direction respectively.

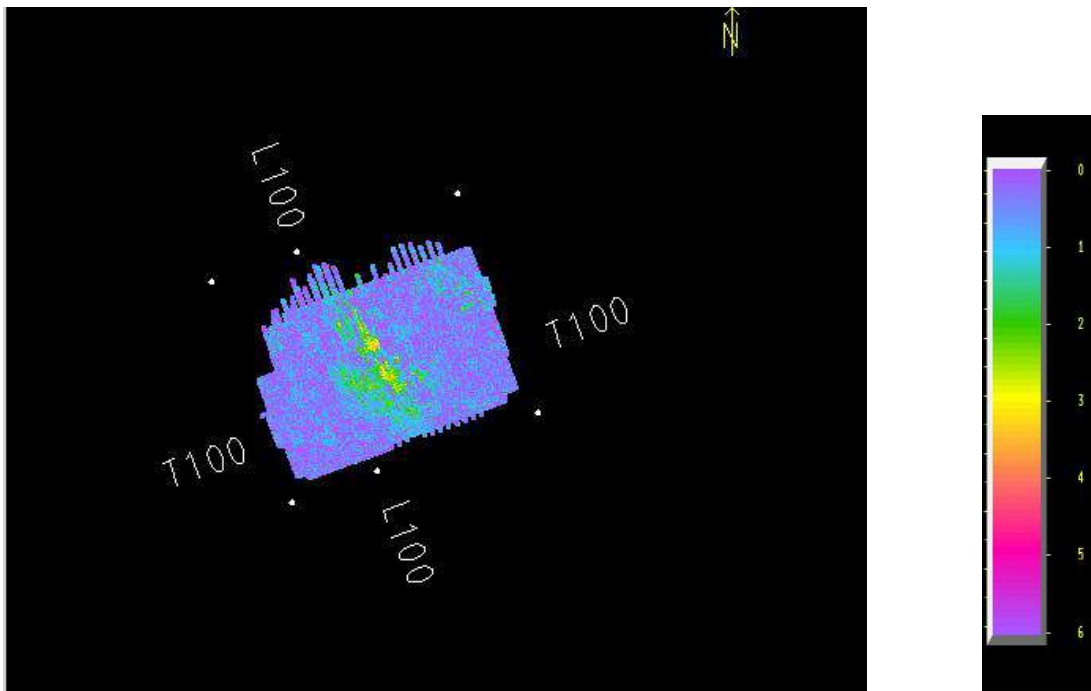


Figure 4.2 RMS amplitude map for horizon 1, green horizon, for data (full-stack) parallel to the fracture direction computed over the entire survey

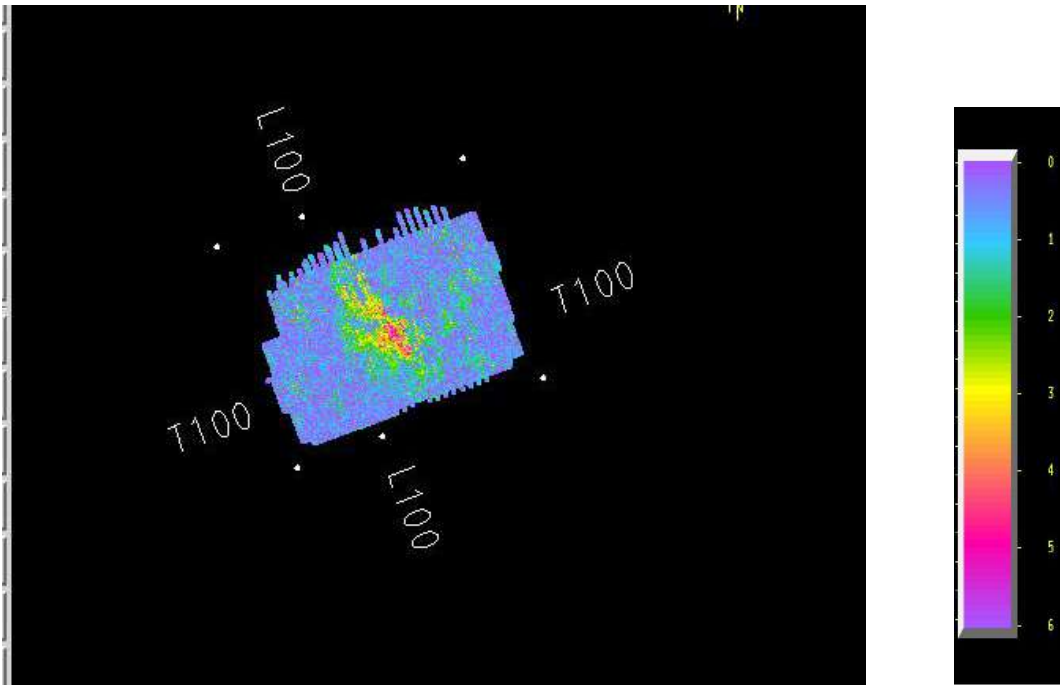


Figure 4.3 RMS amplitude map for horizon 1, green horizon, for data (full-stack) orthogonal to the fracture direction computed over the entire survey

Figure 4.4 and Figure 4.5 are the RMS amplitude maps for horizon 2 for the data parallel and data perpendicular to the fracture direction respectively.

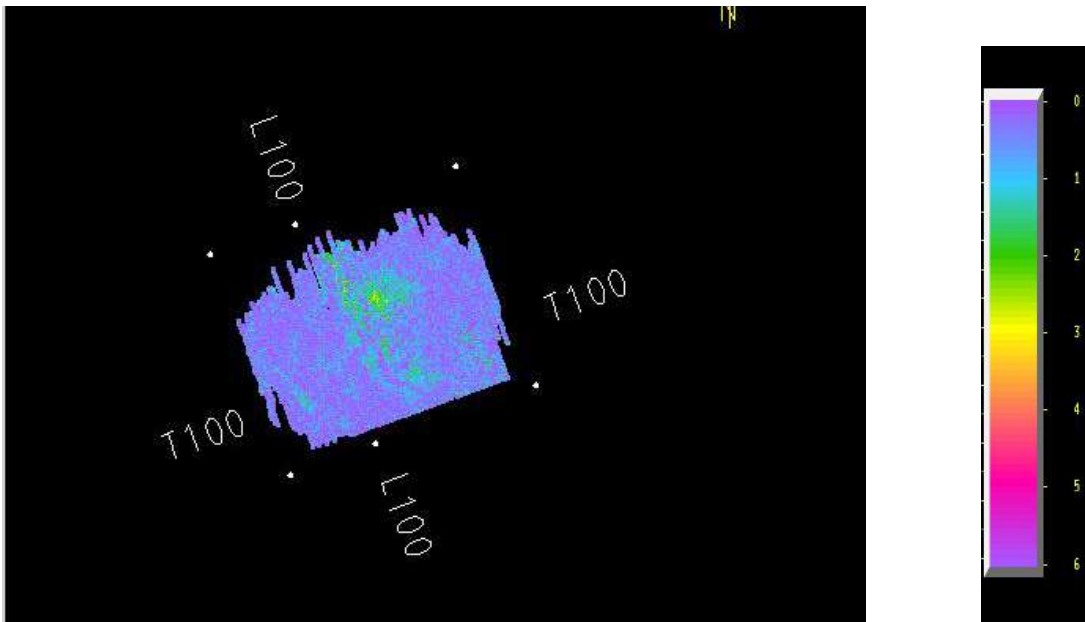


Figure 4.4 RMS amplitude map for horizon 2, yellow horizon, for data (full-stack) parallel to the fracture direction computed over the entire survey

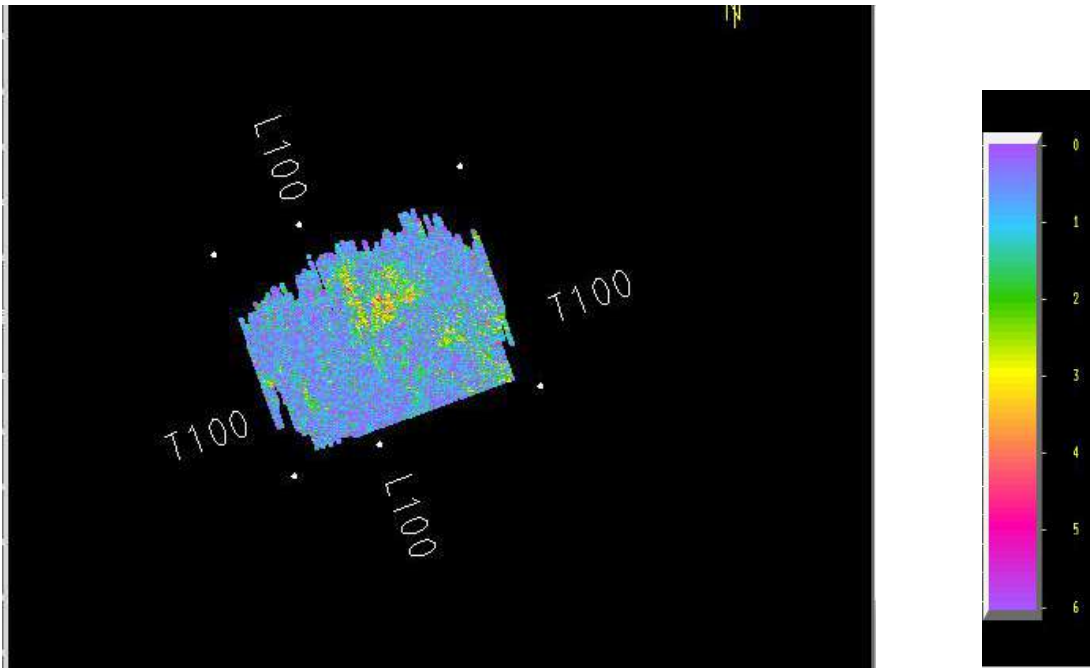


Figure 4.5 RMS amplitude map for horizon 2, yellow horizon, for data (full-stack) orthogonal to the fracture direction computed over the entire survey

Figure 4.6 and figure 4.7 are RMS amplitude maps for horizon 3 for the data parallel and data perpendicular to the fracture direction respectively.

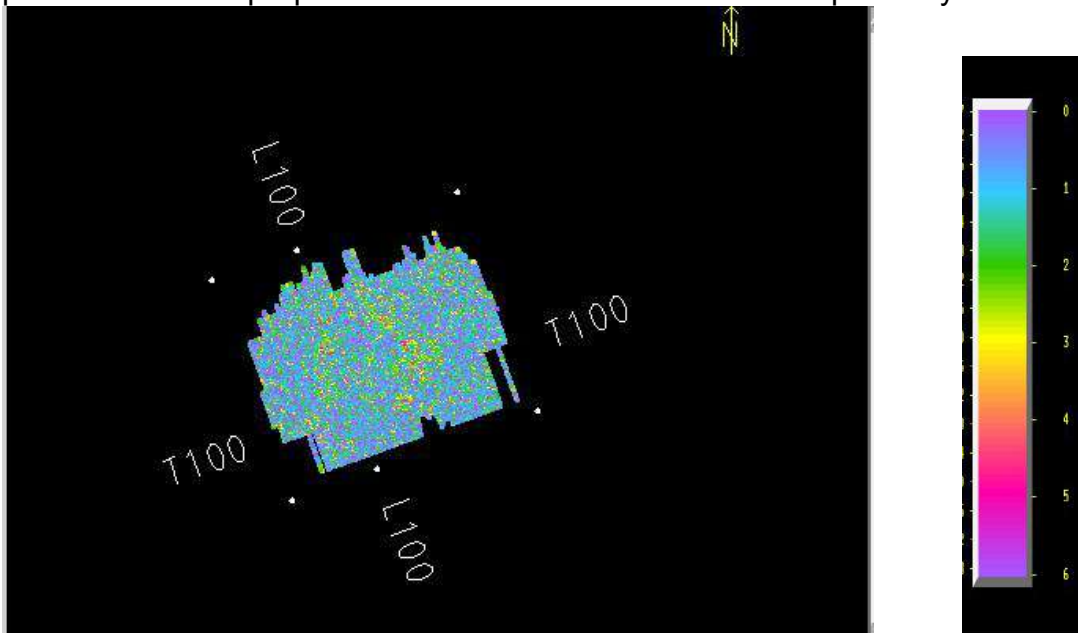


Figure 4.6 RMS amplitude map for horizon 3, pink horizon, for data (full-stack) Parallel to the fracture direction computed over the entire survey

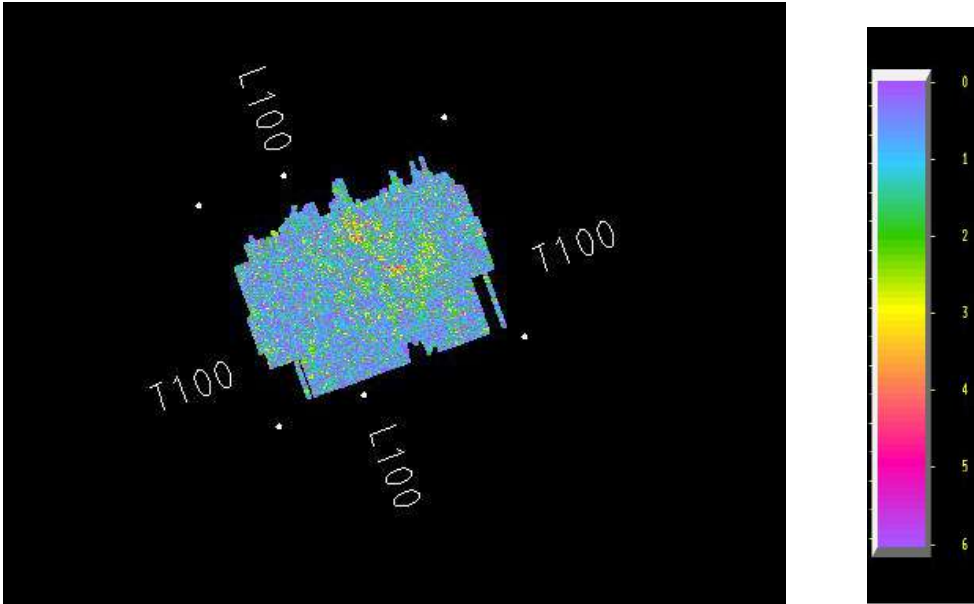


Figure 4.7 RMS amplitude map for horizon 3, pink horizon, for data (full-stack) orthogonal to the fracture direction computed over the entire survey

I also extracted RMS amplitudes for the whole interval between Horizon 1 and Horizon 3 (Figures 4.8 & 4.9).

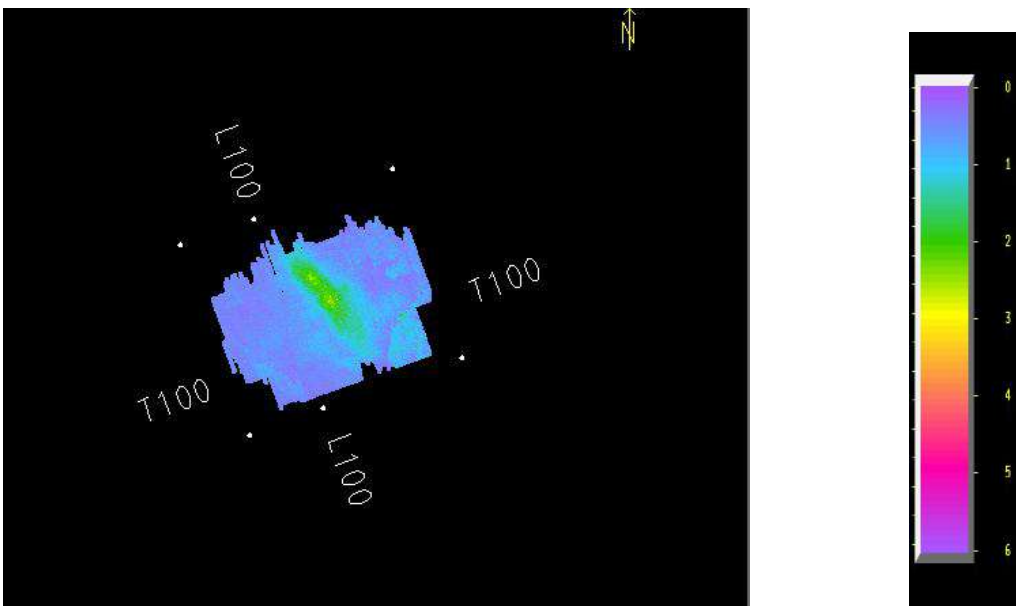


Figure 4.8 RMS amplitude map for the data (for the entire interval) parallel to the fractures

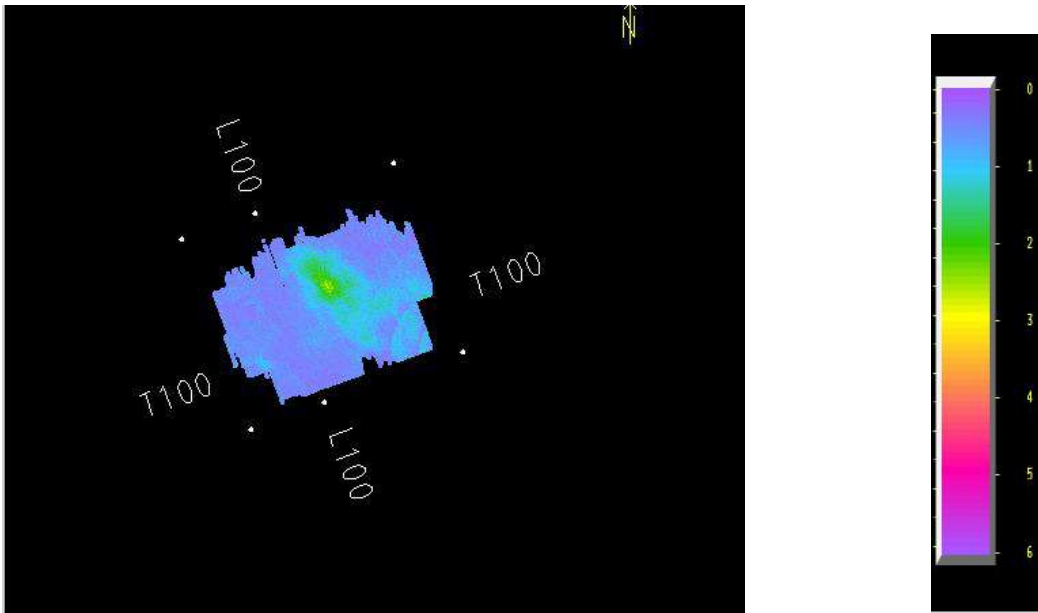


Figure 4.9 RMS amplitude map between horizon 1 and horizon 3 for data (full-stack) orthogonal to the fracture direction computed over the entire survey

Lastly, I extracted RMS amplitudes maps 40-ms above Horizon1. Figures 4.10 and figure 4.11 show the map for the two sectored dataset

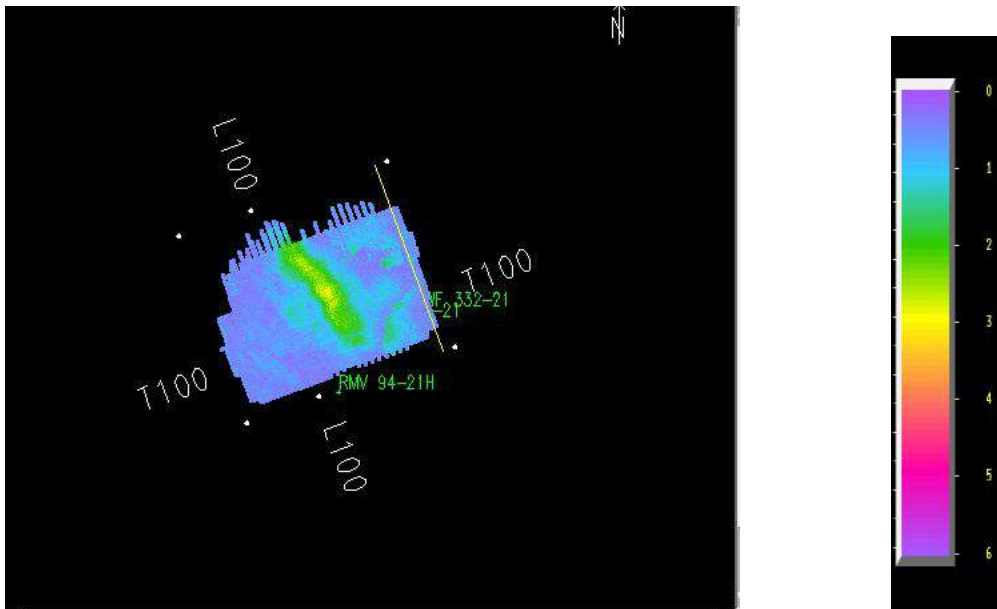


Figure 4.10 RMS amplitude map extracted 40ms above horizon 1 for data parallel to the fracture direction computed over the entire survey

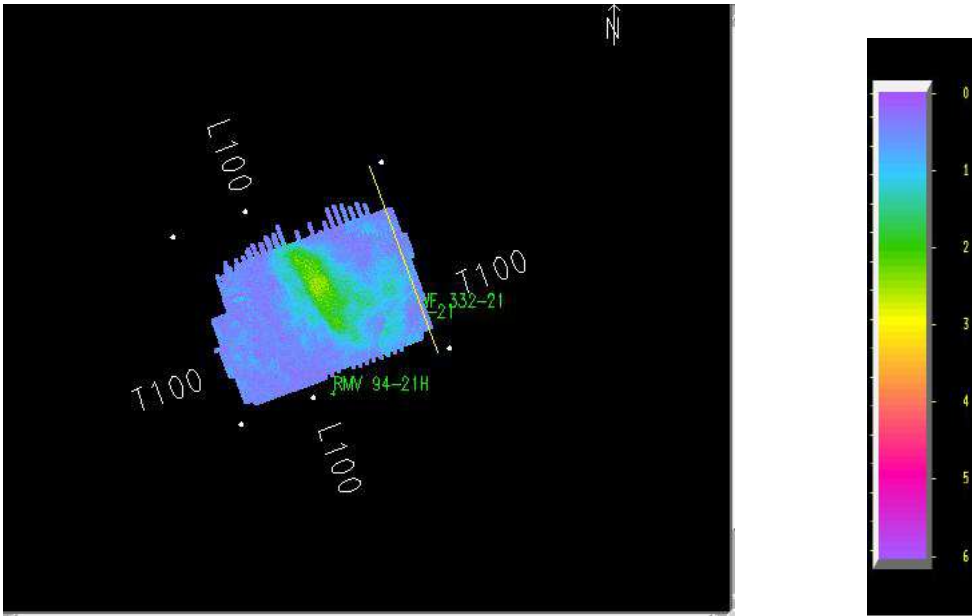


Figure 4.11 RMS amplitude map extracted 40ms above horizon 1 for data orthogonal to the fracture direction computed over the entire survey

4.2 Observations from the amplitude analysis

After a careful comparison of the RMS amplitude maps of the all-offset, migrated data parallel to the fracture orientation with the amplitude maps of the all-offset migrated data perpendicular to the fracture direction (Figure 4.2 – Figure 4.7), I noticed that the RMS amplitude maps generated from both azimuth-separated volumes look similar in terms of magnitudes and trends. This result is similar to what I observed in the synthetic modeling. The amplitudes are almost azimuthally invariant because of the low contrast in the anisotropic parameters between the overburden and the coal, which cannot be detected due to the low signal-to-noise ratio of the prestack P-wave data and the thickness of the coal which is below the tuning thickness. There is a slight difference in the RMS amplitude maps for the whole interval between horizon 1 and Horizon 3 for the two azimuthally

separated volumes (Figure 4.8 and Figure 4.9); this interval consisted of mixed lithologies. Also, there is a similar trend in the difference of the RMS amplitude maps extracted 40-ms above horizon 1 for the two azimuthally separated volumes (Figure 4.10 and Figure 4.11).

4.3 AVO Attributes Computation

In order to better characterize the fractures in the coal interval, I computed AVO attributes for each of the two azimuth-separated datasets. The attributes computed were the intercept stack, the gradient stack, and the curvature stack. They were computed from the near-stack, the mid-stack and the far-offset stacks. I used the Landmark's AVO modeling software, Well Seismic Fusion, for the computation of these AVO attributes. During the AVO processing step, three attributes were fitted from the near-stack, the mid-stack and the far-offset stacks. The algorithm computed the sine-squared of the angle of incidence for each sample of each offset for the second term and a higher-order attribute for the third term of the fit. The sine-squared tangent-squared option was selected in the AVO modeling software for the computation of the higher-order attribute. The algorithm outputs pseudo-stacks sections; the three output datasets corresponds to the intercept (A), the gradient (B) and the curvature(C). These are the A, B, C coefficients of the Shuey's 3-term AVO equation:

$$R_p(i) = A + B \sin^2 i + C \sin^2 i \tan^2 i \quad 4.1$$

where i is the angle of incidence. Figure 4.12, 4.13 and 4.14 show the intercept, the gradient, and curvature-stacks for the two azimuth-separated seismic volumes. There is no systematic difference in the first two AVO attributes when compared visually.

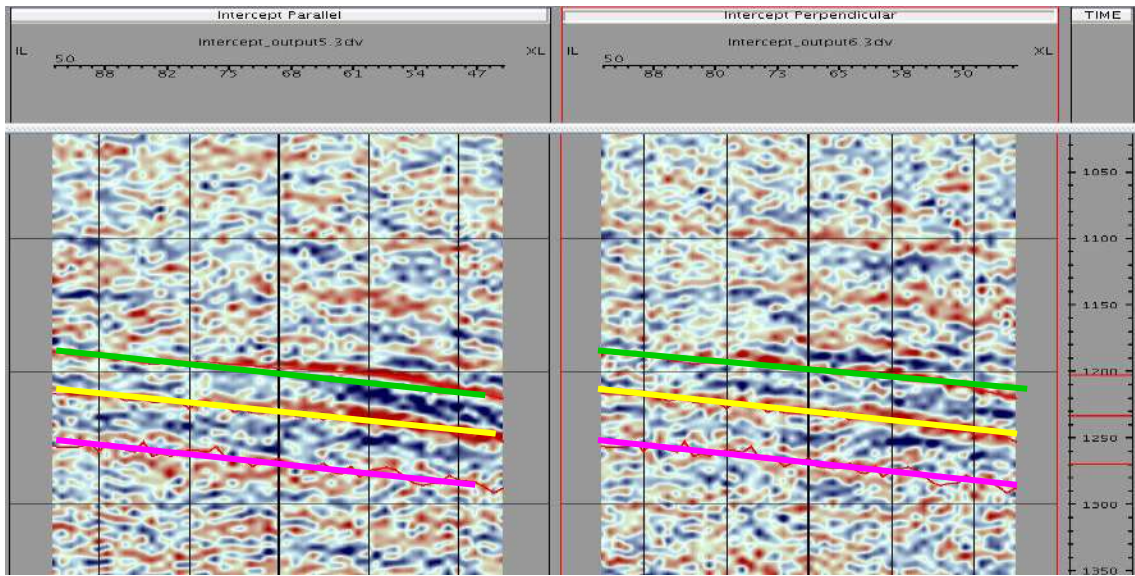


Figure 4.12 Intercept pseudo-stack volumes. The data on the left is the data parallel to the fracture direction while the volume on the right is the data orthogonal to the fracture direction.

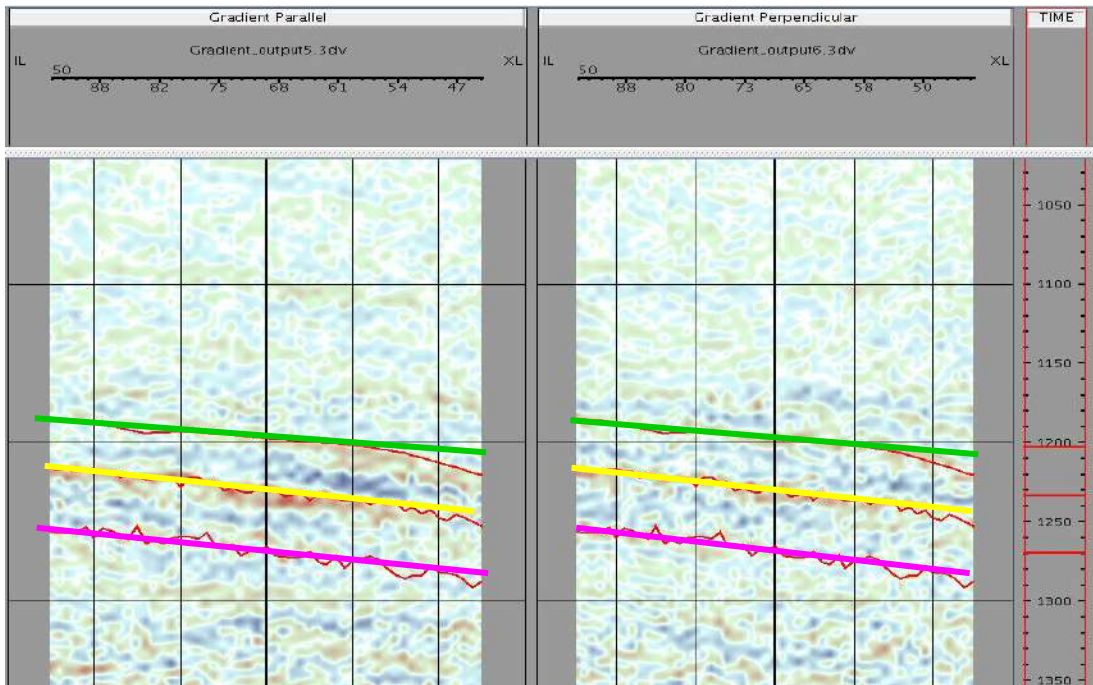


Figure 4.13 Gradient pseudo-stack volumes for the azimuth-separated volumes

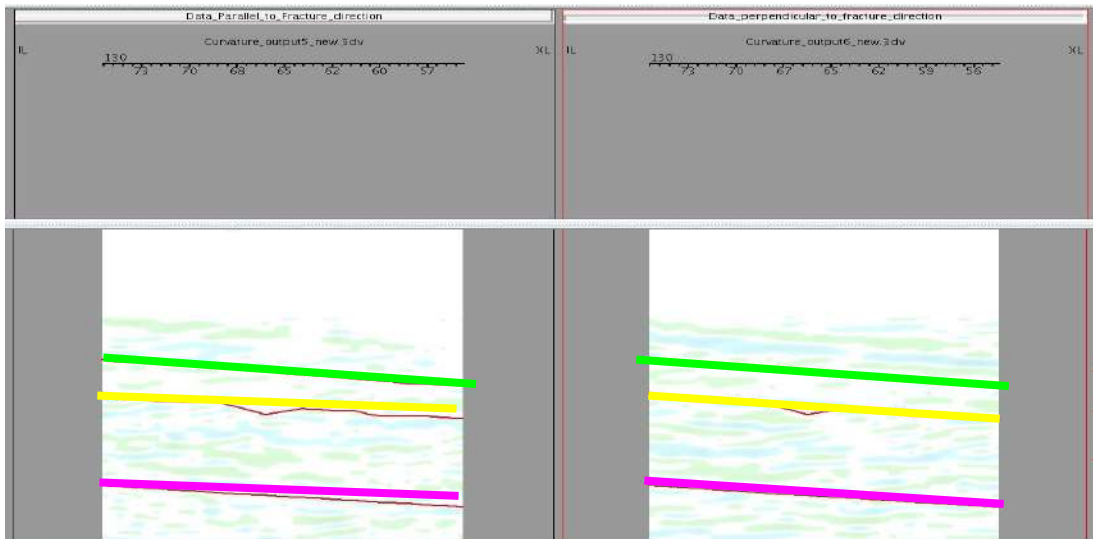


Figure 4.14 Curvature pseudo-stack volume for each of the two azimuth separated volumes. The data on the left is the data parallel to the fracture direction while the volume on the right is the data orthogonal to the fracture direction.

4.4 Crossplot Analysis

Amplitude versus offset (AVO) interpretation can be facilitated by crossplotting the extracted AVO attributes, the AVO intercept (A) and the AVO gradient (B). These are the A, and B, coefficients of the 3-term AVO equation (equation 3.2). Figure 4.15, 4.16, and figure 4.17 are the intercept and gradient crossplots for horizons 1 through 3 respectively.

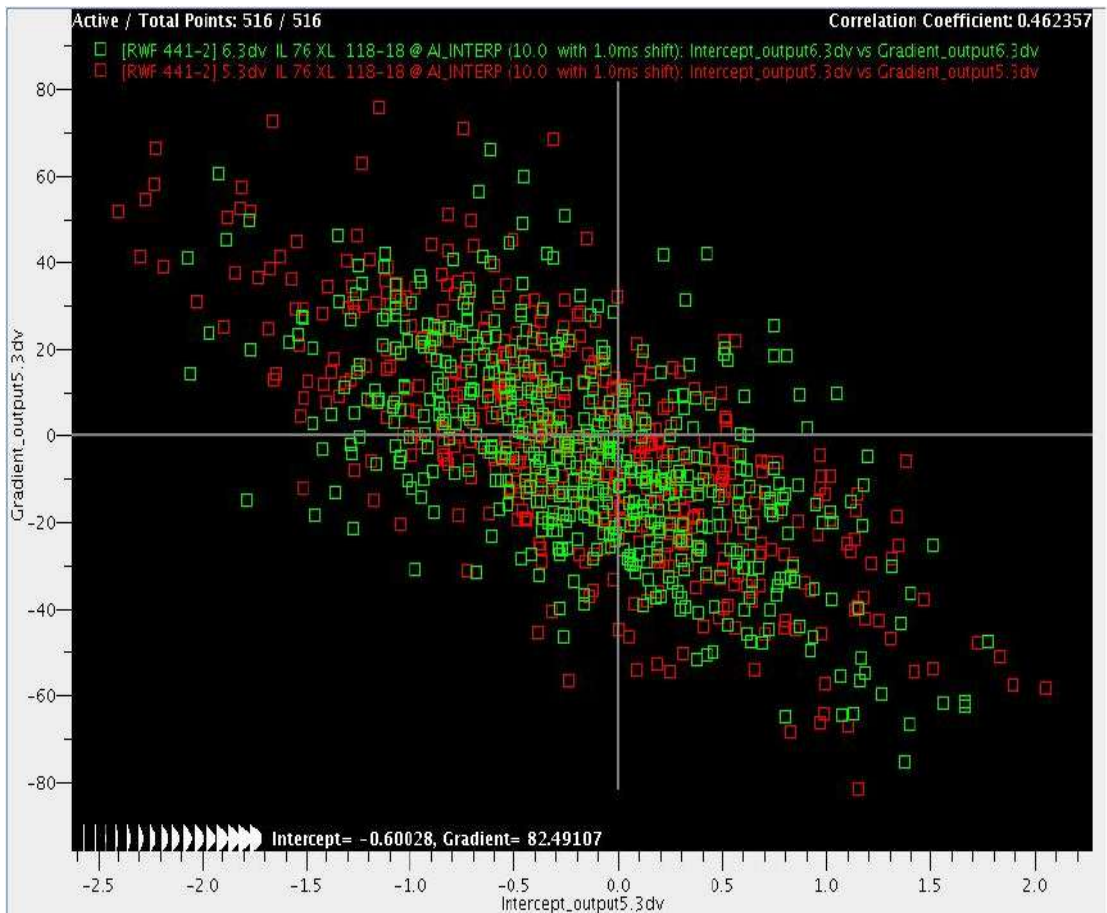


Figure 4.15 The Intercept and Gradient crossplots for horizon 1. The data points for data parallel to the fracture direction are in red while data points for data orthogonal to the fracture direction are in green.

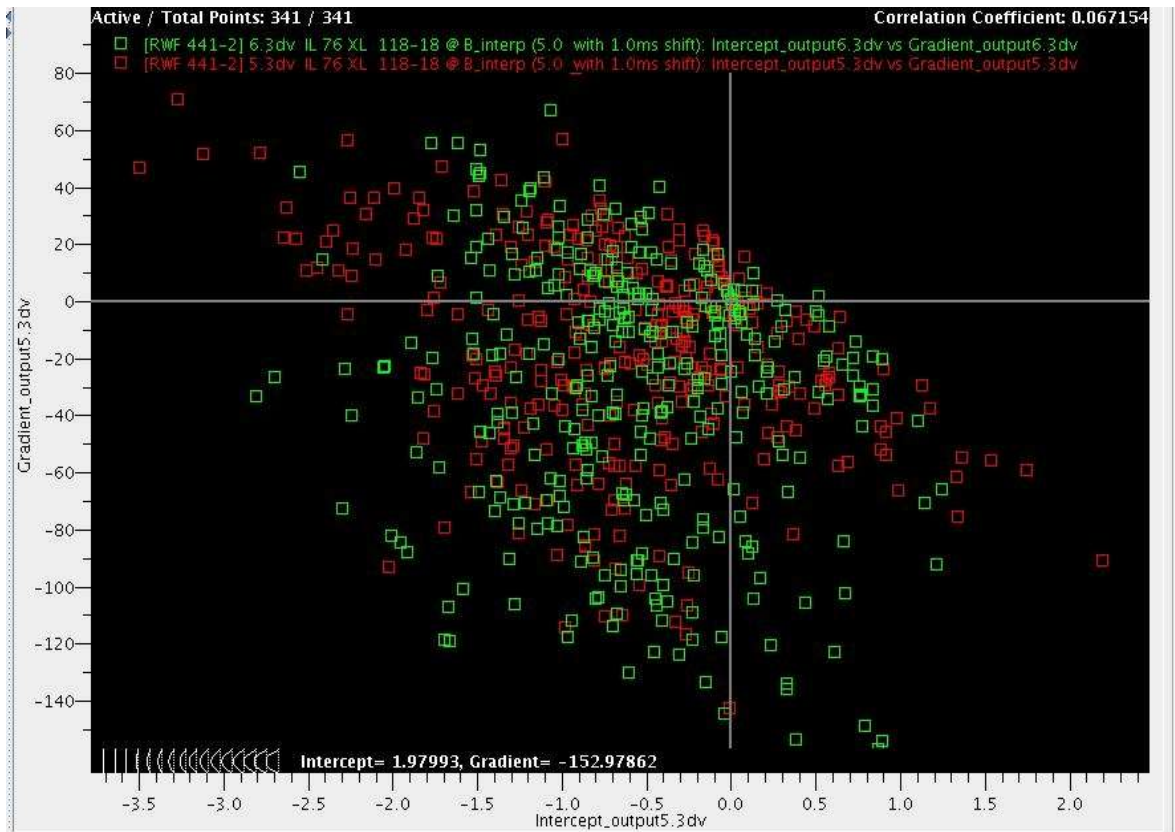


Figure 4.16 The Intercept and Gradient crossplots for horizon 2
 The Crossplot for data parallel to the fracture direction is in red while Crossplot for data orthogonal to the fracture direction is in green.

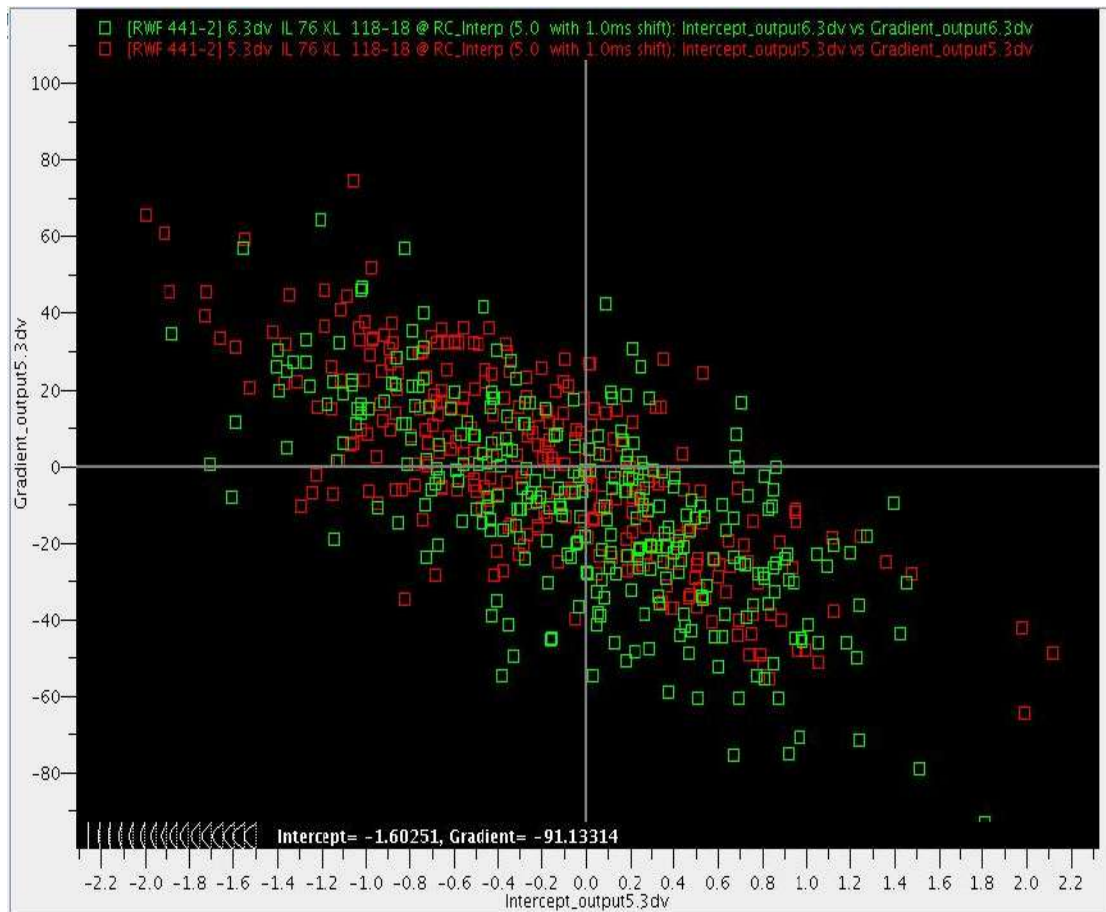


Figure 4.17 the Intercept and Gradient crossplots for horizon 3. The Crossplot for data parallel to the fracture direction is in red while Crossplot for data orthogonal to the fracture direction is in green.

4.5 Interpretation of the AVO Crossplot

I crossplotted the intercept and gradient to see if there would be any systematic relationships between the two attributes and also to determine if the AVO attributes will be azimuthally-variant.

The azimuthal variance in the intercept and gradient for all the three horizons cannot be detected due to the signal-to-noise ratio of the data. The crossplots for both of the azimuthal separated data are almost the same for the three horizons. Systematic difference between crossplots for the two datasets is so small and it

cannot be detected due to the poor S/N ratio. A slight dissimilarity is seen in the curvature volumes for the two azimuth-separated datasets; this is due to the fact that the curvature term gives the amplitudes at the far-offset but unfortunately the uniform azimuthal coverage of the prestack P-wave data only extended to offsets of about 5500ft. Figure 4.18 shows the offset-azimuth plot. After about 5500 ft of offset, the azimuthal coverage is unevenly sampled.

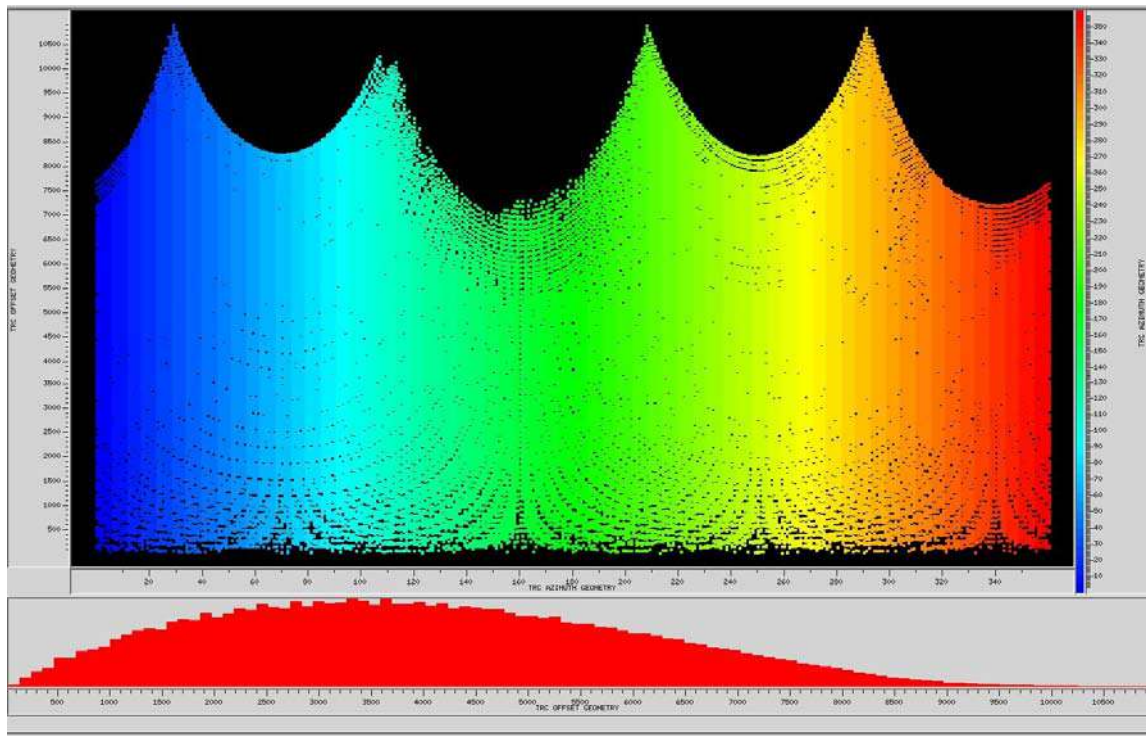


Figure 4.18 Plot of offset as a function of azimuth for all the traces in the survey. Offset is plotted in the vertical axis while azimuth is plotted in the horizontal axis.

Synthetic modeling shows that the azimuthal variation in reflection coefficient is only distinctly visible beyond 30-degree incidence angle or after 9000 ft of offset. Unfortunately, we do not have uniform azimuth coverage for offsets beyond 5500 ft and this makes it impossible to adequately detect the azimuthal-variation in the amplitudes of the two azimuth-separated datasets.

4.6

Error Analysis

The prestack dataset used for this project was contaminated with noise. Thus, I found it necessary to carry out a statistical analysis to quantify the amount of noise found in the substacked, prestack migrated data used for the computation of the AVO attributes volumes in the two orthogonal directions.

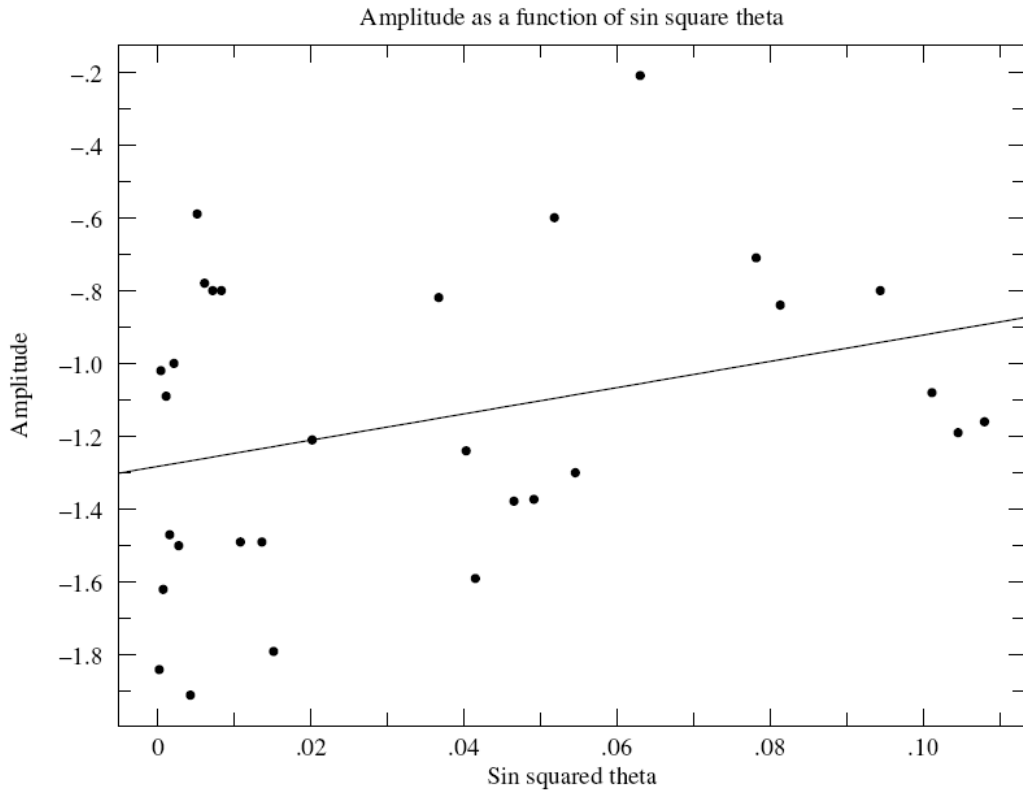


Figure 4.19 Amplitudes plotted as a function of $\sin^2\theta$ for the data parallel to the fracture direction.

Figure 4.19 shows the amplitudes plotted as a function of $\sin^2\theta$ for the data parallel to the fracture direction. The Least squares method was used to fit the best straight line to the data set.

$\sin^2\theta$ was computed using Walden's equation (equation 3.29, chapter 3). The amplitudes were estimated at the Cameo Horizon from the P-wave data set that I used for the AVO attributes computation. (Please see the appendix for the data). I computed the standard deviation of the amplitudes because standard deviation is one of several indices of variability that statisticians use to characterize the dispersion among the measures in a given set of data. It measures the spread in the values. If many data points are close to the mean, the standard deviation will be small; if many data points are far from the mean, then the standard deviation will be large. If all the data values are equal, then the standard deviation is zero. The mean of the data set used for the plot above (figure 4.19) is -1.16 while the standard deviation is 0.42. Thus, we can see that the data is dispersive. An ordinary least squares method was first used to fit the best straight line to the data set (Figure 4.19).

The straight line is given as $y = a + bx$ where:

Intercept (a) = -1.28 ($\sigma_a = 0.10$)

gradient (b) = 3.60 ($\sigma_b = 1.7$)

σ_a and σ_b are the expected range of variation for the intercept and gradient respectively. Correlation coefficient (r) indicates the extent to which the pairs of numbers for these two variables (amplitude and $\sin^2\theta$) lie on a straight line

The correlation coefficient (r) calculated for this data set = 0.316.

Will G. Hopkins (internet source) wrote that the correlation coefficient (r) of less than 0.1 is very poor. Thus a correlation coefficient of 0.316 is poor.

Also, I fit the same data to another straight line using the least absolute deviation method. This method is a mathematical optimization technique similar to the least squares technique in that it attempts to find a function which closely approximates a set of data. In the simple case of a set of (x,y) data points, the approximation function is a simple "trend line" in 2D Cartesian coordinates. The method reduces the sum of absolute errors, between points generated by the function and corresponding points in the data. Figure 4.20 shows the trend lines fitted by both the ordinary least square and the least absolute deviation methods.

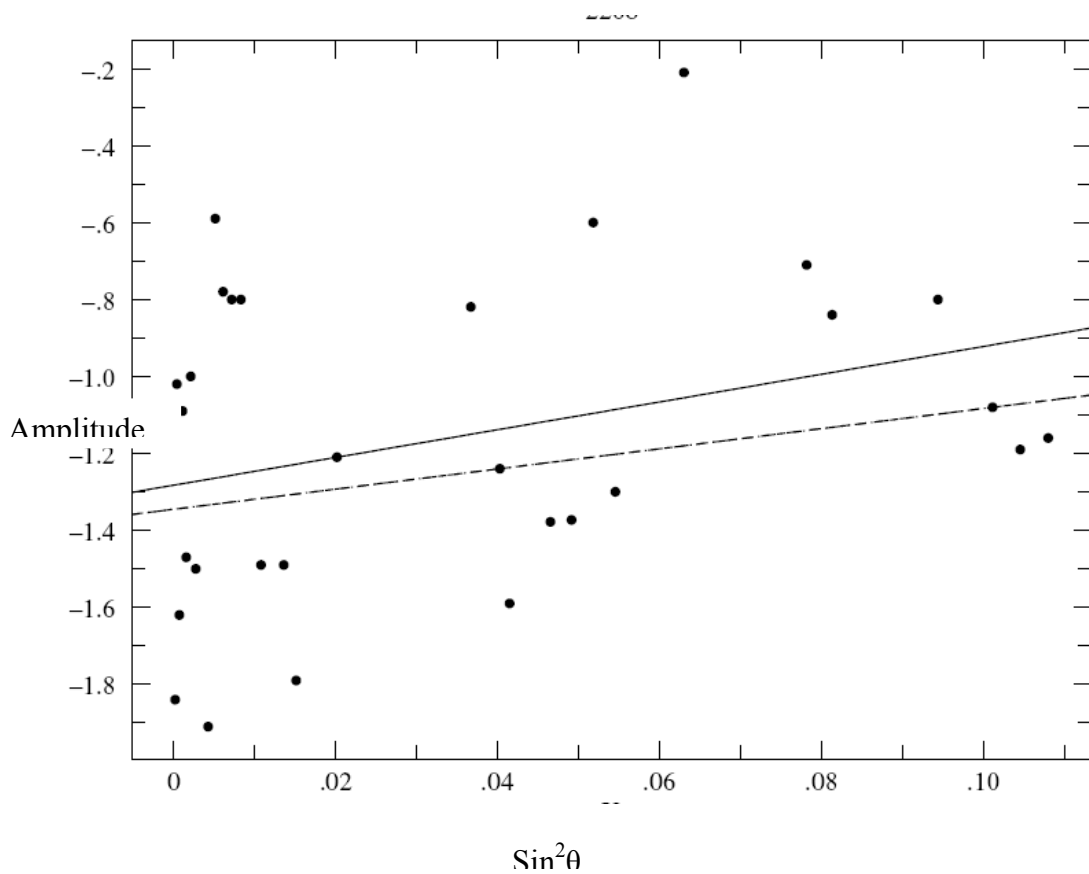


Figure 4.20: Plot of amplitudes as a function of $\text{Sin}^2\theta$ for the data parallel to the fracture direction.

The results for the computation with the ordinary least square method are:

Intercept (a) = -1.313 ($\sigma_a = 0.15$), gradient (b) = 5.189 ($\sigma_b = 2.8$),

Correlation coefficient (r) = 0.334. σ_a and σ_b are the expected range of variation for the intercept and gradient respectively.

The intercept (a) computed using the least absolute deviation method is -1.409 and the gradient (b) is 4.257. The average deviation = 0.402.

From this statistical analysis, we can see that it is possible to fit many straight lines to each of the two azimuth sector datasets; this shows that the amplitudes of the dataset analyzed for this project are quite dispersed. The dispersion is due to the low signal-to-noise ratio of the prestack P-wave data. There is a large uncertainty in the values of the AVO intercepts and gradients computed for two orthogonal datasets because of this low signal-to-noise ratio of the dataset; this huge uncertainty makes it difficult to see a systematic difference in the AVO attributes for the two orthogonal directions when compared. Modeling predicts a 3% percent difference in the reflection coefficients between parallel and perpendicular azimuths at the 6000-foot offset distance. In order to see this difference in the real data we need a dataset that is devoid of noise. This statistical analysis shows that the standard deviations of the datasets are around 0.4, thus indicating that the noise in the seismic data analyzed is high. A standard deviation value less than 0.1 is required in the dataset in order to be able to see the azimuthal variation in amplitudes. The low signal-to-noise level in

the dataset analyzed made it difficult to see the differences in the amplitudes in the two orthogonal directions.

4.7 Summary

The RMS amplitudes maps computed for the reflection from the top of coal do not demonstrate a systematic azimuthal effect above the noise level. The small contrast in Thomsen's parameters causes a small difference in the amplitudes of the two orthogonal datasets. These systematic differences in amplitudes are not detectable due to the noise in the data and also because the acquired offsets are not sufficient to provide reflection angles greater than 20 degrees. However, there is a slight difference in the RMS amplitude maps for the whole interval (i.e. interval between horizon 1 and horizon 3) for the two azimuthal separated volumes; this whole interval also consist other lithologies which will also be sensitive to the azimuthal variation in velocity. The magnitudes i.e. the range of slope and intercept values are almost equal for both of the azimuth-separated data, thus indicating that the reflections from the coal interval are almost azimuthally invariant. While recognizing that the larger contrasts in the Thomsen parameters would have created larger and perhaps more distinguishable azimuthal dependence, from all evidence, that is not the case. The small difference in the gradients of the two-azimuthally separated data is not detectable in the data due to the low signal-to-noise ratio of the data and also due to lack of extreme offsets at all azimuths.

CHAPTER 5

CONCLUSIONS AND RECOMMENDATIONS

5.1 Conclusions

The objectives of this study were to delineate areas of high fracture density within the Cameo coal interval at Rulison Field in Piceance Basin, Colorado using multi-azimuth prestack P-wave data and also to investigate the influence on AVO of the orientation of the seismic lines relative to the fractures. Based on my AVO analysis at the Cameo interval, Colorado, I conclude:

1) Modeling shows that for the top-of-coal reflections to be azimuthally-dependent; there must be a contrast in Thomsen's anisotropic parameters. Modeling also shows that the azimuthal variation in reflection coefficient increases dramatically for very large far-offset distances.

2) I was unable to observe convincingly a systematic azimuthal dependence to the AVO. There are a variety of contributing factors. Given the best-guess values for the Thomsen parameters, the azimuthal AVO is modest for the range of offsets in the data. In addition, the airwave, even though attenuated, hinders the AVO measurements.

3) Modeling shows that the reflection from the top of a coal (i.e. interface between the overburden and the coal) is a trough, whose amplitude decreases

as a function of offset. If this were a gas sand reservoir, it would be noted as a Class IV AVO anomaly (Castagna et al., 1998).

5.2 Recommendations for Future Studies:

Azimuthal AVO is one of the techniques used in the oil and gas industry for delineation and characterization of fractures (Maria A Perez et al, 1999), but there are many factors that must be met before this technique yields a reasonable result. For future studies in Rulison Field, I make these recommendations:

- 1) Even though synthetic modeling shows the azimuthal variation in reflection coefficient, other factors distort the observed azimuthally varying seismic amplitudes. These factors include processing steps such as trace equalization. Trace equalization should be avoided if possible for processing; this might affect the relative amplitudes of the data. Rueger (2001) suggested that the conventional processing algorithm has to be modified to process each azimuthal direction separately, thus preserving the azimuthal varying seismic amplitudes.
- 2) The shear-wave data should be analyzed because of shear-wave splitting that occurs when a plane wave is incident on an HTI medium outside the symmetry axis plane and isotropy plane. Both the fast and the slow shear-wave datasets should be analyzed and the results from the AVO analysis should be compared.

3) Proper direction of the fractures should be determined. The analysis of the stacked data for several azimuthal ranges can reveal the proper fracture direction but this can only be achieved with proper (azimuthally varying) normal-moveout velocity. As pointed out by Franco (2007), it is important to understand that in the case where multiple fractures sets exist, two or more directions of high open fracture density will cause the P-wave azimuthal anisotropy to approach zero provided the rock is overpressured. (The pressure will keep the cracks opened).

4) Thomsen's anisotropic parameters should be estimated properly for the study area. These elastic properties of the desired reflector and the overburden must be known in detail for a better azimuthal AVO analysis. Vertical seismic profiling (VSP) can be used to estimate the in-situ anisotropy. This can be done by the joint inversion of the slowness and polarization vectors of P and SV-waves for parameters, and this should be done without assuming a priori symmetry or any other kind of anisotropy. Pawan Dewangan and Vladimir Grechka (2003) concluded that given a sufficient polar and azimuthal coverage of the VSP data, the polarizations and the slownesses of the P and the two split shear (S1 and S2) waves are sufficient for estimating the 21 stiffness coefficients efficient (C_{ij} s) that characterize the most general triclinic anisotropy. Unfortunately, the VSP data available in Rulison Field do not have the adequate information required for the proper estimation of the in-situ anisotropic parameters. The 2003 VSP data that Franco analyzed only covered the overburden (4600- 5050 ft). The 2006 VSP data covered the reservoir interval and the coal interval but unfortunately the data lacked adequate vertical P-wave vibrator coverage (Praj, 2008).

5) The offset distribution in different azimuthal directions must be more uniform than with the current survey. The geophones should be planted in areal distribution to ensure that the offset distribution is uniform in the different azimuthal directions. Also, large-offset distances should be acquired because modeling shows that the azimuthal variation in reflection coefficients can be seen more distinctly in the far offset with greater than 20-degree incidence angle. This uniformity in the offset distribution is necessary for a better comparison of the AVO result in the ideally-perpendicular directions.

REFERENCES

- Aki, K. and Richards, P. G., 1980, Quantitative seismology: Theory and methods: W. H. Freeman and Co.
- Banik, N. C., 1987, An effective anisotropy parameter in transversely isotropic media: *Geophysics*, 52, 1654–1664.
- Bortfeld, R., 1961, Approximation to the reflection and transmission coefficients of plane longitudinal and transverse waves: *Geophysics. Prospecting*, 9, 485–503.
- Burke, L., 2005, Anisotropy from RWF 542-20 cross dipole sonic log analysis; Reservoir Characterization Project Report, spring 2005 Sponsor Meeting, Colorado School of Mines, Golden.
- Castagna, J. P., 1993, AVO analysis: Tutorial and review, in Backus, M. M., Ed., *Offset-dependent reflectivity—Theory and practice of AVO analysis: Soc. Exploration Geophysics* 3–36.
- Castagna, J. P., Batzle, M. L., and Eastwood, R. L., 1985, Relationships between P-wave velocities in elastic silicate rocks: *Geophysics*, 50, 571–581.
- Castagna, J.P., Swan, H.W., and Foster, D. J., 1998, Framework for AVO gradient and intercept interpretation: *Geophysics*, 63, 948–956.
- Cumella, S.P., and D.B. Ostby, 2003, Geology of the basin-centered gas accumulation, Piceance Basin, Colorado. *Piceance Basin 2003 Guidebook: Rocky Mountain Association of Geologists*, 171-193.
- Cumella, S.P., 2006, Overview of a giant basin-centered gas accumulation, Mesaverde Group, Piceance Basin, Colorado, in S.A. Sonnenberg, and E.D. Dolly, eds., *The Mountain Geologist*, A special theme issue on Rocky Mountain gas reservoirs revisited. *Rocky Mountain Association of Geologists*, v. 43, No. 3, p. 219-224.
- Davis, T., 2005, Phase XI proposal: Integrating dynamic data into high resolution reservoir characterization II – Time-lapse multicomponent seismic, geomechanical modeling and flow simulation at Rulison field, Colorado School of Mines.
- Embree, P., 1966, Diversity seismic record stacking method and system

Guliyev, E., 2007, Vp/Vs estimation from multicomponent seismic data for improved characterization of a tight sandstone gas reservoir, Rulison Field, Colorado. M.S. thesis, Colorado School of Mines.

Hemborg, H. T., 2000, Gas production characteristics of the Rulison, Grand Valley, Mamm Creek, and Parachute Fields, Garfield County, Colorado: Turning marginally economic Basin-centered Tight-Gas Sands into profitable reservoirs in the southern Piceance Basin: Colorado Geological Survey, Resource Series 39, p. 1-30.

Higgins, S., 2006, Geomechanical modeling as a reservoir characterization tool at Rulison field, Piceance basin, Colorado. M.S. thesis, Colorado School of Mines.

Jansen, K., 2005, Seismic investigation of wrench faulting and fracturing at Rulison Field, Colorado. M.S. thesis, Colorado School of Mines.

Keighley, D., 2006, P-wave Time Lapse seismic data interpretation at Rulison Field, Piceance Basin, Colorado. M.S. thesis, Colorado School of Mines.

Koefoed, O., 1955, On the effect of Poisson's ratios of rock strata on the reflection coefficients of plane waves: *Geophys. Prosp.*, 3, 381–387.

Kusuma, M., 2005, Analysis of time-lapse P-wave seismic data from Rulison field, Colorado. M.S. thesis, Colorado School of Mines.

Matesic, M., 2007, Structural and stratigraphic controls on Mesaverde reservoir performance: Rulison Field, Garfield County, Colorado. M.S. thesis, Colorado School of Mines.

Mavko, G., T. Mukerji, and J. Dvorkin. *The rock physics handbook: Tools for seismic analysis in porous media*: Cambridge University Press, 1998.

Ostrander, W. J., 1984, Plane-wave reflection coefficients for gas sands at non-normal angles of incidence: *Geophysics*, 49, 1637–1648.

Ramos, A.C.B., 1993, PhD T-4481, Three-dimensional AVO analysis and anisotropic modeling applied to fracture characterization in coal bed methane reservoirs, Cedar Hill Field, San Juan Basin, New Mexico.

Rojas, E., 2005, Elastic rock properties of tight gas sandstones for reservoir characterization at Rulison field, Colorado. M.S. thesis, Colorado School of Mines.

Ruger, A., 1997, P-wave reflection coefficients for transversely isotropic models with vertical and horizontal axis of symmetry: *Geophysics*, 62, 713–722.

Rumon, M., 2006, Shear wave time-lapse seismic monitoring of a tight gas sandstone reservoir, Rulison field, Colorado. M.S. thesis, Colorado School of Mines.

Rutherford, S. R., and Williams, R. H., 1989, Amplitude-versus-offset variations in gas sands: *Geophysics*, 54, 680–688.

Samec, P., and Blangy, J. P., 1992, Viscoelastic attenuation, anisotropy, and AVO: *Geophysics*, 57, 441-450

Scheevel, J. and S. P. Cumella, 2005, Stratigraphic and rock mechanics control of Mesaverde gas distribution. Piceance Basin, Colorado: RMAG PTTC Fall Symposium.

Shuey, R. T., 1985, A simplification of the Zoeppritz equations: *Geophysics*, 50, 609–614.

Smith, G., and Gidlow, P. M., 1987, Weighted stacking for rock property estimation and detection of gas: *Geophys. Prosp.*, 35, 993–1014.

Thomsen, L., 1986, Weak elastic anisotropy: *Geophysics*, 51, 1954-1966.

Thomsen, L., 2002, Understanding seismic anisotropy in exploration and exploitation:

SEG/EAGE Distinguished Instructor Short Course Lecture Notes, No. 5.

Tsvankin, I., and L. Thomsen, 1994, Nonhyperbolic reflection moveout in anisotropic media: *Geophysics*, 59, 1290–1304.

Tsvankin, I., 1997, Anisotropic parameters and P-wave velocity for orthorhombic media: *Geophysics*, 62, 1292–1309.

Tsvankin, I. *Seismic signatures and analysis of reflection data in anisotropic media*: Elsevier, 2001.

Vasconcelos, I. and V. Grechka, 2006, Seismic characterization of multiple fracture sets from multicomponent, multi-azimuth, 3D data: Rulison Field, CO: CWP Project Review.

Verm, R., and Hilterman, F., 1995, Lithology color-coded seismic sections: The calibration of AVO crossplotting to rock properties: *The Leading Edge*, 14, No. 7, 847–853.

Walden, A.T., 1991, Making AVO sections more robust: *Geophys. Prosp.*, 39, 915-942

Xu, X., 2006, Anisotropic geometrical spreading correction and its application in azimuthal AVO analysis. Ph.D. thesis, Colorado School of Mines.

Yilmaz Ö., 2001, *Seismic Data Analysis*: Society of Exploration Geophysicists
http://en.wikipedia.org/wiki/Least_absolute_deviations

http://www.physics.csbsju.edu/stats/fitting_lines.html

APPENDIX A

REGIONAL GEOLOGY OF RULISON FIELD

A.1 Geologic Setting of Piceance Basin

The Piceance is a northwest trending asymmetrical, Laramide-age basin in the Rocky Mountain foreland with gently dipping western and southwestern flanks and a sharply upturned eastern flank (Tremain and Tyler, 1997). The Douglas Creek Arch bounds the basin on the northwest, and separates it from the Uinta Coal Basin which lies almost entirely in Utah. The Mesaverde Group is sharply upturned to near vertical along the Grand Hogback, which forms the eastern boundary of the basin and separates the basin from the White River uplift to the east. Most of the Piceance Basin's coal deposits are contained in the Iles and Williams Fork Formations of the Late Cretaceous Age Mesaverde Group which are approximately 100 to 65 million years in age.(McFall et al., 1986). These formations composed of sandstone and shale were deposited in a series of regressive marine environments (McFall et al., 1986; Johnson, 1989). It is believed that the coals were deposited in marine transitional, brackish, interdistributary marshes and freshwater deltaic swamps (Collins, 1976 in McFall et al., 1986). The Mesaverde Group is underlain by the marine Mancos shale and overlain by the lower Tertiary Age Fort Union and Wasatch Formations which consist of fluvial sandstones and shales. The Mancos Shale, Fort Union, and Wasatch Formations are essentially barren of coals (McFall et al., 1986). Depths to the coal-bearing sediments vary from outcrops around the margins of the basin to more than 12,000 feet in the deepest part of the basin (Tyler et al., 1996). The major fold structure of the Piceance Basin is the Grand Hogback Monocline, formed as the White River Uplift, was uplifted and thrust westward during the

Laramie Orogeny in Late Cretaceous through Eocene time (McFall et al., 1986). Broad folds, such as the Crystal Creek and Rangle Syncline, trend northwest to southeast and generally parallel to the axis of the basin. Intrusions occur throughout the southeast part of the basin, locally elevating coal ranks to as high as anthracite grade. A buried laccolith intrusion is thought to be present under a coal basin anticline along the southeast margin of the basin where high quality coal was mined since the 1800s (Collins, 1976). Coalbed methane reservoirs occur exclusively in the Upper Cretaceous Mesaverde Group which covers an area of approximately 7,255 square miles (Tremain and Tyler, 1997). Depths to the Mesaverde Group range from outcrop to greater than 12,000 feet along the axis of the basin (Tyler et al., 1996; Tremain and Tyler, 1997). Two-thirds of the coalbed methane occurs in coals deeper than 5,000 feet, making the Piceance Basin one of the deepest coalbed methane areas in the United States (Quarterly Review, August 1993). The major coalbed methane target, below the Cameo coal zone is contained within the Williams Fork Formation of the Mesaverde Group and holds approximately 80 to 136 Tcf of coalbed methane (Tyler et al., 1998). This coal zone ranges in thickness from 300 to 600 feet and lies more than 6,000 feet below the ground surface over a large portion of the basin (Tyler et al., 1998). Individual coal seams of up to 20 to 35- feet thick can be found within the group, with net coal thickness of the Williams Fork Formation averaging 80 to 150 feet thick. In 1991, at the Grand Valley field, there were 23 coalbed methane wells and 18 conventional gas wells (Reinecke et al., 1991). However, in 1984, most wells at the Rulison Field were conventional gas wells. Initially, it was

anticipated that coalbed methane wells in the sandstones and coals of the Cameo zone would have high production rates of water. However, testing later showed that they produced very little water (Reinecke et al., 1991). Both the sandstones and coalbeds are tight, poorly permeable, and are generally saturated with gas rather than water or a mixture of water and gas. The dynamic flow of a hydrologic system enhances the collection of gas in traps, but in much of the Piceance Basin that flow is not present because of the over-pressuring and saturation with gas. Consequently, the conventional models for coalbed methane accumulation developed for other basins do not apply well for exploration and development in the Piceance Basin.

A.2 Petroleum System of Piceance Basin

The source rocks for the Williams Fork Formation are interbedded gas-prone shales, mudstones, siltstones, and coals (Johnson and Roberts 2003). Spencer (1989) claims that the gas was generated and migrated into the reservoirs in Tertiary time.

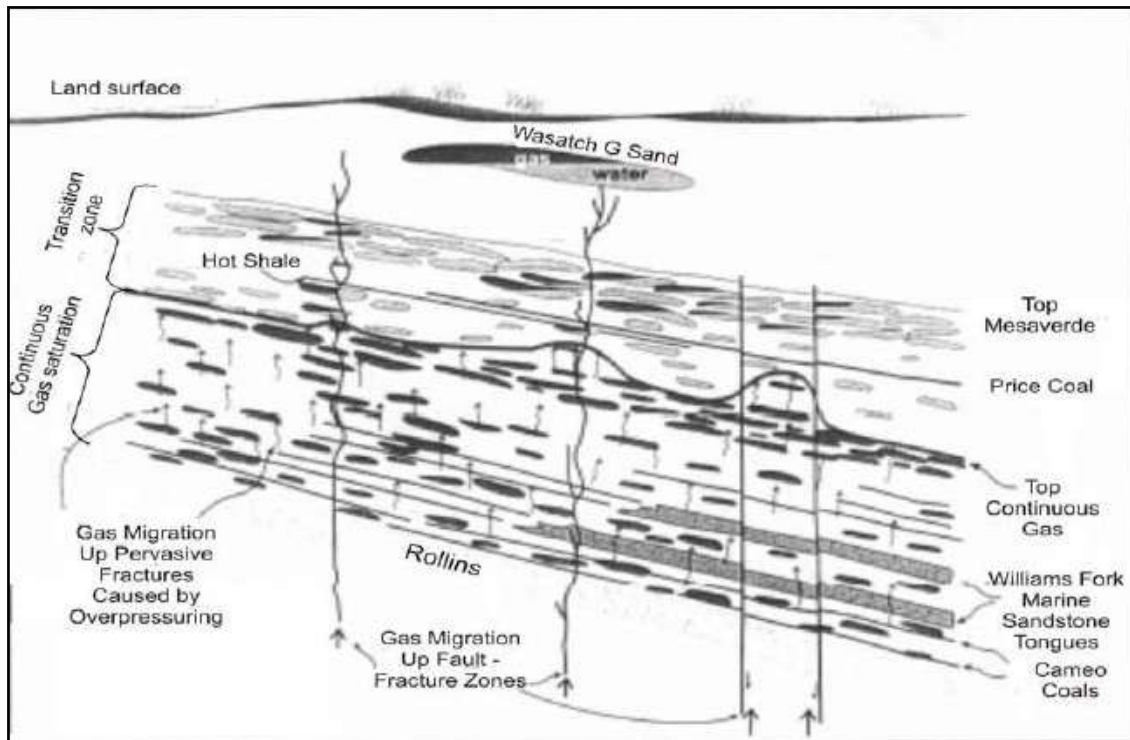


Figure A-1: Schematic cross section illustrating the gas migration model for the Mesaverde in the Piceance Basin (courtesy: Scheevel and Cummella 2005)

Both stratigraphic and diagenetic trapping mechanisms occur in the formation.

One can characterize the petroleum system with the knowledge of the source, reservoir, seal overburden rocks, and the processes of trap (Figure 1.3 and 1.4).

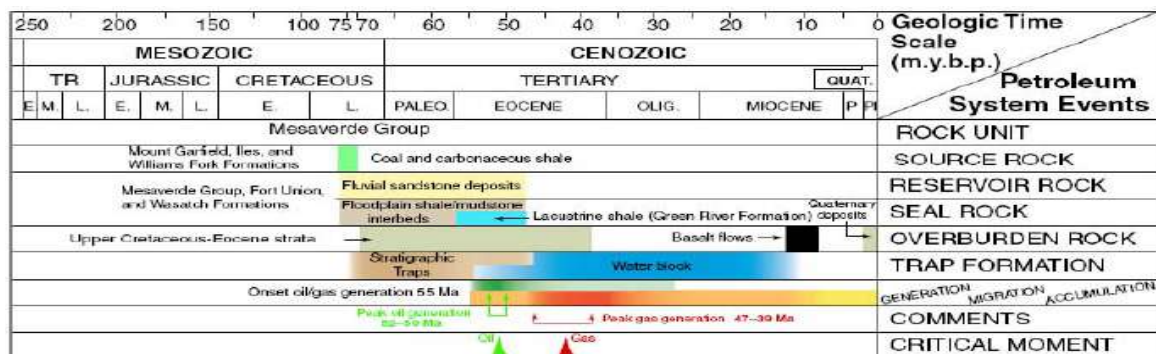


Figure A-2: illustrates the petroleum system chart for the Piceance basin. (Picture modified from Guliyev 2007)

A.3 Tectonic Evolution of the Piceance Basin

The study of the structural and tectonic evolution of the Piceance basin indicates that basement faulting, resulting from tectonics during the Precambrian, Pennsylvanian and the Laramide and younger events have shaped the development of major fault systems. This also indicates that a reactivated paleohorst and SW-NE directed regional shortening produced the dominant regional deformation and structures in the southeastern basin, including the Rulison Anticline. The basin has experienced WNW and EW compression from Holocene to present.

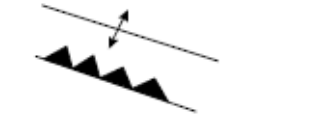
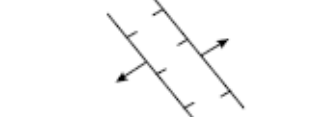
<i>Geologic Age</i>	<i>Structural Style</i>	<i>Schematic</i>
Miocene to Recent	Regional Uplift	 WNW Maximum Compression
Cretaceous to Eocene	Laramide Thrust Faults and Related Folding	 SW Directed Shortening
Pennsylvanian/ Permian	Faulting and Graben Development	 NW Trending Extension
Precambrian	Regional Crustal Shearing and Extension	

Figure A-3: Tectonic history of the Piceance basin, Rulison Field. (Picture Modified from Guliyev 2007)

Cumella and Ostby (2003) used 3D seismic data to interpret a series of faults in the Rulison area. They suggested that wrench tectonics is the dominant structural style of the northwest-trending features. They indicated a left-lateral transgressional structural style. The first set of faults showed a northwest trend (N45°W), near-vertical dip, and left-lateral slip. The second set showed a north-northwest trend (N20°W), dips of 30 to 60 degrees, and showed reverse character. A possible explanation for this system is an east-west Laramide compression that produces left-lateral slip along pre-existing northwest-trending faults. Kuuskraa et al. (1997b) suggested that the vertical overburden stress appears to be similar in magnitude to the maximum horizontal compressive stress. Therefore, fracturing has occurred perpendicular to the least and intermediate stress orientation, creating fractures with a mix of N30°W, N60°E and N70-80°W trends. The development of the major fracture in the Rulison field is shown in Figure A-4.

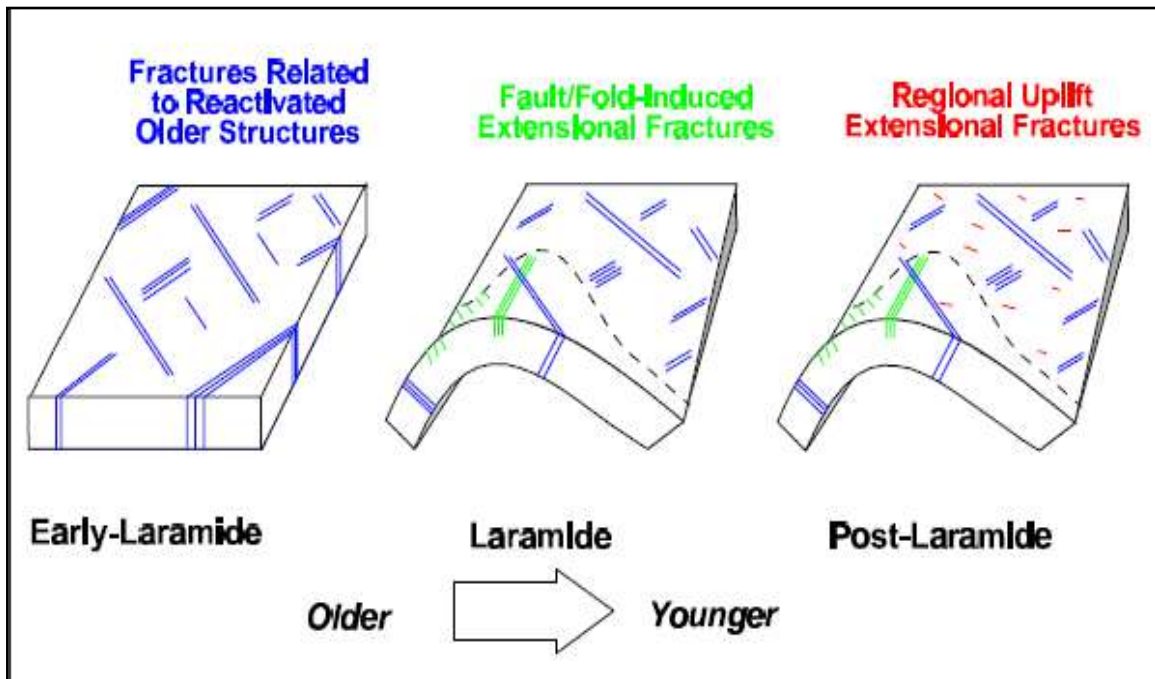


Figure A-4: Development of major fractures at Rulison Field (Modified from Guliyev 2007)

A.4 Reservoir Properties and Production History

Many of the reservoir properties were obtained from the research done during the U.S. DOE's Multiwell Experiment (MWX), a field laboratory designed to improve the characterization and production of tight gas sandstones. The MWX research is located less than 2 miles from the RCP survey area. Tight gas sandstones are highly heterogeneous and complex. The reservoir is characterized by sandstone channels, interbedded with siltstones, shales and coals. The discontinuous nature of the channels requires well spacing of 20 acres or less to adequately drain the

reservoir (Cumella and Ostby, 2003). Williams Fork Formation sandstones porosities range from 1 to 10%. Change in porosity is less than 2% for a 1000 psi confining pressure change (Sattler, 1989). Permeabilities range from 1 to 60 μ D. Water saturations range from 30 to 35% in productive sands (Cumella and Ostby, 2003) and 65% at the top of the Mesaverde Group. Log porosities range from 10 to 12%, but measured porosities in cores are lower. The upper one-third of the Williams Fork Formation is considered to have low reserve potential, due to high water saturation. The gas composition in Rulison Field is mainly methane. Reinecke et al. (1991) noted that gases above and below Cameo coal have a different composition. Gases below the Cameo coal are chemically drier (90 to 93% methane, 1 to 3% ethane, and 3 to 6% carbon dioxide) compared to sandstones gases, which are wetter (89 to 92% methane, 3 to 6% ethane, and 1 to 4% carbon dioxide). The reservoir pore pressure gradients vary from 0.433 psi per foot (normal hydrostatic gradient) to 0.68 psi per foot. During primary depletion processes, reservoir pressure decreases; however, areas that are not connected with the depletion zone stay at higher pore pressures. The pore pressure data were obtained from well tests (Nelson, 2002). The red line shown in Figure A-5 connects the measured pore pressure points.

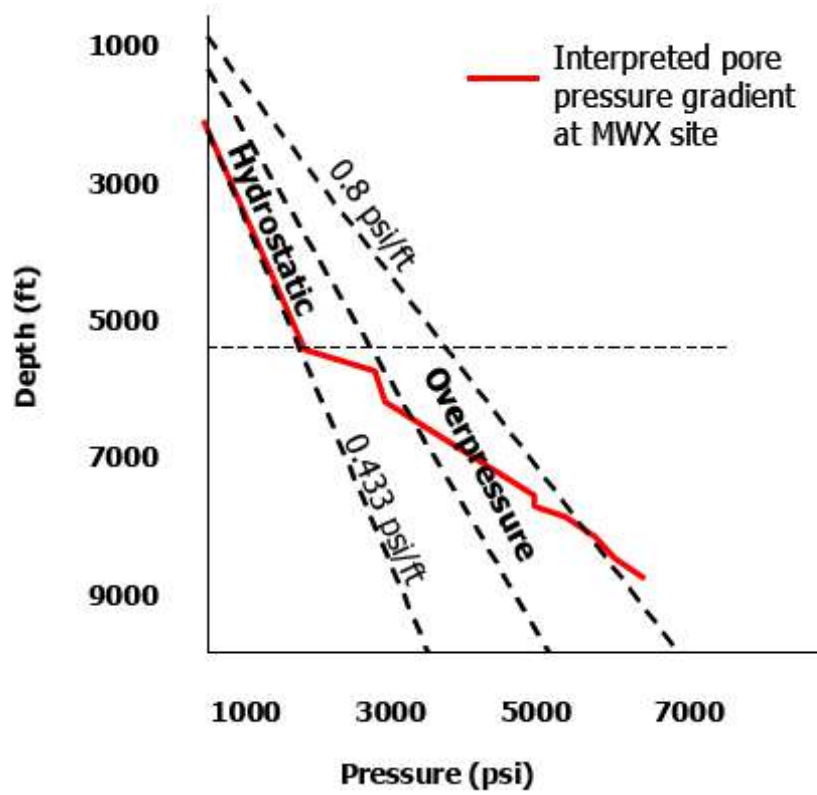


Figure A-5: Pore pressure gradient measurements as function of depth at the U.S. DOE's MWX-site. Picture modified from Spencer (1989). Pore pressure increases with depth to progressively higher gradients. Top of reservoir is approximately at 5100 ft of depth (dashed line). Picture from (Rojas 2005).

APPENDIX B

DIVERSITY STACK ALGORITHM

B.1 Diversity Stack

The algorithm was developed based on the assumption that there might be varying amount of signal energy from the source and also that the noise might vary in intensity. Embree expressed the relationship between the signal and the noise constituents for consecutive seismic events in time as:

$$a_1S + b_1N \tag{2.1}$$

$$ka_2S + kb_2N \tag{2.2}$$

where:

a_1 is the scalar function in the first record

S is the signal

N is the noise

b_1 is the scalar function for the RMS noise in the first seismic event

a_2 is the scalar function for the signal energy in the second seismic event

b_2 is the scalar function for the noise energy in the second seismic event.

k is the factor to be applied to the second seismic event (equation 2.2) before adding it to the first seismic event (i.e. equation 2.1).

Embree (1966) expressed the sum of the signal and noise power as:

$$\left(a_1 + ka_2 \right)^2 S^2 + \left(b_1^2 + k^2 b_2^2 \right) N^2 \quad 2.3$$

He further expressed the ratio of the signal power to noise power as:

$$\frac{\left(a_1 + ka_2 \right)^2 S^2}{\left(b_1^2 + k^2 b_2^2 \right) N^2} \quad 2.4$$

He took a derivative of the signal-to-noise power with respect to the scalar function k , when set equal to zero. He then solved the derivative for the scalar k and obtained:

$$k = \frac{a_2 b_1^2}{a_1 b_2^2} \quad 2.5$$

Equation 2.5 means that the scalar k is proportional to $\frac{b_1^2}{b_2^2}$ for the noise and the signals should be combined with amplitudes inversely proportional to the square root of the noise in a given trace. The relationship is expressed as:

$$\frac{S}{N^2} = \frac{\text{Signal Amplitude}}{\text{Noise Power}}$$

2.6

Embree (1966) also stated that, since the signal power is in phase due to the time coincidence, then the signal power is proportional to the square of the sum of amplitudes while the noise power, because of lack of correlation in time, is proportional to the sum of the two input powers. If both the signal amplitude and the noise amplitude can be evaluated before stacking, then an optimum stack would involve scaling the seismic event proportional to the signal amplitude and inversely proportional to the noise power. However if the signal is constant, the signal can be weighted proportionally to the inverse square of the noise. In the case where noise is constant, the signal should be weighted by a scalar proportional to the signal amplitude.

APPENDIX C
ERROR ANALYSIS

C.1 Data (parallel) used for error analysis

Offset	Sin2theta	Amplitude
200	0	-1.84
300	0	-1.02
400	0	-1.62
500	0	-1.09
600	0	-1.47
700	0	-1
800	0	-1.5
1000	0	-1.91
1100	0	-0.59
1200	0	-0.78
1300	0	-0.8
1400	0	-0.8
1600	0	-1.49
1800	0	-1.49
1900	0	-1.79
2200	0	-1.21
3000	0	-0.819
3150	0	-1.24
3200	0	-1.59
3400	0	-1.378
3500	0	-1.373
3600	0	-0.6
3700	0	-1.3
4000	0	-0.21
4500	0	-0.71
4600	0	-0.84
5000	0	-0.8
5200	0	-1.08
5300	0	-1.19

C.2 Data (perpendicular) used for error analysis

Sin2theta	Amplitude
0.000171	-0.2
0.000384	-1.59
0.000682	-2.11
0.001065	-1.45
0.001533	-1.73
0.002086	-1.4
0.002722	-0.92
0.004245	-1.77
0.005131	-0.73
0.006099	-1.9
0.007149	-1.15
0.00828	-1.28
0.020145	-0.25
0.040258	-1.53
0.041481	-1.53
0.049134	-1.2
0.051801	-1.06
0.063015	-0.14
0.078152	-0.41
0.081315	-0.8
0.101115	-1.08
0.107995	-1.16